3-2020

Laser Shock Peening Pressure Impulse Determination via Empirical Data-Matching with Optimization Software

Colin C. Engebretsen

LASER SHOCK PEENING PRESSURE IMPULSE DETERMINATION VIA EMPIRICAL DATA-MATCHING WITH OPTIMIZATION SOFTWARE

DISSERTATION

Colin C. Engebretsen, Major, USAF

AFIT-ENY-DS-20-M-260

DEPARTMENT OF THE AIR FORCE
AIR UNIVERSITY

AIR FORCE INSTITUTE OF TECHNOLOGY

Wright-Patterson Air Force Base, Ohio

DISTRIBUTION STATEMENT A.
APPROVED FOR PUBLIC RELEASE; DISTRIBUTION UNLIMITED.

AFIT-ENY-DS-20-M-260

LASER SHOCK PEENING PRESSURE IMPULSE DETERMINATION VIA EMPIRICAL DATA-MATCHING WITH OPTIMIZATION SOFTWARE

DISSERTATION

Presented to the Faculty

Department of Aeronautics and Astronautics

Graduate School of Engineering and Management

Air Force Institute of Technology

Air University

Air Education and Training Command

In Partial Fulfillment of the Requirements for the

Degree of Doctor of Philosophy

Colin C. Engebretsen, BS, MS

Major, USAF

September 2019

AFIT-ENY-DS-20-M-260

LASER SHOCK PEENING PRESSURE IMPULSE DETERMINATION VIA EMPIRICAL DATA-MATCHING WITH OPTIMIZATION SOFTWARE

DISSERTATION

Colin C. Engebretsen, BS, MS
Major, USAF

Approved:

Dr. Anthony N. Palazotto (Chairman) — 25 Feb 2020 — Date

Dr. William P. Baker (Member) — 25 Feb 2020 — Date

Dr. Larry W. Burggraf (Member) — 25 Feb 2020 — Date

Dr. Kristina Langer (Member/Sponsor) — 25 Feb 2020 — Date

Accepted:

Dr. Adedeji B. Badiru
Dean, Gradual School of
Engineering and Management — 25 Feb 2020 — Date

Abstract

Laser shock peening (LSP) is a form of work hardening by means of laser induced pressure impulse. LSP imparts compressive residual stresses which can improve fatigue life of metallic alloys for structural use. The finite element modeling (FEM) of LSP is typically done by applying an assumed pressure impulse, as useful experimental measurement of this pressure impulse has not been adequately accomplished. This shortfall in the field is a current limitation to the accuracy of FE modeling, and was addressed in the current work.

A novel method was tested to determine the pressure impulse shape in time and space by optimization driven data-matching. FE model development and material model verification was completed in Abaqus. A 2D and 3D model type study was conducted. A proof of concept data-matching optimization tool was developed and verified. This data-matching optimization tool, using the Hooke-Jeeves optimization algorithm, was then applied to match experimentally collected residual stress measurements from single LSP treated spots in 2024-T351 aluminum specimens. Validation of this "best-fit" pressure impulse was attempted in a 6Al-4V titanium material model for the same LSP treatment process.

A combination Johnson-Cook viscoplasticity and Mie-Grüneisen equation of state (EOS) material model was shown to be amply sufficient for modeling the highly dynamic LSP event. A 2D axisymmetric FE model was shown to adequately represent a square LSP treatment process, in terms of residual stress field results with the use of a linear adjustment factor. The Hooke-Jeeves optimization algorithm proved highly successful at working through a FE model "black box" to match a target residual stress outcome. Further, this method was successful in matching the residual stress field of experimentally collected data. The validation of the best-fit pressure impulse in titanium was not a perfect match, but exhibited enough accuracy to be useful to design engineers in certain cases, and further shows potential for improvement and implementation toward this impulse matching goal.

Ineffable Creator,
You who are the true source of light, and wisdom. Pour forth upon my dense intellect a ray of your splendor that may take away the darkness of sin and ignorance. Endow me with a keenness of understanding, a retentive memory, measure and ease of learning, and discernment of what I read. Grant me rich grace with words, and the ability to express myself in thoroughness and charm. Guide the beginning of my work, direct its progress, and bring it to successful completion. This I ask through my Lord and Savior Jesus Christ, true God and true Man, who lives and reigns with you and the Holy Spirit.
Amen

- Saint Thomas Aquinas, A student's prayer

Acknowledgments

This work would not be possible without the funding of the Air Force Research Laboratories, and the support of my research committee. A special thanks to my sponsor, Dr. Langer for her guidance, and to my research advisor, Dr. Palazotto for his continued patience and willingness to weather my brainstorms and give tough direction. Other special thanks to the AFIT lab and model shop staff for their professionalism and willingness to help in any way possible, especially in a pinch.

To pursue a PhD is a prodigious exploit which fluctuates between labor of love and labor of loathing, is punctuated by moments of consternation and self-doubt, and culminates with as much self-discovery as self-improvement. The affair demands a great deal of backing and encouragement from friends and family; these are the real heroes of this endeavor. To the men of our biweekly bible study group (and home-improvement cohort), whose fellowship I highly value; to my parents and siblings, whose undue pride inspires me to be my best self; to my beautiful wife and children, my most cherished cheerleaders, and through whom the title doctor is made lowly to those of husband and father; but especially to my wife, who willingly sacrificed more than I would have asked of her to ensure my success. To these I bestow indelible gratitude.

Colin

Table of Contents

Page

List of Figures

Page

NOTE: All cited figures are used on the basis of “Fair Use” under section 107 of the Copyright Act of 1976, 17 U.S.C. § 107 (1994).

List of Tables

Page

List of Nomenclature & Acronyms

A, B, C, m, n	=	Johnson-Cook Constants (Material Properties see page 54)
c_0	=	Bulk Sound Speed (Material Property)
E	=	Modulus of elasticity (Material Property)
E_m	=	Energy per Unit Mass
EOS	=	Equation of state (see page 20 and 59)
FEM	=	Finite element model
FWHM	=	Full width half maximum (impulse peak measurement)
HEL	=	Hugoniot elastic limit (see page 20)
I	=	Laser intensity
LSP	=	Laser shock peening
P	=	Pressure
s	=	Hugoniot Slope Coefficient (Material Property)
SRT	=	Short rise time [pressure impulse shape] (see page 23)
T	=	Temperature
T_m	=	Melting Temperature
T_0	=	Reference Temperature
U_p	=	Particle Velocity
U_s	=	Shock Velocity
VISAR	=	Velocimetry interferometer system for any reflector (see page 20)
XRD	=	X-Ray diffraction (see page 10)
Γ_0	=	Mie-Grüneisen Constant (Material Property)
η	=	Nominal Volumetric Compressive Strain
ε	=	Strain
$\dot{\varepsilon}$	=	Strain Rate
$\dot{\varepsilon_0}$	=	Reference Strain Rate
ν	=	Poisson's Ratio (Material Property)
ρ	=	Density
ρ_0	=	Reference Density
σ_y	=	Flow Stress

LASER SHOCK PEENING PRESSURE IMPULSE DETERMINATION VIA EMPIRICAL DATA-MATCHING WITH OPTIMIZATION SOFTWARE

I. Introduction & Background

Objective

Laser shock peening or processing (LSP) is a method of work hardening of metallic alloys for surface hardness or fatigue life improvement. Finite element modeling (FEM) of the process, however, often relies on an assumed pressure impulse, as the event is not easily measured in-situ. The objective of the current work was to build a stronger connection between FEM and the empirical residual stresses imparted by LSP. The unique approach taken here, utilized Isight optimization code (described in Appendix B. Isight Optimization Code Details) in conjunction with Abaqus FE code (Appendix A. Abaqus Finite Element Code Details) to deduce the LSP pressure impulse shape in time and space by matching empirical data from a single LSP spot, namely surface deformation (or dimple volumetry) and residual stress. This deduced pressure impulse was then applied to a second material and the FEM-predicted dimple volumetry and residual stress were compared to experimental results for validation. This method is a first step in the ability to "catalog" pressure impulse shapes which correspond to certain settings in a laser system, and which could be applied in the FE model for better prediction of the resultant residual stress field for a specific application.

Overview

Laser shock peening or processing (LSP) is mechanical in nature, not thermal, imparting compressive residual stresses into a workpiece via pressure impulses initiated by laser burst. In metallic alloys, LSP and its associated compressive residual stresses have been shown to improve surface hardness and yield strength, as well as the resistance to fatigue and stress corrosion cracking [1]. There have been many recent practical applications of LSP on military and civil aircraft for fatigue life extension. Examples of titanium treatment are seen in turbine engine blades in the B-1B, F-16, and Boeing 777 and 787; examples of steel treatment are seen in military helicopter rotor gears and in large landing gear structural members of military fixed wing aircraft; and examples of aluminum treatment are seen in T-38 side-brace trunnions [2]. A more significant example can be found in the titanium wing lug of the F-22, for which the LSP treatment qualification involved full-scale fatigue testing, and took over four years, costing the program a great deal of money (an example which is currently being repeated on the forward bulkhead of the F-35 Joint-Strike-Fighter) [2].

Motivation

The F-22 wing lug example demonstrates perhaps the biggest shortfall in LSP today, that is, the lack of validated predictive modeling with enough confidence to preclude expensive full-scale testing for process qualification. One root cause of this gap lies in the relatively unknown pressure impulse shape in both time and space. This impulse occurs over just a few hundred nanoseconds and peaks at pressures in the gigapascal (GPa) range, making it difficult to measure directly in-situ [3]. Further, LSP

settings and best practices tend to be based on proprietary experience, customized for individual applications, and governed only loosely by Aerospace Material Specification (AMS) 2546 in which "cognizant engineering" is a common fallback [4]. As a result, most FEM is done by applying an assumed pressure impulse shape in time and space, resulting in inconsistencies among modeling methods and predicted residual stresses.

Background

Not long after the advent of the laser (1960), researchers began to test the effects of high powered laser pulses on different materials, noticing immediately that momentum could be transferred to objects in this way [5], [6]. The momentum was discovered to produce a stress wave in solid materials, and very early, the stress wave was measured with the use of a quartz gauge [7]. With the stress wave as the focus of attention, more work was done in an attempt to augment the impulse imparted by the laser, first by use of volatile transparent overlays such as RTV adhesives [8], then through application of ablative paint and foil coatings and transparent inertial boundary, typically water [9], [10]. Some of the first hydro-code based computer modeling began around this time (mid 1970's) in an attempt to predict modifications which could improve the peak pressures transferred to the substrate material [11]. LSP was soon put to use for hardening of metallic materials [12], [13], notably in aluminum for improved durability of weld zones [14]. The study of these hardening effects continued into significant improvement of fatigue resistance in many alloys.

The basic process of LSP is fairly consistent across most proprietors today. The substrate is first coated with an ablative layer; this is usually a dark paint, tape, or foil,

though the substrate itself can serve as the ablative material in some cases. Next, the workpiece is secured in a traversing fixture and an inertial boundary is applied; this can consist of quartz, glass, or more commonly laminar flowing water. The laser is then pulsed at the target, vaporizing the ablative tape into a rapidly expanding plasma bubble at a single spot. The bubble is contained by the inertial boundary and thus directs a shock into the substrate material. (See Figure 1 for details) The process is repeated in an array of spots large enough to cover the desired treatment area. Typically the entire process it repeated again in another slightly offset array, creating an overlap which provides a more uniform residual stress field in the workpiece. [1]

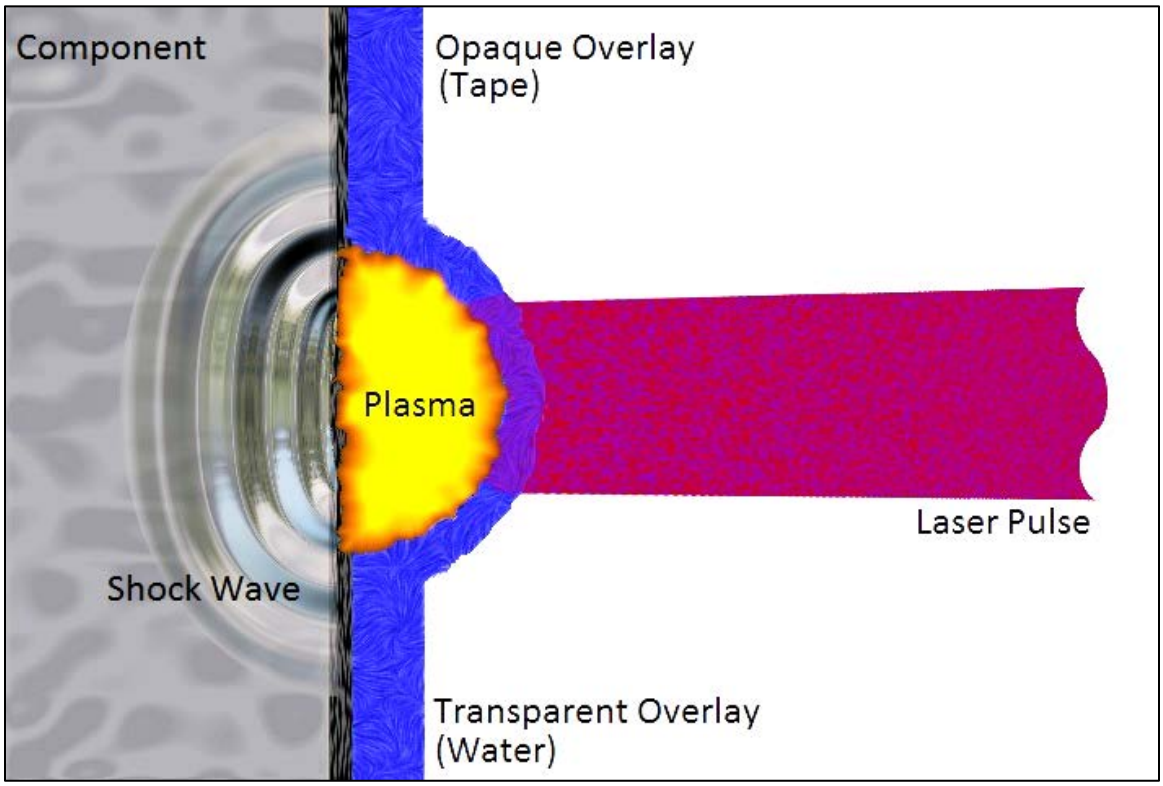

Figure 1: Diagram of LSP process single burst [15]

Laser Systems

Lasers for LSP treatment are typically Neodymium-doped, Q-switched lasers up to 100 joules (J) in power [16], with pulse duration ranging from fractions to hundreds of nanoseconds (ns), and spot sizes ranging from fractions to tens of millimeters (mm). The result of these variety of settings is a broad range of laser power densities at the workpiece, from fractions to thousands of gigawatts per square centimeter (GW/cm^2) [16]. The power density is the widely accepted metric on which to judge any given treatment process, and for given ablative and inertial layer conditions, will most directly correlate to peak impulse pressure. [1]

Literature Review

The following section will take a look at key research, with an emphasis on recent work, which fills in important background and highlights the state of the field of late. It is not meant to be an all-inclusive, but rather focused on the most pertinent and applicable research which builds the foundation and motivation for this work. The review will cover three topic areas to support the objective of the current work; first, the material improvements that are imparted by LSP and which make it so valuable; next, the evolution of the modeling of LSP, and the best practices or shortfalls seen today; finally, the measurement of LSP process parameters such as pressures or velocities, and LSP results such as surface displacement and residual stress, which are needed for validation of FE modeling of the process.

Material Improvement from LSP

LSP has been well researched and utilized to improve surface hardness, fatigue life, and other properties of metallic alloys. The following is a brief, approximately chronological summary of some of the fundamental work demonstrating the improvement of mechanical properties in LSP treated alloys, with an emphasis on more recent work.

Battelle Laboratory was early to examine fatigue life in 2024-T3 aluminum with notched holes. [17] They compared untreated specimens to those treated with LSP in both a solid circular application area, as well as an annular treatment area to attempt to arrest propagating cracks while still allowing them to be observable under inspection. Both LSP treatments resulted in a measured fatigue improvement, with the greatest seen in the solid treatment zone in which cracks took a large number of cycles to initiate from the notches. The cycles to failure in these treated specimens exceeded 20 times those left untreated. [17]

Peyre and Fabbro explored fatigue of notched specimens of 7075, Al-12%Si, and A356-T6 aluminum alloys in untreated, shot-peened, and LSP treated conditions. [18] The work utilized a 50% overlapping pattern of 3 square laser bursts. They found that LSP imparted compressive residual stresses more than four times deeper below the surface than traditional shot peening. Further, LSP was found to be very effective in raising the fatigue strength in the S-N fatigue curves nearly 20% in all materials when compared to untreated specimens, and also showed an advantage of nearly 10% over shot-peened samples in 7075. At stresses of 260 MPa, the fatigue life in 7075 aluminum

was improved more than six fold compared to untreated specimens, and still three fold compared to traditional shot peening. [18]

Having been quite successful in LSP endeavors, some experts from Battelle Labs created their own company, LSP Technologies Inc. Allan Clauer among these, continued research in the area of improving fatigue resistance via LSP treatment. [19] The work was very thorough in measuring LSP imparted residual stresses in various steel, aluminum, and titanium alloys. LSP was effective in improving tensile, bending, and fretting fatigue life in these materials when compared to untreated specimens, including cases in which cracks were pre-grown for many cycles before LSP treatment. In a number of cases, treated specimens endured 50-100 times as many cycles as untreated specimens. [19]

Later work by LSP Technologies investigated LSP treatment around fastener holes, and stopholes in 2024 aluminum. [20] Residual stresses were measured using X-ray diffraction (XRD). XRD is a method of residual stress measurement in which the angle of diffraction of collinear X-Rays through a material indicate the matrix spacing, and thus elastic strain trapped in the material. In all cases, LSP showed delay of crack initiation, most prominent in the center-hole specimens. Also, fatigue life in every type of specimen was improved by an order of magnitude. [20]

The General Electric Company (GE) has been, perhaps, the biggest user of LSP in the aviation industry since the 1990s [21], [22], as LSP has been shown to greatly improve fatigue life of turbine engine fan blades including in cases of foreign object damage. GE has numerous patents relating to use of LSP on turbine engines, including

turbine blade airfoil leading edge treatment, and the use of volumetric dimple analysis as a means of quality assurance. [21], [22]

The US Air Force has also led many research efforts into LSP application. [23] One partnership with University of Dayton Research Institute (UDRI) was very thorough in investigating fatigue nucleation and crack growth in untreated, shot peened, and LSP treated titanium specimens. The research utilized a three point bend test, and unique tapered specimens to closely replicate turbine fan blade leading edge geometry. The research tested un-notched, notched, and simulated foreign-object damaged (FOD) specimens. The results showed negligible improvement of LSP treated samples when un-notched. Both notched, and FOD sample fatigue lives were improved when treated with LSP, only slightly for a higher, 0.8 stress ratio, substantially more so for the lower, 0.1 stress ratio. While the unusual step-loading design of the experiment was such that it did not offer a large statistical sample to establish an entire S-N curve, it still demonstrated the improvement of LSP over untreated, and shot-peened titanium under damage-like conditions. [23]

An interesting work by Nikitin et al. [24] tested the fatigue behavior of LSP treated and deep rolled 304 stainless steel at high temperatures (up to 600˚ C). The thorough study used high-energy synchrotron XRD to measure residual stresses at various fatigue points to determine stress relaxation of both types of treatment. LSP improved fatigue life nearly as much as deep rolling and was equally effective at all temperatures even though the residual stresses from LSP did not extend as deep into the material as deep rolling. Fatigue cycle stress relaxation is prominent in all cases, but

becomes more pronounced at higher temperatures. Ultimately LSP proved itself to be almost equally as effective as deep rolling for the purposes of fatigue life extension at a broad range of temperatures in stainless steel. [24]

LSP treatment of cold pilger dies for rolling tubing was the focus of a Pacific Northwest National Lab study [25]. These A2 tool steel dies tend to fail due to fatigue cracks which then imprint onto the rolled tubing. Here again, XRD was used to measure residual stress at the treated surface. LSP was extremely effective at imparting compressive residual stresses over 1 mm deep into the material. LSP also showed a dramatic improvement of the life of the die (measured in length of tubing processed), a 300% increase. One unique note of the work was the physical change in failure appearance when LSP was used. Instead of failing in the form of cracks, the LSP treated dies failed in a kind of flaking failure mode, possibly due to the dimpled texture that LSP imparted onto the die during treatment. [25]

A study out of China looked at the fatigue life of 7050 aluminum specimens treated with two different LSP shocked paths. While the premise left one hopeful for a study of feasible LSP treatment arrays, it was in fact simply a comparison of two LSP rows and four LSP rows on either side of the fatigue specimen hole. Not only does this not afford the opportunity to compare to an un-treated specimen, but the treatment method is not representative of best practices for fatigue improvement. The study still showed a slight improvement with the addition of more LSP treatment, of questionable significance, however. [26]

Research by Achintha et al. [27] was conducted on 7010 and 2024 aluminum alloy tensile specimens with a center hole. The work compared fatigue life of untreated specimens, full width LSP treatment, full width traditional shot peening, and a smaller LSP treatment patch concentrated around the hole. The study also tested two different thicknesses at multiple stress levels, all at a 0.1 stress ratio. For 15 mm thick specimens, LSP was not effective at improving fatigue life, however traditional peening was. Only the concentrated patch LSP treatment in 5 mm specimens resulted in significant fatigue life improvement (over 10x) over both untreated, and shot peened specimens. [27]

A study out of India, in conjunction with Tata Motors [28], examined fatigue life extension of spring steel which had already endured 50% of their expected fatigue life. The specimens were machined to remove the decarburized layer from heat treatment, and were fatigued in three-point bend test for approximately 50% of their expected life. Some of the specimens were then treated on the tensile side with LSP, residual stresses were determined by XRD, and fatigue tests were continued to failure. The work also compared paint and PVC-based tape for ablative coatings, finding that the tape was superior. The study was very thorough with its characterization of the steels, both treated and untreated. It was found that LSP improved surface hardness and yield strength and reduced the energy spent in plastic deformation. Ultimately, the LSP treated specimens saw fatigue life improved 15 times over that of untreated specimens. [28]

A Jiangsu University study [29] looked at the effects of LSP on stress corrosion properties of laser welded joints in 7075 aluminum. A good comparison was made between treated and untreated weld zones. LSP promoted grain refinement when

compared to untreated weld zones. LSP treated specimens also had improved microhardness, as well as higher compressive residual stresses in the weld zone as would be expected. Slow strain rate tensile tests were conducted on treated and untreated specimens, each in air as well as 3.5% saline solution. LSP provided noticeably improved stress corrosion properties of the welded specimens in the saline solution, resulting in 19% stronger ultimate strength, and 32% more plastic deformation than untreated specimens. The same results were slightly less noticeable in tests conducted in air, but LSP treated specimens were still 12% stronger, and allowed 28% more plastic deformation before failure. Most interestingly in the study, extensive microscopic evaluation of the grain structure and fracture face showed significant changes in the mode of failure when specimens were treated with LSP. Intergranular fracture of the base material dominated LSP treated specimens, while untreated specimens failed in transgranular fractures in the weld zones. [29]

A unique study from the University of Nebraska-Lincoln [30] looked at LSP in polycrystalline alumina ceramics (α-AL_2O_3), which are typically susceptible to indentation cracking. LSP proved effective at imparting compressive residual stresses as deep as 1.2 mm into the ceramics, although this was also accompanied by increased surface roughness. Further, the process generally left grains on the surface intact, but occasionally resulted in small damage regions near grain boundaries, correlating with higher laser power. LSP also resulted in higher surface hardness, reduced cracking around the Vickers indentations, and finally, the imparted compressive residual stresses can improve resistance to indentation cracking. [30]

Recent work out of Serbia [31] looked at LSP in the nickel based Nimonic 263 superalloy, focusing exclusively on picosecond laser pulse duration. This specific alloy is usually exposed to elevated temperatures and tends to degrade due to creep. Both low infrared, as well as green wavelength lasers were tested at varying power densities, with varying number of accumulated pulses in the study. The study was a bit misguided in its application of LSP, pulsing numerous times, apparently in the same location, without replacing the ablative coating. This resulted in partial melting of the material at the surface, and unusual results for the higher number of laser pulses, thus, these results will be thrown out of the discussion of the paper. The work took a close look at the grain structure of the material, examined elemental composition via spectroscopy, and also measured surface hardness and roughness. The spectroscopy showed large variations of the elemental readings, bringing into question the execution of the measurement for this case. Surface roughness was increased by the LSP treatment, but surface hardness was improved. This part of the work seemed reliable, and remained consistent with other findings. [31]

A paper out of Iran [32] explored the effects of LSP in 6061 aluminum, analyzing surface hardness, roughness, grain structure and residual stresses and their dependence on laser beam overlap, scanning pattern, and number of shots. The study is another example of one which applied multiple LSP pulses, without reapplication of the ablative layer. In this case, however, the maximum number of consecutive pulses on any single location was kept very small and as such, the LSP treatment is more-or-less consistent with industry best practices, although only the first impulse likely reaped the full benefits of

the ablative coating, as the subsequent shots were thus imparted onto nearly bare metal. Comparisons were made between single and double impulses at each coordinate, scanned in both switchback and inward spiral paths utilizing between 0 and 70% overlap of sequential spots. Residual stresses were measured with XRD, and hardness with the Vickers test. Consistent with past results, the LSP treatment imparted compressive residual stresses, and improved surface hardness in every sample. Surface roughness also increased for every treated sample. Comparing between treatment methods, generally the more impulses per area, the higher the surface hardness; 50% overlap of double impulse peening provided the highest average hardness into the depth. The spiral pattern showed a very slight advantage in hardness over the switchback pattern. Overall, LSP imparted rather large compressive residual stresses although anisotropic results were observed, potentially due to the original rolling of the material. [32]

A recent study out of Mexico [33] compared LSP treatment of stainless steel notched fatigue specimens of varying thicknesses. The work was excellent in melding modeling to empirical tests, using Abaqus for FEM and FE-Safe for fatigue modeling. Specimens of 2205 stainless steel were made in thicknesses of 2, 3, and 4 mm. Some of the specimens were then LSP treated around the notched area, and all of the specimens were fatigued in a standard R=0.1 fatigue loading test. FEM was sped up using the eigenstrain model, which will be discussed in a later section more in depth. In the modeling sense, the work serves to demonstrate the motivation herein, there is a weakness between modeling and experiment which needs to be overcome. Residual stresses predicted by FEM did not do well to match those measured experimentally via

hole-drilling. As a result, the predicted fatigue life varied somewhat from experimental results. In terms of experimental fatigue life improvement, the work reinforces the utility of LSP, with all specimens showing improved fatigue life. Further, the biggest gains were seen in the thinnest material: the 2 mm thick specimens showed 300% improvement in fatigue life, the 3 mm specimens had 143% improvement, and the 4 mm specimens had just 79% improvement. These were all still significant improvements over untreated materials. [33]

Work completed by David Eisensmith here at AFIT [34] tested LSP as treatment over minimally detectable partial through-thickness cracks in 7075 aluminum. Driven by the aging fleet of Air Force aircraft, the work explored the capability of LSP to improve fatigue life in specimens with cracks already formed to a size discoverable by standard non-destructive inspection (NDI) techniques. The work also utilized neutron diffraction for measuring residual stresses in LSP treated specimens. He showed that LSP could be applied over top of surface cracks without negative effects in the processing, and a comparison of square vs. round laser spot LSP treatment showed minimal differences in residual stress field. Further, the application of LSP over surface cracks resulted in a significant increase in fatigue life, in fact halting crack growth in every specimen treated by LSP. [34], [35]

Work by Lainé et al. [36] looked more closely at the microstructure and residual stresses of titanium after both shot peening and LSP. The study used cross-rolled titanium which was then milled and processed by either LSP, or traditional shot peening, or both. Grain structure was studied via electron back scatter diffraction, transmission

electron, and transmission Kikuchi diffraction microscopy. Residual stresses were measured using the hole-drilling method. One focus of the work was the observation of deformation twinning due to high strain rates in the processes. LSP on top of traditional shot peening resulted in compressive residual stresses approximately seven times deeper below the surface than shot peening by itself. Both methods of work hardening result in dislocations in the grains. In shot peening, the dislocations are very tangled in shape, in LSP the dislocations take on a very planar geometry and appear to create sub-grain cells. Interestingly, the LSP process, despite very high strain rates, resulted in very minimal deformation twinning near the surface, and none below the immediate surface. This is in contrast to traditional shot peening which introduced deformation twinning well below the surface, despite significantly lower strain rates. The work provided some very interesting metallographic insight into the processes, but also reinforced the deep residual stresses imparted by LSP which make the process so effective. [36]

A study out of Beijing recently addressed the influence of LSP on wire-arc additive manufactured 2319 aluminum specimens [37]. This manufacturing process is fast and cheap, but produces inconsistent material properties due to inconsistent grain structure and imperfections in the material. Manufactured plates were milled to uniform thickness and specimens were cut normal to printed layers. LSP was applied through the middle section of the specimens. Grain size and orientation were examined via electron back-scatter. Residual stresses were measured by hole-drilling, hardness via micro-Vickers tests, and yield and ultimate strength as well as elongation were measure via standard tensile test. Electron back-scatter showed that LSP treatment resulted in

reduced average grain size, a reduced number of very large grains, and more uniform grain orientation. As expected, LSP also resulted in significantly improved hardness as deep as 1 mm below the surface. Residual stress in the untreated specimens tended to be tensile near the surface. LSP overcame this defect and imparted compressive residual stresses more than 0.75 mm into the depth. The overall effects on tensile properties were also positive: LSP treated specimens, with minimal reduction of ultimate strength (<3%), had 72% improved yield strength, and less than half the total elongation at failure. These changes represent a very welcome improvement to a very cost-effective additive manufacturing process. [37]

Computer Modeling of LSP

Having thoroughly demonstrated the material improvements which bring so much merit to the use of LSP in the practical sense, it is necessary to explore the historical and technical development of engineering computer modeling of this process. Early predictive modeling via hydro-codes for the purposes of shock wave augmentation was mentioned earlier [11]. The following will address, in approximately chronological order, predictive modeling of the mechanics of LSP in metallic alloys and the resultant material benefits in terms of residual stresses and deformation. Specific attention will be paid to model flow and material properties (as an example of best practices), as well as pressure impulse shape assumptions (as an example of the *lack* of consistent best practices).

Substantial modeling of the mechanics of LSP did not occur until the 1990s. Berthe et al. [38] paired a confined ablation analytical model with a one-dimensional

hydro-code to follow a shock-wave through aluminum foils under a water boundary. The code assumed an elastic, perfectly plastic behavior, but utilized Mie-Grüneisen equation of state (EOS) which accounts for hydrostatic pressures exceeding the Hugoniot elastic limit (HEL), that is the applied pressure above which the solid no longer compresses elastically, but in an elastic-plastic way, behaving more like a fluid with reduced shear strength. The work was effective at modeling the traversing of the shock-wave through the material because of the specifically tailored material properties. This made it effective for tracing the shock decay through the material and correlated well with velocimetry interferometer system for any reflector (VISAR) measurements of the same. The shockwave profile points to the short-rise-time pressure profile that has come to be expected of an LSP event (discussed later). However, their work over-predicts the duration of the pressure at much higher power density. Further, the oversimplification of the material to uniaxial, perfectly plastic properties means that this type of simulation is not effective at predicting deformation or residual stress during or after the event. [38]

Braisted and Brockman [39] did a very thorough FEM analysis of laser shock peening, and were seemingly the first to compare predicted residual stresses to LSP empirical results and XRD measured residual stresses. The work used Abaqus in a two-step process to streamline the computational burden of such a highly dynamic event. The challenge in modeling LSP is with the highly plastic behavior, in conjunction with high kinetic energy imparted into the workpiece which requires a very long time to dissipate. By passing static data to the explicit time integration portion of Abaqus for plastic deformation, and dynamic data back to the implicit time integration for final equilibrium

analysis, determination of both the immediate shock response as well as the final residual stress state was greatly streamlined. This was particularly effective when multiple laser shots were being imparted onto the substrate material as the resultant stress states could be continually passed between the two integration methods. The material model used a dynamic yield criteria based on split-Hopkinson bar tests, with upper limits determined via flyer-plate tests and HEL. The work still assumed an elastic-perfectly plastic property, but used a linear EOS and an axisymmetric model allowing a radially variable residual stress field. The pressure impulse in the work was assumed to be uniform across the round spot and followed a triangular impulse over time with a peak pressure of 5 GPa, all based on rudimentary experimental observations from prior work. The finite element mesh constituted a rather refined mesh extending one and a half laser spot radii from the center of the spot, and into the depth. Outside of this zone, infinite elements were used to prevent any shock reflection within the material affecting residual stresses. [39] The use of infinite element does not precisely represent actual material response, particularly in geometries which are of finite thickness, as stress waves would be reflected off of boundary surfaces and their interference within the material would result in different residual stresses [40]. Infinite elements are useful, however, because they reduce computation time by allowing the omission of dissipation time of these reflected stress waves. They can also be suitably representative of LSP in a sufficiently large structure where reflected waves would interfere with primary waves well outside of the LSP area of interest. The suitability of this method of modeling will be discussed more in-depth when outlining the methodology of this work. The work of Braisted &

Brockman was a very substantial first step into FE modeling, and was very effective at predicting residual stress fields, particularly near the surface, but accuracy diminished notably further into the depth of the substrate. Their work also exposed a radial focusing effect, especially prominent in round laser spots, which results in reduced compressive, or even tensile residual stress at the center of the circular spot. [39]

Ding and Ye have been big contributors to the LSP field. In one of their earliest collaborative works they paired past experimental data and analytical modeling with a new finite element effort [41]. They too used Abaqus with an explicit and implicit integration exchange technique. Their work utilized a square spot by using quarter symmetry and also implemented fully surrounding infinite elements leaving only the treated surface free. The pressure impulse was assumed to be uniform over the spot area, and following a triangular distribution over a time of 100 ns. The region of very refined mesh in the work extended to twice the width of the square spot. The von Mises yield criterion was used based on HEL dynamic yield strength. The simulation showed that it takes quite some time for the imparted energy to dissipate fully; though the pressure impulse had a duration of only 100 ns, the simulation required 4000 ns for the dynamic stresses to diminish sufficiently to be considered an adequate solution. The simulation also did a reasonable job at matching experimental residual stresses, particularly near the treated surface. The study also completed a parametric study, varying the number of impulses on a single spot, peak pressures, impulse duration, and spot size. Fundamentally, the work showed that compressive residual stresses were higher and deeper into the substrate with increasing number of shocks. Higher pressures resulted in

deeper plastic deformation, but not necessarily higher residual stresses. Longer impulse time resulted in deeper plastic deformation but below a minimum pulse duration, negligible residual stresses were found. The spot size had little effect on plastic deformation, but the work confirmed that of Braisted & Brockman in that a square spot is superior in uniformity of residual stress field. [41]

A 2008 work by Warren et al. [42] was among the first to look at not just laser intensity and spot size, but also array spacing on the resultant residual stresses. The work again used Abaqus in a three-dimensional model surrounded by infinite elements. After benchmarking the simulation against past observed data, the research conducted a design of experiment (DOE) sensitivity study, changing laser intensity, spot size, and array spacing to determine the effects on residual stress field. The work utilized a Gaussian pressure distribution over the round laser spot, and was among the first to utilize a short-rise-time (SRT) impulse shape in the time domain, that is a pressure impulse which spikes quickly, but takes much longer to dissipate. This impulse shape reaches a peak pressure just before the completion of the laser burst, but takes approximately three times longer to fully dissipate (see Figure 2).

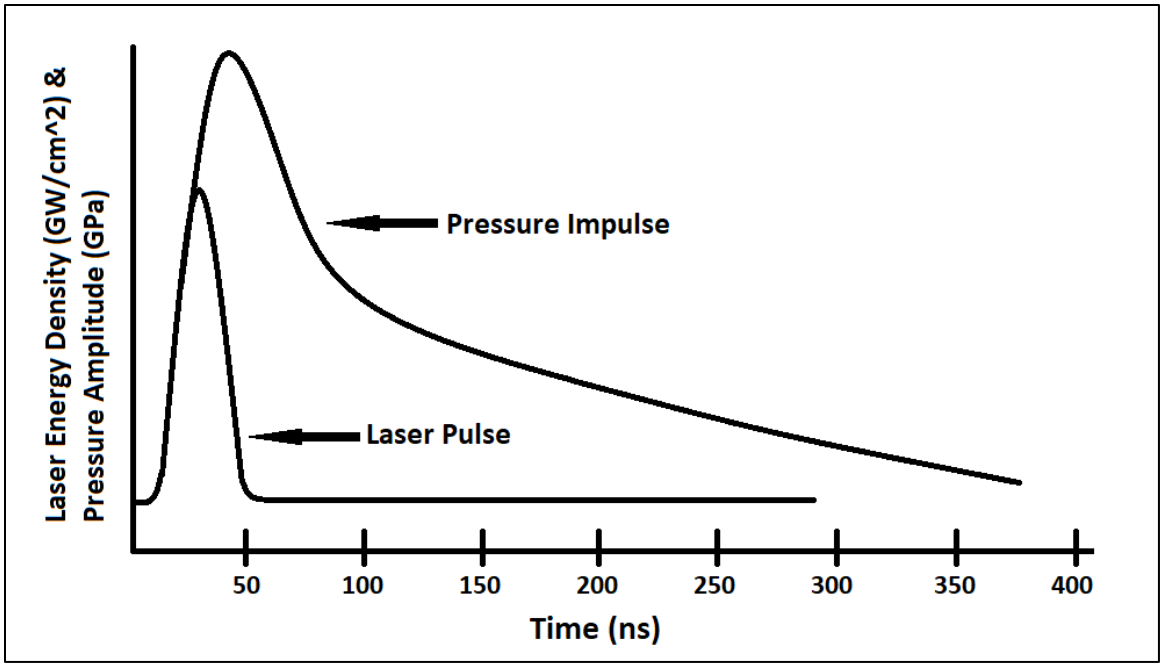

Figure 2: Example of short rise time (SRT) pressure impulse from Gaussian laser pulse [43]

The work demonstrates one of the substantial obstacles to overcome in relating FEM and experimental LSP results. As seen in the benchmark of the work, the point-wise residual stresses from a simulation will be difficult to match to experimental data for which residual stress measurement methods such as XRD in this case can only measure an average residual stress over a small gauge volume. Nonetheless, with at least a qualitative verification of the FEM, the DOE of the work provided some valuable insights. First, as seen prior, increased laser intensity results in larger, deeper residual stresses, and larger laser spots result in more plastic deformation. Concerning array spacing; larger, more uniform residual stress fields can be achieved by overlapping laser spots. [42]

A two-part special issue paper by DeWald and Hill presented a very novel approach to LSP residual stress modeling [44], [45]. The method utilizes a relatively

recent numerical technique called the “eigenstrain method.” This method takes residual stress results of one advanced simulation from which the LSP eigenstrain is defined; an elastic material model is then built and the application of the eigenstrain as “misfit strain” to this model results in residual stresses representative of an LSP shot. The second of the two papers looked at the validation of the predictions on many different radii of fillets and round bars and pipes. The eigenstrain method holds a lot of promise in LSP modeling due to the simplicity of the model and thus the huge computation savings. However, the results showed errors as high as ~35%, and appear to be highly geometry (and boundary condition) dependent. As such, the method has limitations which are not suitable for improving generalized predictive modeling of LSP as the “catalog” of eigenstrain fields would necessarily be tailored to both laser settings *and* substrate geometry. [44], [45]

A PhD dissertation by Singh [46], sought to optimize the residual stress field by controlling LSP parameters. The work is yet another which uses Abaqus explicit integration for the plastic portion of the process with data hand-off to implicit integration to determine the final equilibrium. The optimization effort used increasingly refined simulations to narrow the optimization space, beginning first with a 2D axisymmetric model, then working up to a full 3D model run on a supercomputing cluster. The pressure impulse more or less followed the SRT temporal distribution, but was divided into concentric rings to vary the spatial distribution, interestingly with peak pressure at the outermost ring tapering to 80% peak pressure in the center of the spot. [47] This distribution was based on a prior dissertation out of Ohio State University [48], and no

other references or justification for the unusual pressure shape were given. Material properties for the preliminary model utilized HEL dependent dynamic yield strength with elastic, perfectly plastic behavior. The more detailed model in the optimization process used the Johnson-Cook yield criteria which is an empirically based material model. To more accurately compare FEM results to experimental residual stress fields measured by XRD, the author utilized an averaging scheme over a small portion of the mesh. The model slightly over-predicted residual stress profile near the treated surface, but converged somewhat deeper below the surface. The dissertation went on to look at double spot overlap and seven spot overlap patterns for interaction. Further, the work sought to achieve certain residual stress fields via optimization of LSP parameters. The FEM part of the work reinforced previous findings; higher pressure, larger spots, and overlapping patterns increase the magnitude, depth, and uniformity of compressive residual stresses in LSP treated materials. The optimization portion of the research found that a given residual stress profile could be achieved via multiple LSP spot intensity/size combinations. Most interestingly, the work showed that an elliptical spot would alleviate the tendency to produce a more tensile region in the center of the spot. [47] The work carried forward to fatigue life optimization of LSP treated bending specimens by simply transferring residual stress results to FE-Safe fatigue life simulation software. The results predicted a huge increase in fatigue life, particularly for lower pressure LSP treatment, though the model was not validated via experimental results. [46]

Work by Ivetic in 2011 [49] sought to improve the modeling of LSP in thinner sheets and instances when an infinite element backing may not be an accurate

representation of reality. The material model for the work implemented a Johnson-Cook plasticity with the addition of the Mie-Grüneisen EOS. Abaqus explicit integration was used for the entirety of the simulation since chosen material parameters are only available in the explicit code. The work examined varying maximum pressure, impulse durations, and square spot size; it even looked at the possibility of applying a damping panel to the top surface for use in an in-field treatment without access to the back of the work piece. The model showed the best residual stresses were achieved at low pressures, short duration, and also with a damping layer on the top. The effectiveness of the damping layer was very sensitive to laser settings, however and is not likely to present a useful solution. The biggest shortfall of the work was the lack of any experimental validation, especially considering a model verification was compared to work where specimens were peened on both sides, or via multiple shots made to match past work via manually input cyclic hardening. While one could reasonably expect the trends to be indicative of real-world performance, the fact that boundary conditions were not accurately represented leaves a bit of doubt. [49]

Brockman et al. [50] conducted perhaps the most thorough study to date of LSP in aluminum and titanium by using Abaqus. The paper looked at residual stress variations at small scale which ought to be interpreted with some care. The model incorporated a very refined FE model with symmetry on the opposing surface to replicate a double-sided LSP treatment. The material models for both metals used Johnson-Cook flow model with von Mises yield criterion and an additional isotropic hardening model. The pressure impulse was given a spatial distribution based on the measured laser power distribution

over the size of the spot, though the profile is not explicitly described in the paper. Temporally, the impulse utilizes the SRT profile with a peak pressure between 3 and 11 ns, and trailing off to zero at 300 ns. The work was careful to note that for such short pressure duration, particularly with a well define peak, it is important to use a small enough time step in the simulation so as to "capture" the full peak pressure or it will not have the full influence on the model. The model further refined the explicit to implicit hand-off method by cycling between the standard explicit integration impulse step, and a highly damped explicit integration relaxation step; doing this multiple times to represent sequential LSP shots in an array. After the plastic strain-rate diminished to zero, the dynamic state was then handed-off to the implicit integration step to determine the final static residual stresses. One overarching discovery in the work was the presence of many localized variations in the residual stress field dependent on spot overlap, stress wave reflection, or pressure variations. The work importantly noted that residual stress measured by XRD is actually an average of the residual stress over the chosen or designed gauge volume. To compensate for this fact, the paper utilized a continuous interpolation area average to make a better comparison to XRD measured residual stresses. The predicted residual stresses in the work also showed interactions from reflected waves which were then studied for further understanding. The paper demonstrated a very well-planned computer modeling technique to best utilize available technology. It also looked in depth at effects of LSP technique and specimen geometry on resultant stresses and showed the need for better understanding of associated uncertainties. Perhaps most usefully, it showed a viable averaging of FEM residual

stresses to compare to common empirical measurement techniques (which themselves are averages), and demonstrated the need to better understand highly localized stress variations as they likely contribute greatly to fatigue life and do not show up in the averages of common residual stress measurement techniques. [50]

A recent work out of France linked FEM to empirical results of LSP in 2050 aluminum [51]. The work modeled the entire laser shock of a single spot in a single explicit simulation in Abaqus instead of determining the final equilibrium via an implicit simulation. The FE model was entirely 3D rectangular with a round spot, and infinite elements on all sides except the treated surface. The pressure impulse was modeled with the SRT profile over a time of 210 ns, and a spatial profile that produced a spherical distribution with a half-power pressure at the outer edges of the circular spot. The simulation considered the kinetic energy of the model to determine when the simulation had reached a steady state of residual stresses, ultimately running nearly two orders of magnitude longer than the pressure impulse itself. The material model for the paper utilized the Johnson-Cook flow rule with Mie-Grüneisen EOS. The work traced the shock wave propagation through the depth at various time steps immediately after impact to show the dynamic yield strength and the shock dissipation over time. The paper compared FEM and empirical results of surface displacement and residual stress field for a single laser spot as well as a multiple spot array. Residual stress was measured by XRD, and the work fell prey to comparing point-wise FEM stresses to XRD average stress but made an effort to improve the comparison. The surface displacement, however showed fairly accurate agreement with experiment for the LSP array, and very excellent

agreement for the single spot. The work showed some anisotropy in the residual stress field, as well as reduced compressive stresses toward the center of the spot particularly for higher pressures. [51]

Li et al. [52] conducted a study of LSP on titanium turbine blades, using an explicit simulation in ANSYS to model the process and compare to experimental results. The model utilized Johnson-Cook material properties, and the pressure impulse was stated to have been modeled based on prior theoretical work but was not explicitly described. The paper simulated four different peak pressures and compared residual stress results; it identified the previously demonstrated reduced compressive stress in the center of the spot at higher pressures. The experimental LSP application was conducted using aluminum foil for the ablative layer, was confined with water, and the peak pressure was measured via thin film sensor though the results were not mentioned. The diameter of the shock indentation, as well as the residual stresses were compared to the model and agreed quite well. It was not stated exactly how residual stress was measure, bringing some question as to the legitimacy of the comparison. The value in the paper stems mostly from the modeling effort which reinforced trends discovered in prior work. The experimental side of the work seemed a bit lacking and not fully discussed, so the comparison between the two is not particularly helpful. [52]

Langer et al. [53] conducted research to validate high strain-rate modeling of LSP via the Johnson-Cook material model in aluminum and titanium. The strain rates in LSP greatly exceed those of the split Hopkinson bar testing used to determine the Johnson-Cook material model. As such, it was a valuable step to determine if the sole use of

Johnson-Cook parameters could accurately predict the results of the higher strain rate flyer plate test. The results were all within 15% of actual strain values, most within 10% and some within 5%. Further, the addition of the Mie-Grüneisen EOS resulted in minimal improvement of the accuracy of the models. [53] These results are particularly important to this body of work as the paper used the same FE code and modeling techniques utilized herein.

Halilovič et al. [54] performed FE modeling of LSP in 304 austenitic stainless steel. This is an alloy in which plastic deformation can cause transformation to the martensitic phase, resulting in improved hardness not possible by way of heat treatment. The FEM used an axisymmetric model surrounded by infinite elements on all but the LSP treated side. The pressure impulse from the work was rather unique, involving an inverse exponential taper to zero at the edge of the laser spot (reflecting a partial Gaussian distribution) and an instantaneous max pressure plateau followed by exponential decay in the time domain (see Figure 3 for visual representation of the impulse shape). This impulse shape is rather unusual, and is unlikely to represent reality, at least in the time domain, though it demonstrates the need for a better characterization of the pressure impulse to accurately model LSP. The entire simulation was done with Abaqus implicit integration using extremely small time steps to account for the highly dynamic effects of the process. Figure 3 shows in (a), the Gaussian spatial pressure profile (p(r)) over the LSP radius (r_0) and in (b) the pressure profile through time with respect to maximum pressure p_{max} and the laser shut-off time τ.

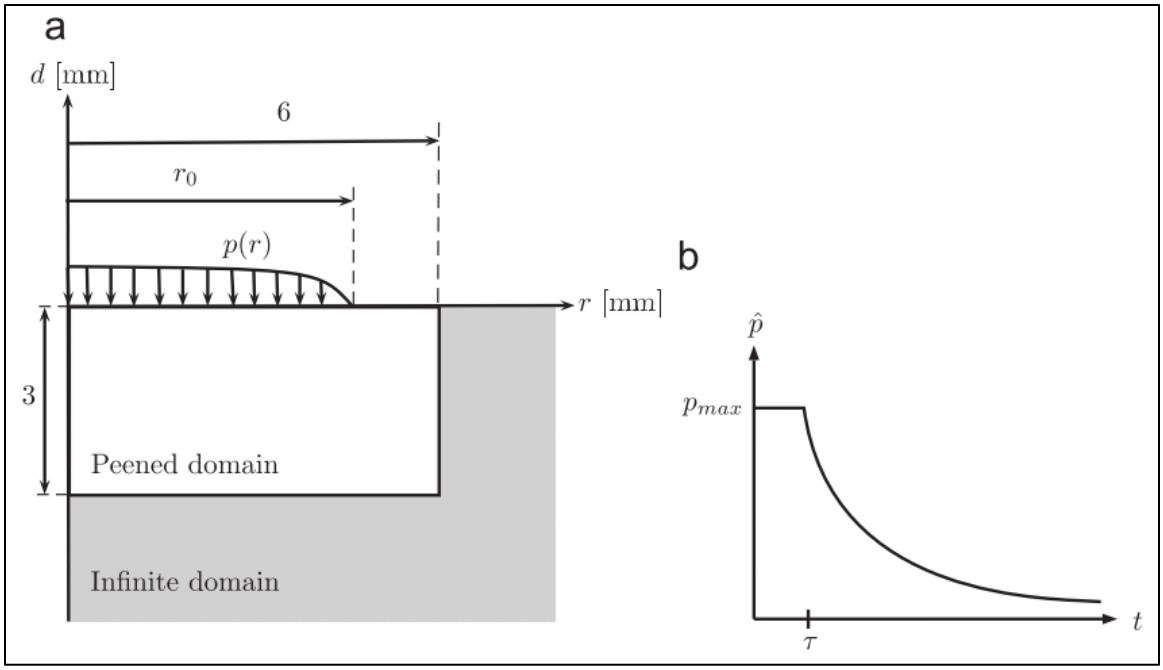

Figure 3: Spatial (a) and temporal (b) pressure impulse shape used by Halilovič et al. [54]

The material model was a constitutive strain rate-dependent model with the addition of a temperature dependent stress threshold to trigger the martensitic phase transformation. The results qualitatively showed increased amounts of martensite at higher pressures, larger spot sizes, longer impulse durations, and cooler ambient temperatures. As martensite forms at higher imparted stresses, all of these factors (with the exception of ambient temperature) imply stresses deeper into the substrate and reinforce prior findings. Further, the paper serves as another method of material modeling (*UMAT in Abaqus) which can be used with implicit integration if explicit is not well suited for the intended purposes (and thus the Johnson-Cook material model is unavailable). [54]

A study out of the University of Nebraska Lincoln [55] simulated a hybrid manufacturing technique using selective laser melting and LSP to optimize titanium material properties. The material model for the work was a user-input, temperature

dependent, tabular data with a full thermal heat flux model. The material mesh was built up by layer to represent the selective additive melting of the process. The LSP pressure impulse was modeled as a simple triangular pulse in the time domain and a partial Gaussian distribution radially reaching a bit less than half pressure at the outer edge of the laser spot. The paper modeled three different additive layer thicknesses, all stacked up three layers on a fixed substrate. After each layer application, the LSP treatment was applied and residual stresses after each layer-LSP treatment for both 1 GPa and 2 GPa LSP pressures were compared. While it was stated that tensile residual stress develops between layers, no controlled model was used (without LSP treatment) to show this. The comparison between two LSP peak pressures, however indicated that the LSP was beneficial to the process, as the lower pressure treatment reflected tensile stress between layers, and the higher pressure LSP treatment resulted in reduced tensile, or even compressive stresses within the layers. The material model of the work is certainly not complete enough, particularly in strain rate dependence to accurately model LSP treatment. Further, the paper is another example of the need for a more thorough characterization of the pressure impulse. Qualitatively, however, the work is good enough to show that LSP could be a valuable addition to additive manufacturing improve resultant residual stresses. [55]

A 2016 paper by Kamkarrad and Narayanswamy [56] researched the modeling of LSP on biodegradable magnesium orthopedic implants. These implants can corrode within the body, resulting in failure before the supported bone has healed, and compressive residual stresses via LSP were proposed as a solution to this problem. The

work was original in the use of a very small laser spot (just 40 μm), and a very high pulse repetition rate of 10,000 Hz, as opposed to a more standard rate of 10 Hz. This required careful timing of the explicit to implicit hand-off used in the Abaqus model, so as to allow enough time for kinetic energy to fully dissipate. The material model in the paper involved an elastic perfectly plastic model based on HEL dynamic yield limits. The work was also another to utilize a pressure impulse with a partial Gaussian distribution, reaching just over half pressure at the outer edge of the spot. In the time domain, the pressure impulse was modeled in shape somewhere in between a triangular pulse and SRT shape. This adds yet another impulse shape to the discord within the LSP modeling world. For a single shot case, the work was validated against experimental data by comparing dimple volumetry and maximum residual stresses. The magnitude of maximum displacement was only slightly over predicted, however experimental data was not nearly as uniform as the model, likely due to grains not much smaller than the dimple itself. The residual stress magnitudes did not, however reach the depths observed in past work. The real crux of the model accuracy in the work stems from the ability to handle the very fast repetition rate properly, an aspect not yet researched in the paper. [56]

Hasser et al. [57] conducted some very thorough work to improve the computational time of explicit only FE modeling of LSP, and apply these methods to optimization of LSP treatment for bending specimen fatigue life. The work featured a two-step method of explicit integration modeling with a time-dependent damping applied during the second step to speed up the settling time. The pressure impulse step remained unchanged, utilizing explicit integration to capture all of the dynamic effects of LSP. A

second explicit step was added in which a mass-proportional Rayleigh damping was applied to only the elastic behavior, and varied with time to damp both high and low magnitude strain energy, more quickly achieve a quasi-static equilibrium, and move on to the next laser pulse. When compared to the two explicit plus one implicit step simulation, which relied on constant damping, the explicit time-dependent damping method resulted in computation time was reduced by more than 80%. This savings paved the way for LSP optimization of fatigue life with improved model reliability based on the uncertainty of random process variables. The reliability portion of the paper is extensive, and goes beyond the scope of the intended area of study for this body of work, though it should certainly be taken in to account as FE modeling of LSP becomes more consistently reliable. The material model for the work was the Johnson-Cook model and the pressure impulse followed an SRT shape in the time domain. Spatially, the pressure impulse followed a rather unique profile in which the middle of the spot was subjected to a bit less than 90% of peak pressure, and the outer portion of the spot received peak pressure with a sharp drop to zero pressure near the edge of the spot (see Figure 4). This profile was assumed based on the measured laser irradiance profile from prior work [58], which interestingly mentioned that a uniform profile assumption was likely sufficient. In any event, this is yet another example of pressure impulse assumptions based on varying data sources within the LSP field. [57] Figure 4 shows the pressure profile across the radius of the LSP spot (a) as well as the laser irradiance profile from which this assumed profile was taken (b).

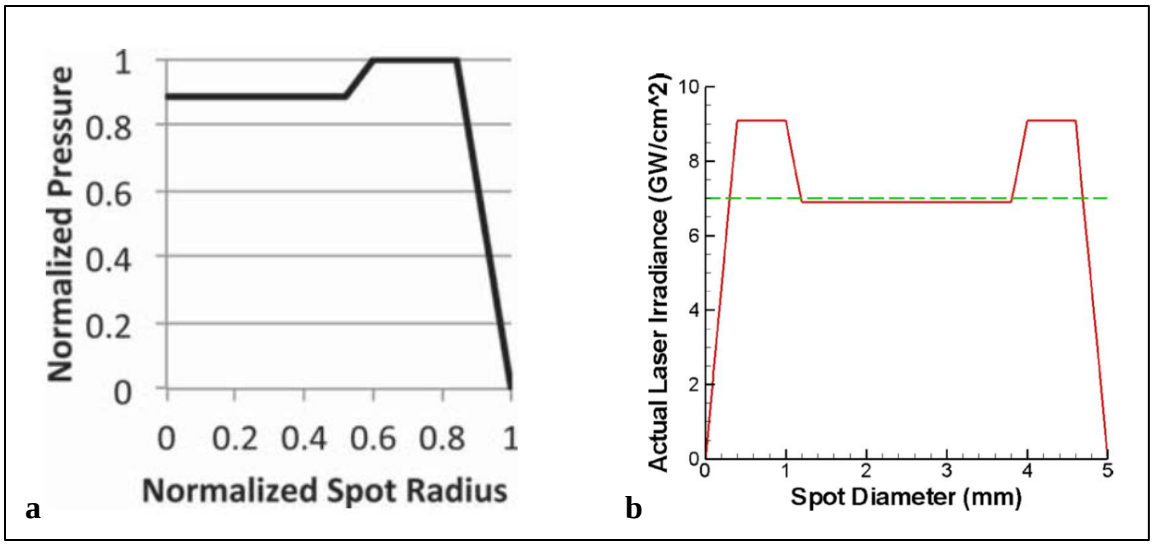

Figure 4: Pressure profile from Hasser et al. (a) [57] **laser irradiance profile from Cao et al. (b)** [58]

Work by Wang et al. [59] explored the numerical modeling of LSP on copper. The work modeled a circular disk using quarter symmetry with infinite elements around the perimeter, but a fixed back surface. The material model utilized a user input constitutive model based on a flow stress model for metals with face centered cubic crystalline structure. This model incorporated strain-rate dependent Von-Mises yield surface. It is unclear, however, from where the material constants were determined, and this could influence the accuracy of the model at the very high strain rates expected in an LSP event. The model was only validated for one strain rate (notably lower than those seen in LSP), the accuracy of which was off by more than 10% over much of the stress strain curve. The pressure impulse for the work utilized a Gaussian distribution across the radius of the spot, and a piecewise numerically defined SRT profile over the time domain. A parametric study was completed for the paper, varying the impulse duration and peak pressure. The results from this work reinforced past results in that higher pressure, and longer duration result in greater dimple volume and larger residual stresses.

Validation of a single laser spot was done by comparing surface displacement. For single laser pulse, the maximum depth of the dimple matched fairly well, but diverged for cases of subsequent pulses over the same spot. The radial profile of the experiment compared to the model did not match very well, particularly in terms of the dimple width. The radius of the modeled pressure profile was reduced to achieve a better match. [59]

Je et al. [60] modeled LSP for very small scale hydroforming of fully submerged, very thin copper foils. The model consisted of a very small 3D, quarter-symmetric disk surrounded by non-reflecting boundaries (equivalent to infinite elements in prior work). The pressure load was set as a uniform distribution over the circular spot, and was modeled as a flat impulse over time, likely not representative of the reality of LSP. The material model considered dynamic yield based on HEL, and incorporated a power law strain rate dependency similar to the Johnson-Cook strain rate dependent part, but modifying the effective stress state. This model was a reasonable approximation, but not as empirically based as the Johnson-Cook model. Validation of the work was accomplished through surface displacement, for which the model predictions deviated from experimental data by more than 30% in many places. The work further demonstrated the need for more standardized modeling practices. [60]

A piece of work out of Jiangsu University in China [61] modeled the effects of LSP overlap rate on stress relaxation for cyclically loaded aluminum. It is an important modeling effort, as the relaxation of LSP imparted residual stresses over many cycles directly affects the fatigue life of the treated specimen. A quarter symmetry model was used here, with a nine laser spot overlapping pattern for which the amount of spot overlap

was varied in the study. The pressure impulse in the work used the partial Gaussian spatial distribution and what seemed to be a near triangular impulse over time. The material model in the paper was not at all discussed which brings into question the ability to properly model both LSP as well as cyclic stress relaxation. Further, the cyclic loading appeared to be applied as a pressure over the same LSP treated area, and resulted in increased compressive stresses within the treated area except for one case. While these make the study unreliable for many aspects, it still demonstrates a lack of consistency in pressure impulse shape assumptions, and also demonstrated the commonplace use of an entirely explicit integration simulation. [61]

Very recent work by Frija et al. [62] modeled LSP in titanium in an attempt to optimize LSP parameters via DOE study. The work reflected many of the latest advancements and best practices in modeling. It utilized a biased mesh surrounded by infinite elements in an axisymmetric geometry. The simulation was run over a single explicit step in Abaqus. The material model incorporated Johnson-Cook plasticity with the unique addition of the Johnson-Cook damage criteria. This addition allows the mesh accumulate damage and eventually rupture, resulting in zero stress-carrying capacity. The pressure impulse was modeled as uniform over the laser spot and followed an SRT profile over time. The model was validated by comparing residual stress into the depth of the treated specimen, and the model compared very well with experiment, only slightly under predicting the depth of the residual stress field. The thorough DOE study ran a full factorial study, varying maximum pressure, spot diameter, and full width half maximum (FWHM) pressure impulse peak width, that is the width of the pressure spike when

measured at a pressure value half that of the maximum value reached. Each of these five variables were tested over five levels and the results analyzed were maximum residual stress, surface stress, compressive stress depth, maximum damage, and maximum plastic equivalent strain. The study revealed that moderately high peak pressure, applied over shorter impulse duration resulted in higher surface residual stresses while minimizing surface damage. This can be readily applied to structures such as titanium turbine blades where hardness is ideal, but surface damage could result in adverse aerodynamic influences. [62]

There are a number of takeaways from this review of FEM development in the field of LSP. First, the acceptance of Johnson-Cook material properties for modeling LSP is commonplace due to the ability to handle high strain rates, its foundation in empirical data, and its availability in most commercial FE codes. The addition of some form of EOS, typically Mie-Grüneisen, is optionally used, depending on the magnitude of peak pressures in the model. In terms of software technique, Abaqus is commonly, though not exclusively used, and any number of combinations of explicit and implicit steps can be useful in handling different scenarios, and for balancing model accuracy as well as computational cost. Of late, higher performance computer systems are able to handle single explicit step simulations, though the splitting of this process into dual explicit step to reduce the kinetic energy settling time is somewhat appealing due to computational savings. Further, it has become rather commonly assumed, though not uniformly consistent, that the pressure impulse is some form of partial Gaussian profile spatially across the spot, and using a variant of the SRT profile across time. Though

these assumed shapes are common, there are many other varieties of impulse shape throughout the field, and all are still assumptions based on very little experimental measurement. Fundamentally, the aforementioned reliance on an assumed pressure impulse is the source for much variation within LSP modeling work, and points to the need for a better link to determination of this phenomenon.

Measurement of LSP Artifacts

It becomes apparent now that the validation of any LSP model with experimental data is typically accomplished through the measurement of surface displacement (dimple) profile and/or residual stress. A few attempts have been made at measuring different parameters during the LSP event to deduce the pressure impulse or validate the FE model. In any event, the physical methods used to measure these metrics are of particular importance to this work as they are the source of the "target" for the optimization algorithm. The following will address first, work which has undertaken the measurement of conditions during the LSP process then, methods of measuring the material results of LSP.

It would be ideal to directly measure the pressure impulse in both time and space so that it could be directly applied to the FE model. Recall, however, that the entire event takes place over the course of just a few hundred nanoseconds, so the sample rate to record the impulse in sufficient resolution would have to be many gigahertz. Further, the modification of the process to measure the pressure could inherently change the material results of the treatment. The measurement of the LSP pressure impulse, or its direct results has been tested in a few different ways.

The earliest research on the topic used piezoresistive momentum transducers to measure laser pulse energy over time, though this does not necessarily directly correlate to pressure profile over time [5]. Later work got a bit closer by attaching quartz piezoelectric transducers to the back of thin samples to measure the deformation of the sample [11]. When run through an oscilloscope, this provides excellent temporal resolution, but does not directly measure pressure, and is highly dependent on specimen thickness. These methods were reviewed using modern digital oscilloscopes more recently as well, with similar results [3]. The same technique has also been utilized by measuring thin specimen velocity on the back surface by way of VISAR during a single LSP pulse [38]. All of these methods can assist in better understanding of the general behavior of the pressure impulse, but are not directly measuring the pressure, and require a specific experimental configuration to collect the data. The same could not be accomplished when applying LSP treatment to an unusually shaped workpiece intended for engineering application.

Banas [63] conducted research in which polarized polyvinylidene fluoride (PVDF) transducers bonded to the metal directly below the ablative layer. This is perhaps as close as one can come to directly measuring the imparted pressure though it is still displaying the strain experienced by the gauge as a result of the pressure, and might interfere with the treatment of any material beneath the gauge. The process is also quite cumbersome to implement, and the final pressure results are highly dependent on the accuracy of the calibration curves supplied by the PVDF gauge maker. Further, the gauge voltage indicates the change in pressure, thus instantaneous pressure is determined

via integration, resulting in reduced temporal resolution of the pulse. The work was still quite useful in reinforcing the SRT impulse shape as closest to reality. [63]

In recent work [64], the bubble created by plasma expansion during LSP was observed and measured. One rather advanced piece of work utilized stroboscopic imaging of a polarized laser to observe shock fronts in the inertial water layer and the epoxy substrate as well as the cavitation bubble created in the water layer after the LSP pulse. This method achieved a rather high sample rate, and was quite useful at comparing the strength of shock waves between different laser power densities and ablative coating conditions. The energy of the cavitation bubble can be deduced by this method and is good for the same comparisons; however, determination of pressure is done by integrated calculation, and this still quite coarse temporal resolution leaves rather large uncertainty in even the peak pressures at the surface of the workpiece. Simply put, this method still cannot provide an accurate, time-resolved portrayal of the highly dynamic pressure impulse imparted into the specimen. Further, the method is quite complex and requires expensive equipment, making it impractical to apply to numerous LSP settings in an attempt to build an impulse "catalog." [64]

This same method was again researched in an effort to observe bubble oscillation as a form of process diagnostic [65]. The work was successful in using both the first oscillation of the bubble, as well as the collapse time of the bubble to deduce the energy transfer to the target material, though not directly resolving the time-wise shape of the pressure impulse. The technique was rather sensitive to water conditions, however, and noted inconsistent results at higher pressures. Again, this method requires expensive and

complex equipment to complete, and works only in fully submerged LSP, not the typical application method in industry today. [65]

It is now apparent that it is expensive and difficult to directly measure the pressure impulse, particularly in situ without influencing the material benefits achieved by the process. It is thus suggested that more easily measured material artifacts of the pressure impulse be used for this study. The most obvious material property changes due to LSP treatment include surface hardness, surface displacement, and residual stresses. The following will examine the viability of each of these parameters for use in LSP model validation and deducing the pressure impulse shape in time and space.

Surface hardness is a very easily measured material property which can readily be compared before and after a surface treatment. It has been used in a significant amount of research to assess LSP benefits, as well as compare model to experiment [66]–[74]. Vickers micro-hardness tests are even small enough to measure the hardness at multiple locations across the surface of a single LSP spot. Hardness usually changes by relatively small amounts (as little as 15%), and the mechanisms by which hardness change include strain hardening, strain-rate hardening, as well as residual stress [66]. This would make it difficult to deduce a single pressure impulse shape which would result in changes to the measured hardness.

Almen test strips, as are used to standardize conventional shot peening, have also been put to use in some LSP work [67], and are even suggested for use by the LSP material specification [4]. The curvature of these thin strips after the representative treatment is applied on one side provides an idea of the bulk stress field within the

undeformed material and can be useful for some process quality assurance. The results of an Almen strip test will be indicative, however, of the quality of the entire process, from laser settings to shot pattern size and density. Thus it carries little value for deducing the pressure imparted by a single pulse. It could, however, later be used as a secondary form of validation when the deduced pressure impulse is modeled in a pattern arrangement for specific engineering applications.

As previously mentioned, surface deformation, or dimple profilometry has been commonly used as a means of validating LSP modeling. The indentation formed by a given LSP setting, in a given material is fairly consistent, and the measurement of this dimple has even been patented by GE as a means of quality assurance [22]. A profilometer is a common piece of equipment, easy to use, and accurate enough to measure small displacements. This work will utilize surface displacement (dimple profilometry) as one of the forms of empirical data which the optimization code will seek to match.

The other most common means for validating LSP modeling is via the resultant residual stress field within the treated specimen. Residual stresses are stresses hidden within a material not acted on by an outside force. The stresses are typically caused by non-uniformity of phase change, plastic deformation, or machining. The absence of an external load means that residual stress keep themselves in equilibrium via regions of compressive stress balanced by regions of tensile stress. To better visualize this effect, see the one-dimensional example on a stress-strain diagram in Figure 5.

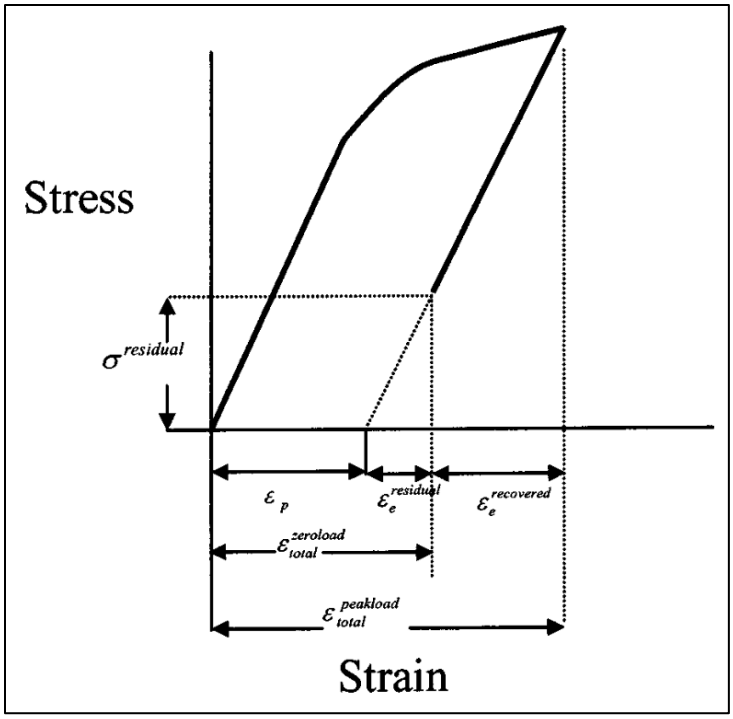

Figure 5: One-dimensional example of residual stress as seen on stress-strain diagram [75]

These regions vary in size and distribution, and thus must necessarily contain some stress gradient. Residual stresses have been shown to have both desirable and undesirable effects on structures. They can result in undesirable deformation or failure properties [76], [77]. They can also be useful, however, in counteracting stress concentrations that can reduce fatigue life. This is where LSP is advantageous, as it can impart residual stresses which prohibit crack propagation or minimize stress concentrations [78]. The challenge in measuring residual stresses is due to their hidden nature, but many reliable methods have been well established. There are two basic types of residual stress measurement: non-destructive and destructive. [79]

The non-destructive techniques measure crystal lattice spacing via diffraction of X-rays or neutrons. Electromagnetic radiation is diffracted when it passes through a

crystalline structure. Differing diffraction angles indicate different spacing within the crystal lattice, and thus reflect the elastic strain left within a specimen. As any residual stress necessarily shows up as linear elastic strain, this strain can be directly linked to the stress remaining within the material. X-ray diffraction (XRD) is the more common method, as X-rays are quite readily available. The method has become very mature, and portable devices can characterized residual stresses at very high resolution, very quickly, and in some cases even automatically. The limitation of these devices is the necessarily low intensity of the X-rays which can be produced by a portable (or even stationary) device. The penetration depth for such low intensity X-rays is quite small, and thus, portable XRD is really only effective at measuring residual stresses very near the surface of the material. One solution to this problem is a more intense beam of X-rays. This can be accomplished through the use of a synchrotron. The depth and resolution at which residual stresses can be measured via synchrotron XRD are unmatched, but the number of synchrotron facilities available for research are limited, and their time is difficult to procure. XRD in either form is diffraction by interaction with electrons, however the same principle can be applied to neutrons, which instead diffract via nucleal interactions. This means that neutron diffraction can easily penetrate quite deep into a material. [79] More recent developments in residual stress measurement have made use of neutron transmission spectroscopy. This method exhibits high spatial resolution in the 2D map of the average strain through which the beam passes. [80] In either method, however, the use of neutrons necessitates a reactor to produce them, and again, the number of facilities capable of such a measurement are limited in number and availability.

The current work had no need of reusing or further testing specimens, and thus an effective destructive residual stress measurement technique was perfectly acceptable, particularly in its ease and affordability. Destructive residual stress measurement techniques come in a large variety of forms. The fundamental principal of all is that the removal of some of the material containing residual stress creates an imbalance in the equilibrium and the surrounding regions will deform to regain that equilibrium. By measuring the resulting deformation, one can deduce the average residual stress which existed in the removed material. This method can also be applied incrementally to resolve the gradient of a stress field. Generally, these methods are fairly straight forward and affordable to apply, and utilize readily available equipment and gauges. They cannot resolve stresses at a scale as small as diffraction techniques, but can still work at increments quite smaller than the typical LSP spot width. The material removal can take many forms, most commonly a hole, ring, slit, or cut. Strain is measured in the immediate vicinity of the removed material and mathematics or finite element modeling is used to determine the residual stresses which must have existed in the removed material. In the hole-drilling case, a strain gauge rosette is place around the area of interest, and the strain is measured as a hole is drilled incrementally. Ring-coring is similar, also using a strain gauge rosette, but instead cutting a ring around the outside. Slitting involves strain gauges on either side of the slit as well as on the back surface of a plate. The slit is then cut to incremental depths while strain is measured. Finally, the contour method involves completely cutting the specimen in two pieces, measuring the cut faces with a profilometer, then using FEM to “push” the surfaces back to zero

displacement and compute the stress across the cut section. This method can be repeated on the same specimen to section it into multiple layers, adding another dimension to the stress characterization. [79]

The current research seeks a better link between LSP residual stress results, and the FEM prediction of those residual stresses. Thus, the method of residual stress measurement used herein must be simple, affordable, and accurate, with enough resolution to "look inside" a single LSP spot. Further the method must have a well-defined gauge volume such that it can be accurately replicated within the FE model. A number of different residual stress measurement methods were already noted in many works above, typically for FEM validation or to quantify the improvement imparted by LSP. XRD has been used to a great extent to measure residual stresses from LSP or other peening techniques [81]–[85]. XRD, however, can only measure to very limited depth, and is sensitive to surface texture and grain uniformity. The following research summary addresses some of the methods which show the most promise to accurate FEM correlation.

Pagliaro et al. [86] explored the superposition of multiple residual stress measurement methods. Every measurement method has strengths and weaknesses; overlapping a combination of methods can help to balance these out in a more thorough characterization of the residual stress field. The paper worked with large piping, for which residual stress measurement is quite difficult. The introduced method first cuts the specimen for characterization via contour method, then uses hole-drilling into the cut face and superimposes the results from the two steps. To validate the results the work used

neutron diffraction as a comparison. The method seems a promising idea, but proved rather inaccurate because the cutting method itself leaves additional residual stresses in the specimen which must be removed by some zero-stress process. [86]

Winiarski et al. [87] researched very high resolution methods of measuring residual stresses around challenging geometric features such as notches. The work measured residual stresses induced by traditional shot peening, but the application is universal. The pairing of very small hole-drilling or slot cutting with electron microscope maps of grain topography allowed measurement of residual stresses in very small volumes. The results showed a great deal of fluctuation at the surface, but the measurement of residual stresses below the surface agreed very well with XRD data. This method, however, requires an electron microscope for the strain measurement, and is thus, still quite complex to implement. [87]

Residual stress measurement has indeed become quite mature of late, and there are many trusted methods available. For the purposes of this work, due to the size of a single LSP spot to be measured, the hole-drilling method seems the best-fit. It is easily implemented and inexpensive. It can measure with a spatial resolution much less than the size of a single spot and is well trusted within the field.

Summary

This chapter has properly introduced the field of LSP, explaining the process and its history. Having looked at a great deal of key literature, particularly recent work which has contributed to the field of LSP and related topics, the following points should be reemphasized. First, the material benefits of LSP for work hardening, surface

improvement, and particularly fatigue life improvement are well researched and show the value of the process. Also, the modeling of LSP has come quite far to date. Many standard practices are apparent, for example the use of Johnson-Cook material properties and explicit modeling. The particular shape of the pressure impulse in time and space, however, is not uniformly agreed upon. Many forms of pressure across the width of the laser spot have been used, and though the SRT profile in time is generally agreed upon, the precise pressure function through time has never been directly measured or determined. This points to the need for a way to deduce the pressure impulse shape imparted by a single LSP pulse. Finally, many measurements can be made to characterize the effects of LSP in a material. Some in situ measurements have been made, but are not easily implemented be used regularly. LSP dimple profilometry as well as measurement of residual stress via hole-drilling were of great interest to this work as the "target" of the optimization code to deduce the pressure impulse shape. These measurements can be taken easily and averaged over multiple LSP spots on a single test specimen, and they do not modify the LSP process to collect the measurements. The objective of the current work was, again, to build a stronger connection between FEM and the empirical residual stresses imparted by LSP. Optimization code was used to determine a "best-fit" pressure impulse shape in both time and space which accurately matched the empirical surface displacement and residual stress "target" data. This deduced pressure impulse was then applied to a second material and the FEM predicted dimple volumetry and residual stress was compared to experimental results for validation. This method is a first step in the ability to "catalog" pressure impulse shapes which

correspond to certain settings in a laser system, and which could be applied in the FE model for better prediction of the resultant residual stress field for a specific application.

II. Theoretical Foundations

Chapter Overview

This chapter will establish the theoretical foundations which are necessary to underpin the key elements of this work. It will cover the numerical development of the finite element model, the material properties used in the model, and the physical guidelines of the pressure impulse applied in the FEM. Further, it will touch on the optimization methodology used here, and the fundamental principles of the measurement techniques used to collect the empirical data.

Finite Difference, Finite Element Modeling, and Material Properties

The way by which LSP imparts residual stress is as follows. First, a very short duration, extremely high pressure impulse is applied to the surface of the material. This imparts a stress wave which exceeds the HEL of the material, causing elastic and plastic strain within the solid. When the event is complete, a permanent deformation has occurred in a small portion of the solid. The localized elastic strain remaining from this deformation can be used in conjunction with Hooke's law to determine the residual stress remaining in the material. These are elastic self-equilibrating stresses contained internally to the model without any external forces applied. The highly dynamic LSP event requires a fully explicit integration FE model to handle the shock events and the time dependent behavior of the materials under these high strain rates. Nodes in the finite model can be treated as lump masses and their position, velocity, and acceleration can be

determined by way setting the sum of forces equal to the mass times the acceleration from one time step to the next via the finite difference method. This requires understanding of the forces (both internal and external) acting on the node. External forces come from the applied pressure function, however internal forces must be found by way of explicit finite element integration over the shape functions of the volume of elements surrounding each node. The following sections will outline the finite difference method in the context of a finite element model as well as how viscoplasticity and EOS are inserted into the material response to the highly dynamic LSP event.

The central finite difference scheme determines the acceleration, velocity, and displacement for every node at incremental time steps explicitly. Time step increments are indexed with superscript notation (i), beginning at $i = 0$ (initial dynamic & boundary conditions) and progressing forward by the defined time increment in the finite difference scheme (discussed later). First, nodal displacement at the current time step ($u^{(i)}$) relates to the strain tensor ($\varepsilon^{(i)}$) via the strain displacement matrix ($\boldsymbol{B}$) which relates every displacement degree of freedom to the element strain via the element shape functions.

$$\varepsilon^{(i)} = \boldsymbol{B} u^{(i)}$$

The elastic strain (${\varepsilon_e}^{(i)}$) is then determined by simply subtracting the plastic strain at the current time step ($\varepsilon_p^{(i)}$) if it exists (this would be known at the start of the step and will be discussed more in depth later).

$${\varepsilon_e}^{(i)} = \varepsilon^{(i)} - \varepsilon_p^{(i)}$$

The elastic strain relates to the stress state ($\sigma^{(i)}$) via Hooke's law (elasticity matrix, $\boldsymbol{D_E}$).

$$\sigma^{(i)} = \boldsymbol{D_E} {\varepsilon_e}^{(i)}$$

The stress state is used to determine the internal forces at the current time step ($P^{(i)}$) in the following way.

$$P^{(i)} = \int_V \boldsymbol{B}^{\top} \sigma^{(i)} dV$$

These internal forces as well as any externally applied forces ($F^{(i)}$ from pressure or point loads) act on a diagonalized mass matrix (M) and drive the nodal acceleration for the current time step ($\ddot{u}^{(i)}$).

$$\ddot{u}^{(i)} = \boldsymbol{M}^{-1} \cdot (F^{(i)} - P^{(i)})$$

The central difference method used in Abaqus keeps track of nodal velocity at "half steps" to differentiate from nodal position and acceleration. In this case, the nodal velocity from the previous half step ($\dot{u}^{(i-1/2)}$) would be the initial dynamic conditions ($\dot{u}^{(0)}$) but for subsequent iterations the half-step velocities will be explicitly known. Together with the nodal acceleration just calculated, this can be used to calculate the nodal velocity at the next half step ($\dot{u}^{(i+1/2)}$).

$$\dot{u}^{(i+1/2)} = \dot{u}^{(i-1/2)} + \frac{\Delta t^{(i+1)} + \Delta t^{(i)}}{2} \ddot{u}^{(i)}$$

Finally, with the subsequent nodal velocity known, the nodal displacement at the subsequent step ($u^{(i+1)}$) can be calculated.

$$u^{(i+1)} = u^{(i)} + \Delta t^{(i+1)} \dot{u}^{(i+1/2)}$$

Now with the subsequent nodal velocity and displacement determined, as the name suggests, the model can be solved explicitly for the next time step and so on. Note that

this method allows for a different time increment for every step. The minimum stable time increment (Δt_{stable}) for any given element is dictated by the element length (L^e) in relation to the material sound speed (C_d) as follows.

$$\Delta t_{stable} = \frac{L^e}{C_d}$$

Where the material sound speed is defined with relation to the material modulus (E), and density (ρ).

$$C_d = \sqrt{E/\rho}$$

Thus the stable time step of the entire model depends on the length of the smallest element, and can change from step to step as the element changes length under load. Further, the method is only conditionally stable based on this minimum time step, and larger time steps will cause the solution to diverge. Also, this is why adjacent time steps are averaged when multiplying by the nodal acceleration at any given half step. This flexibility of time step allows Abaqus to "see" the dilatational wave speed through the smallest element under changing conditions. [88]–[90]

In a purely elastic case, the above central difference method is all that would be needed to handle the deformation. In a plastic or viscoplastic scenario there must be a way to handle non-linear plastic or viscoplastic strain at each time increment. The von Mises yield criterion is used for incremental plastic strain, and the Johnson-Cook model relates the equivalent stress ($\bar{\sigma}$) to the equivalent plastic strain ($\bar{\varepsilon}_p$) and equivalent plastic strain rate ($\dot{\bar{\varepsilon}}_p$) and with respect to temperature (T) via the following equation [91].

$$\bar{\sigma} = \left[A + B\bar{\varepsilon_p}^{n}\right]\left[1 + C\ln\left(\frac{\dot{\bar{\varepsilon}}_p}{\dot{\varepsilon}_0}\right)\right]\left[1 - \left(\frac{T - T_0}{T_m - T_0}\right)^{m}\right]$$

This plastic flow law contains material constants A, B, C, n, and m, which are curve fit to empirical results from monotonic tensile, Split Hopkinson Bar, and Flyer Plate tests. Other material properties include the reference strain rate ($\dot{\varepsilon}_0$) below which quasi-static strain hardening governs the behavior, and melting temperature of the metal (T_m). The reference temperature (T_0) is room temperature. [91]

Fundamentally in terms of equivalent stress and equivalent plastic strain, the material model behaves as follows. At room temperature, and very low strain rates, the yield stress will be equal to constant "A", and the plastic strain hardening will be governed by the $B\varepsilon^n$ power law once this yield stress is exceeded. This power law can also be "scaled up" to higher dynamic yield power laws by using the strain rate (middle) term of the equation. At strain rates higher than the reference strain rate, this middle part of the equations becomes greater than one, increasing the dynamic yield stress as well as the strain hardening effects. In a similar way, at elevated temperatures, the third portion of the equation becomes less than one and "softens" the strain hardening of the first part of the equation. These equations fit quite well to the behavior of metallic materials, but are limited by the empirical data which can be collected, as it must necessarily be taken across the range of strain rates and ambient temperatures to be modeled. Industry standard LSP treatment is typically done in a way which does not impart significant temperature change into the material. Thus, the strain hardening and strain rate portions of the equation are used, but the temperature effects are not required.

It is important to understand that the Johnson-Cook equation relates scalar values of equivalent stress to equivalent plastic strain (designated by a bar notation), however, the stress state for the explicit integration is a 2nd order tensor. The components of the deviatoric stress tensor (s_{ij}) relate to the scalar equivalent stress as follows.

$$\bar{\sigma} = \sqrt{\frac{3}{2}\left({s_{11}}^2 + {s_{22}}^2 + {s_{33}}^2 + 2{s_{12}}^2 + 2{s_{13}}^2 + 2{s_{23}}^2\right)}$$

Or, in terms of principal stresses the equivalent stress is calculated in the following way.

$$\bar{\sigma} = \sqrt{\frac{1}{2}[(\sigma_1 - \sigma_2)^2 + (\sigma_2 - \sigma_3)^2 + (\sigma_3 - \sigma_1)^2]}$$

Note, also, that the stress tensor at the given time increment ($\sigma^{(i)}$) is deviatoric stress. For any arbitrary stress tensor (σ_a), the hydrostatic pressure does not contribute to the yielding of the material but will be handled for the purposes of shock propagation by an equation of state (EOS) highlighted later. The deviatoric stress tensor is calculated from an arbitrary stress state by subtracting the average of the trace values of the stress tensor times the identity matrix. [88]–[90]

$$\sigma_{dev} = \sigma_a - \frac{1}{3}Tr(\sigma_a)I$$

To fit this plasticity into the explicit FE method the von Mises equivalent stress state at the current time step ($\bar{\sigma}^{(i)}$) is calculated and compared to the Johnson-Cook yield stress ($\bar{\sigma}_y$) to determine if yield has occurred for the current strain and strain rate.

$$\bar{\sigma}_y = \left[A + B{\bar{\varepsilon}_p}^n\right]\left[1 + C\ln\left(\frac{\dot{\bar{\varepsilon}}_p}{\dot{\bar{\varepsilon}}_0}\right)\right]\left[1 - \left(\frac{T - T_0}{T_m - T_0}\right)^m\right]$$

If the equivalent stress is less than the yield stress, then yield has not occurred, and the subsequent equivalent plastic strain rate ($\dot{\bar{\varepsilon}}_p^{(i+1/2)}$) remains zero. If yield has occurred, and for strain rates above the reference strain rate, the subsequent equivalent plastic strain rate is calculated as follows.

$$\dot{\bar{\varepsilon}}_p^{(i+1/2)} = \dot{\bar{\varepsilon}}_0 exp\left[\frac{1}{C}\left(\frac{\bar{\sigma}_y}{\bar{\sigma}_0} - 1\right)\right]$$

Where quasi-static equivalent yield stress ($\bar{\sigma}_0$) is defined as follows.

$$\bar{\sigma}_0 = \left[A + B\bar{\varepsilon}_p{}^n\right]\left[1 - \left(\frac{T - T_0}{T_m - T_0}\right)^m\right]$$

This strain rate is a scalar quantity, however, and needs a "direction" in which to travel. The plastic strain follows the unit vector normal to the current yield surface, which is now one and the same with the current deviatoric stress. Thus, plastic strain rate can then be used to calculate the subsequent plastic strain ($\boldsymbol{\varepsilon}_p^{(i+1)}$).

$$\boldsymbol{\varepsilon}_p^{(i+1)} = \boldsymbol{\varepsilon}_p^{(i)} + \dot{\bar{\varepsilon}}_p^{(i+1/2)}\boldsymbol{n}\Delta t^{(i+1/2)}$$

Where the tensor normal ($\boldsymbol{n}$) is equal to the normal of the deviatoric stress tensor (σ).

$$\boldsymbol{n} = \frac{3}{2}\frac{\sigma}{\sqrt{\frac{3}{2}\sigma : \sigma}}$$

If the equivalent plastic strain rate is below the reference strain rate, the plastic strain can be directly calculated from the first portion of the Johnson-Cook equation.

$$\boldsymbol{\varepsilon}_p^{(i+1)} = \boldsymbol{n}\left[\frac{1}{B}\left(\bar{\sigma}^{(i)} - A\right)\right]^{1/n}$$

The plastic strain rate is then simply equal to the equivalent plastic strain divided by the time step.

$$\dot{\varepsilon}_p^{(i+1)} = \frac{\bar{\varepsilon}_p^{(i+1/2)}}{\Delta t^{(i+1/2)}}$$

The incremental plastic strain can then be related via the strain-displacement matrix to additional nodal displacement ($\Delta u^{(i+1)}$) which is added to the overall nodal displacement for the following step. The plastic strain and equivalent plastic strain rate are also carried through to the following time step and this is repeated for each time increment. [88]–[90] The entire flow of this FEM method is succinctly summarized in the following diagram (Figure 6) recently developed by Buentello-Hernandez [89]. The diagram encompasses everything discussed thus far, and also Johnson-Cook damage criterion, not necessary for the analysis as no wear or fracture is imparted by LSP best-practices.

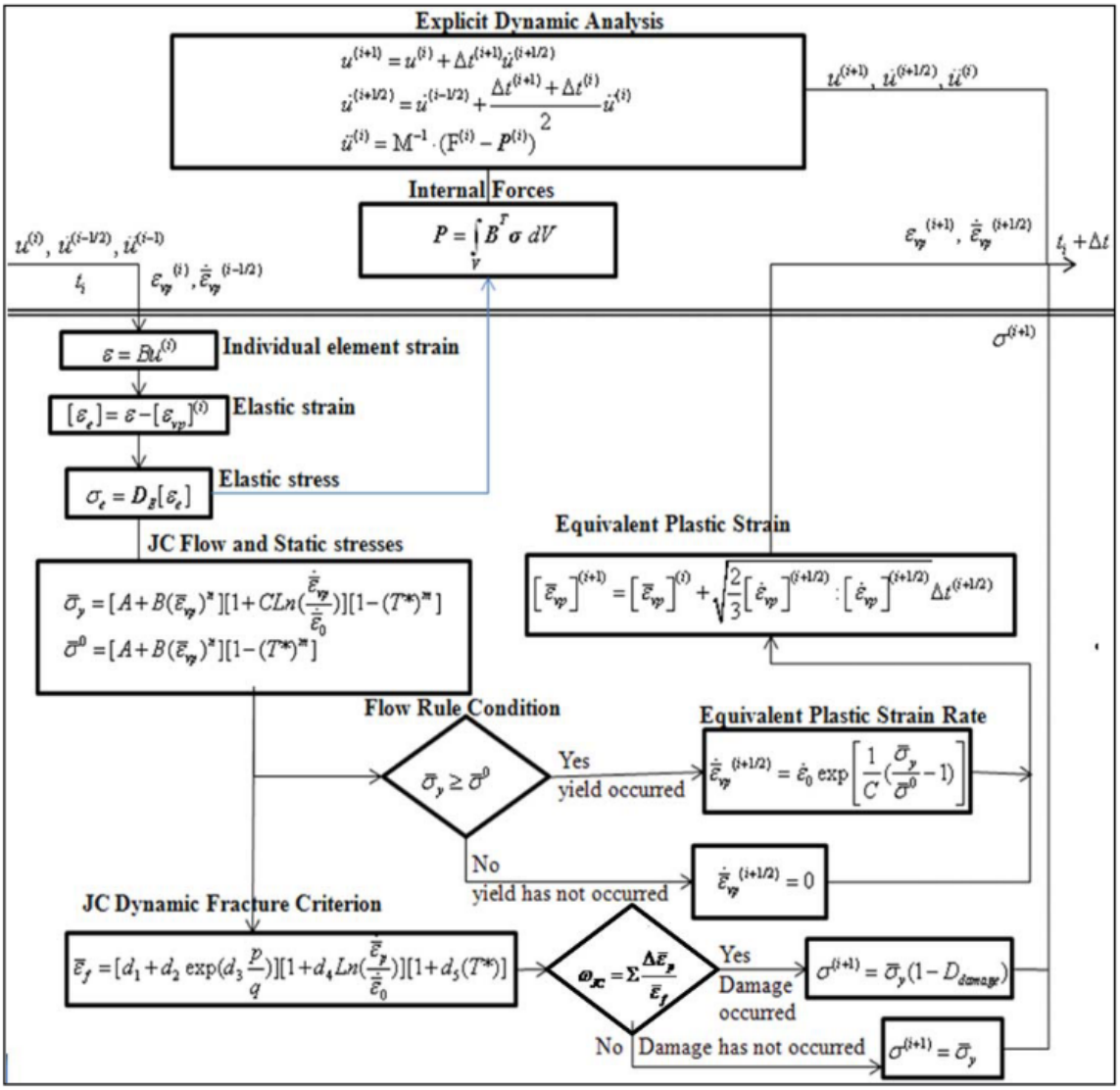

Figure 6: Explicit nodal central difference analysis for elastic/viscoplastic analysis in Abaqus [89]

Under extremely high pressures (as experienced in an LSP event) even metallic alloys begin to behave in a more fluid manner. The Johnson-Cook material model handles only deviatoric equivalent plastic strain but cannot account for hard shock propagation. The Mie-Grüneisen EOS can be used to handle the hydrostatic compression

in conjunction with the Johnson-Cook model. The hydrostatic pressure is traced by the following equation. [88]

$$P = \frac{\rho_0 {c_0}^2 \eta}{(1 - s\eta)^2}\left(1 - \frac{\Gamma_0 \eta}{2}\right) + \Gamma_0 \rho_0 E_m$$

Where Γ_0 is the Mie-Grüneisen constant, s is the Hugoniot slope coefficient (a material property), c_0 is the material speed of sound, E_m is the internal strain energy, and the nominal volumetric compressive strain (η) relates the instantaneous density (ρ) to a reference density (ρ_0) as follows. [88]

$$\eta = 1 - {\rho_0}/{\rho}$$

This EOS model also assumes a linear relationship between the shock velocity (U_s), and the particle velocity (U_p) in the following way. [88]

$$U_s = c_0 + sU_p$$

Pressure Impulse Formation

The LSP pressure impulse is the result of sudden plasma formation from a laser burst. While the specifics of the plasma formation would be an excellent topic for a physicist, for the purposes of this work it is best to start with the shock propagation caused by the resultant pressure, considered in the following simple 1D case established by Fabbro et al. [38] Figure 7 shows this simplified 1D shock propagation in which an expanding plasma bubble results in a shock travelling through the metallic substrate at speed D_1 and the inertial (glass or water) overlay at speed D_2. Material particle velocities at the surface are then characterized as u_1 and u_2 accordingly. [92]

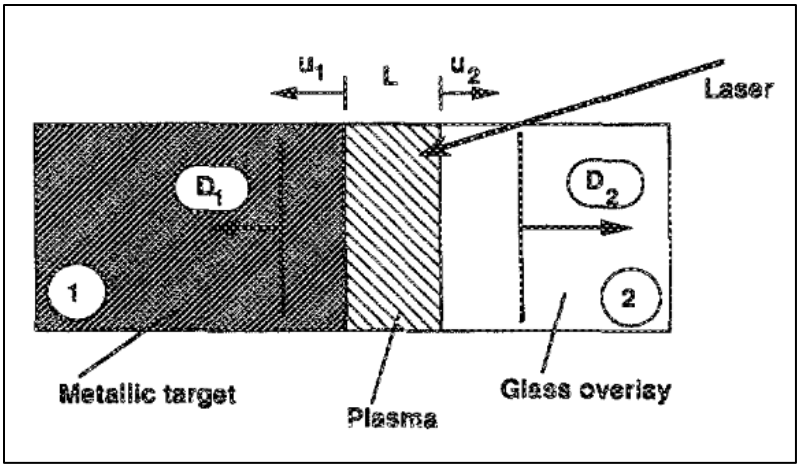

Figure 7: 1D shock propagation from LSP pressure impulse [92]

The thickness of the plasma "bubble" ($L(t)$) can be found by integrating the particle velocities (u_i) in both mediums (1 and 2) behind the shock as in Figure 7. [92]

$$L(t) = \int_0^t [u_1(t) + u_2(t)]dt$$

These particle velocities relate to the pressure (P) via the material density (ρ_i) and shock velocity (D_i) in the following way. [92]

$$P = \rho_i D_i u_i$$

For materials other than gasses, minimal compressibility and constant shock velocity can be assumed, resulting in the following relationship. [92]

$$\frac{dL(t)}{dt} = \left(\frac{1}{D_1\rho_1} + \frac{1}{D_2\rho_2}\right)P(t)$$

While the laser is switched on, the increase in internal energy ($E_I(t)$) is imparting work proportional to the laser intensity ($I(t)$) as follows. [92]

$$I(t) = P(t)\frac{dL}{dt} + \frac{d[E_I(t)L]}{dt}$$

A fraction (α) of this internal energy is thermal energy, giving the following gas equation. [92]

$$P(t) = \frac{2}{3}\alpha E_I(t)$$

This gives a final equation as follows. [92]

$$I(t) = P(t)\frac{dL(t)}{dt} + \frac{3}{2\alpha}\frac{d}{dt}[P(t)L(t)]$$

The laser is then switched off at time $t = \tau$ and, if adiabatic cooling is assumed, the resultant pressure follows this equation. [92]

$$P(t) = P(\tau)\left(\frac{L(\tau)}{L(t)}\right)^{\gamma}$$

In this equation γ is the specific heat ratio in the plasma "bubble" and the thickness of the bubble is now given by the following equation. [92]

$$L(t) = L(\tau)\left(1 + \frac{(\gamma+1)}{\tau}(t-\tau)\right)^{\frac{1}{(\gamma+1)}}$$

These equations can be solved analytically for a specific case if the laser intensity profile function ($I(t)$) is assumed. It should be noted that included in the function for the pressure peak is the density and sound speed of the material it is acting on, often combined to be call the "shock impedance" of the material. That is to say that for a given laser intensity profile, the pressure response to the laser burst on materials with different shock impedance will vary by the root of the ratio of these values. In the case of titanium, one should expect a higher peak pressure than experienced by that of aluminum which is more compliant to the process. Using the above equations to propagate the

pressure through time for an assumed Gaussian laser intensity profile, and then nondimensionalizing in terms of peak pressure and laser duration gives the following profile (Figure 8).

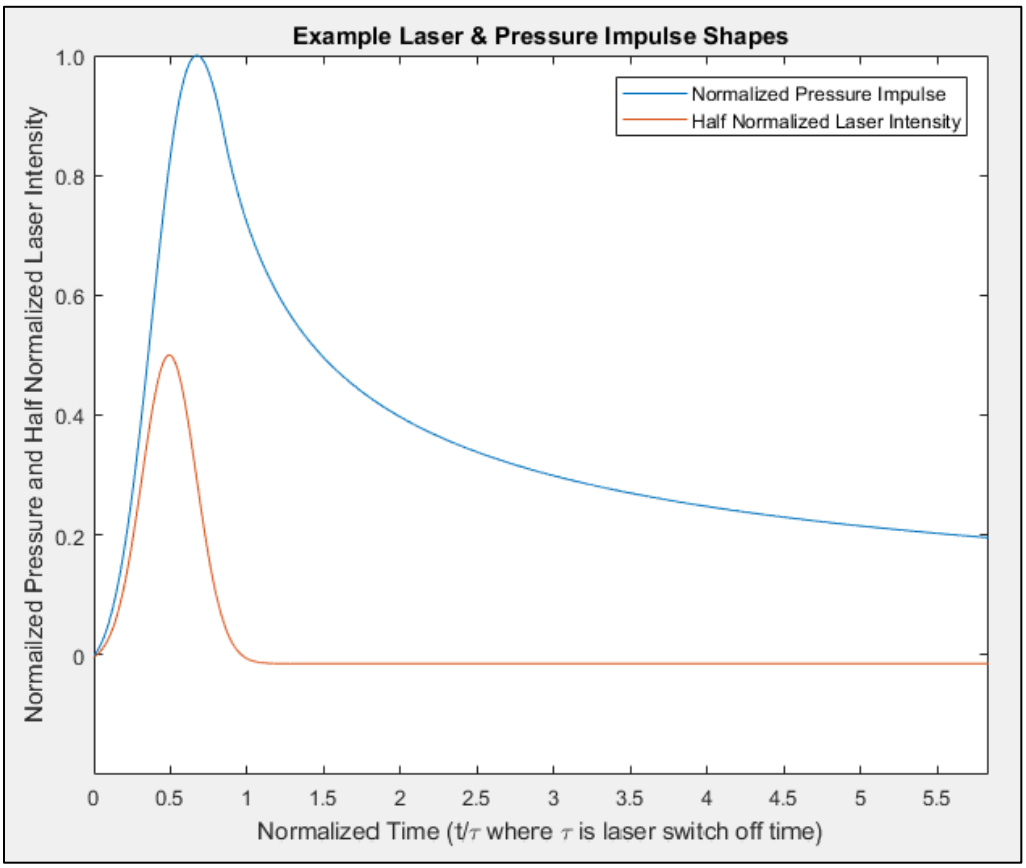

Figure 8: Nondimensionalized example pressure impulse profile in time from Gaussian laser profile

The Gaussian laser intensity here has been "half normalized" to separate it visually from the pressure profile and the timeline has been normalized to time, "τ" which is the time at which the laser is completely shut off. The pressure response to this laser intensity has been normalized to peak pressure. It can be seen that the peak pressure is reached shortly after peak laser intensity, and the FWHM peak width of the pressure profile is between 1.2 and 2 times the FWHM peak width of the laser intensity. The pressure dissipation

after the laser intensity reaches zero follows an adiabatic cooling profile which takes longer to allow the pressure to fully dissipate. This pressure impulse shape will serve as the basis for the pressure applied for the LSP event, allowing for modification of the FWHM peak width and adiabatic cooling rate of the impulse which will be discussed later.

Hooke-Jeeves Optimization Algorithm

The experimental approach taken in the current work attempted to determine a "best-fit" pressure impulse shape in both time and space by using optimization methods to modify the applied impulse shape until FEM results most closely matched empirically collected surface displacement and residual stress data. The fundamental principle of optimization is to find the minimum or maximum of some objective function which reflects the goals of the optimization by way of useful metrics.

In cases like this FEM-based optimization, a "direct (or pattern) search" algorithm such as the Hooke-Jeeves method is quite effective. This method determines a local slope in just one or two dimension by conducting "exploratory" perturbations away from a "base point". When a "downward" slope is found, the algorithm jumps in a "pattern" of increasingly large steps along this vector until the objective function makes no further improvements. This process is repeated from each subsequent base point, with decreasing perturbation step sizes, until the minimum is reached, as determined by no further improvement of the objective function, even with the smallest allowable perturbations in all directions. [93], [94]

In the current work, the goal was to reach the best possible match to collected empirical data. This data consists of multiple data points, across two measurements (surface displacement and residual stress), and so a standard metric is required to compare simulation results to experimental data. Further, it may be of interest to "more closely match" one of these measurements over another. Taking all of this into account, the objective function is defined as follows. [94]

$$Objective = \sum_{i=1}^{n} \frac{X_i * W_1}{S_1} + \sum_{j=1}^{m} \frac{X_j * W_2}{S_2}$$

In this equation, n points of metric 1 are summed with m points of metric 2 such that X_i denotes a single point computed metric for measurement 1, and X_j denotes a single point computed metric for measurement 2. Also W_1 & W_2 are the corresponding weights applied to levy differing importance on either metric as desired by the designer. Finally S_1 & S_2 are the corresponding scale factors to put the associated metrics into the same order of magnitude so that one does not overshadow the other purely in magnitude. In the simplest way, these scale factors can be set equal to the average of the target data (in this data matching case) such that the units match and therefore create a unitless objective function value. For data comparison, there are many metrics to choose from. For this work the square of the difference as well as the absolute value of the difference were considered. The squared difference is computed by simply squaring the pointwise difference for each measurement. The absolute value difference is computed by simply taking the absolute value of each pointwise difference. Both of these metrics result in positive values, ensuring that positive and negative differences do not cancel out to give

the appearance of a perfect match. The squared difference also results in an increased "penalization" of larger differences. The final explicit FE model for this work was an axisymmetric model which had a tendency to predict greatly reduced surface displacements for nodes very near the center of the laser spot. When the majority of modeling points are relatively accurate, but are offset by just a few points which are very inaccurate, the squared difference will drive the data toward a worse overall match to drive down the squared effects of the inaccurate points. For this reason, the absolute valued difference metric was chosen to insert into the objective function. [94]

In the best-case scenario, a metric could be linked, mathematically, to driving design parameters and the gradient of the objective function could be directly computed to assist in minimizing it. For this work, however, the inner workings of the FEM are not known to the optimization code, and the results are very non-linear. Thus a direct mathematical relationship is unknown; some might call this a "black box." The Hooke-Jeeves algorithm is well suited to handle this type of situation with its pattern-search process which determines the local slope by systematic perturbations.

Hole-drilling Residual Stress Measurement

Residual stresses are self-equilibrating elastic stresses which, in the case of LSP, are the result of localized permanent plastic deformation. As previously mentioned, the hole-drilling method of residual stress measurement was used for this work. This method involves incremental drilling of a small hole with fluted orbital bits to accurately remove layers of material which contain residual stress. The material relaxation is then measured

at the surface via strain rosette, closely surrounding the hole. The residual stresses can potentially differ in the x and y directions, as well as into the depth (see Figure 9). A strain rosette at the surface, surrounding the hole allows the determination of both x and y axial stresses as well as the x-y plane shear stress within each depth increment [79]. The residual stress must necessarily be averaged over the entire hole of diameter D, and can be incremented by depths as small as 0.025D measuring residual stress as deep as 0.5D [79]. This depth limitation is a result of diminished surface strain from relaxation as stressed material deeper into the hole is removed.

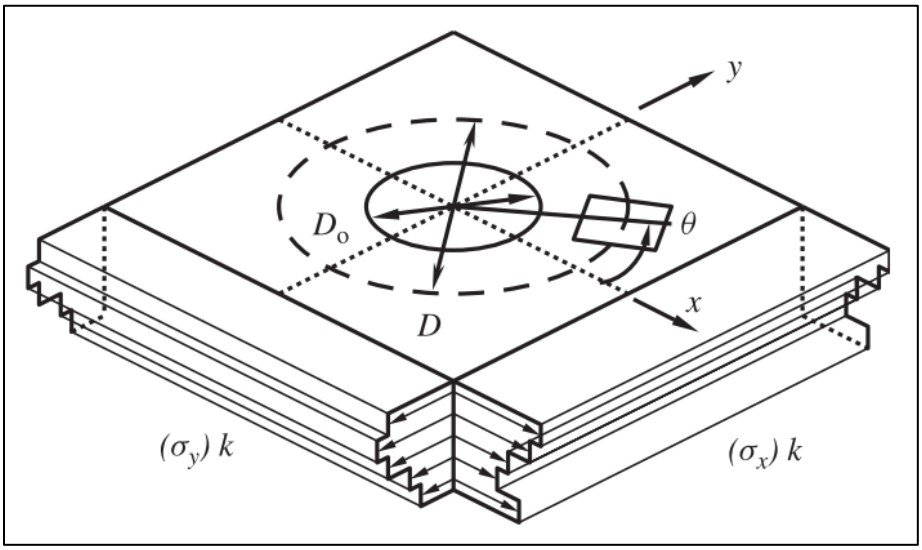

Figure 9: Visual representation of incremental stresses into depth [79]

Generally speaking, the measured strain, ε given by a gauge at angle θ to the designated x-direction as seen in Figure 9 can be represented by the following equation. [79]

$$\varepsilon = \frac{\sigma_x + \sigma_y}{2}\frac{(1+\nu)\bar{a}}{E} + \frac{\sigma_x - \sigma_y}{2}\frac{\bar{b}}{E}\cos 2\theta + \tau_{xy}\frac{\bar{b}}{E}\sin 2\theta$$

Here, σ_x, σ_y, and τ_{xy} are the in-plane x, y, and shear stresses in the removed volume, and ν and E are the Poisson's ratio and elastic modulus of the material accordingly. Also, $\bar{a}$

and $\bar{b}$ are calibration constants which are a function approximately proportional to the square of the diameter of the hole with respect to the diameter of the strain rosette. These calibration constants also change for hole-drilling increments deeper below the surface of the specimen as the strain response to the removal of this material is diminished by increased distance from the relieved stresses. An example (not representative of the current work) of strain rosette specific calibration constants can be seen in Figure 10. For a given hole diameter (D_0) relative to the strain rosette size (D), at a given depth (h), the calibration constants $\bar{a}$ and $\bar{b}$ can be readily found from the curves. These curves are, again, calibrated for a specific strain rosette, and another set of curves would be used for a different strain gauge configuration.

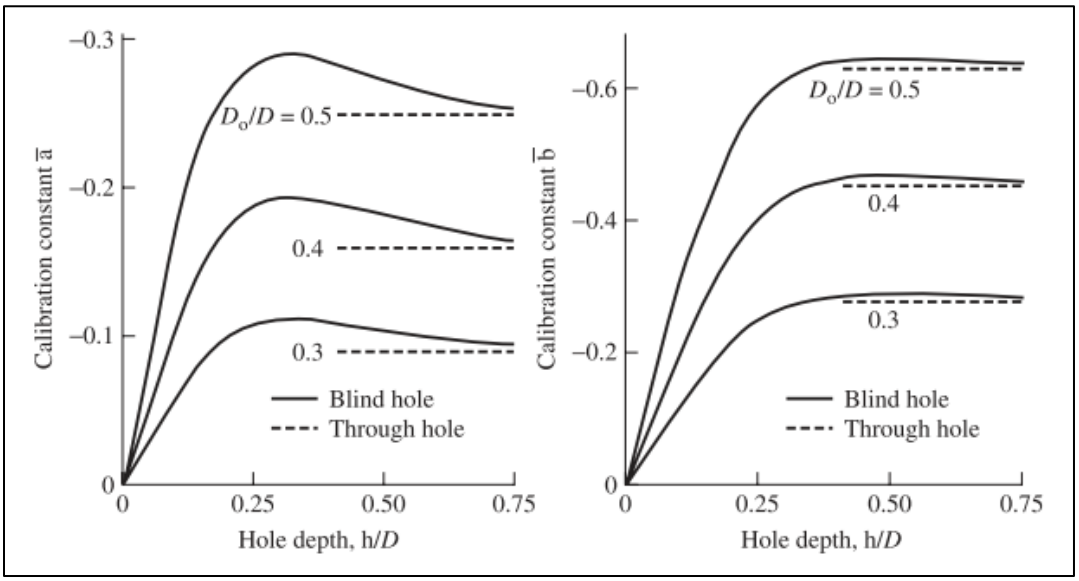

Figure 10: Strain rosette specific hole-drilling calibration constants [79]

Given a stain rosette consisting of three gauges surrounding the hole, the recording of three strain measurements gives enough information to solve for the three unknown stresses. The method described thus far is effective if the residual stress is uniform into

the depth; however, variation of stresses into the depth creates a continuous stress function with respect to the depth below the surface. Thus, the strain response to removal of this stress function must be characterized by an integral taking the following form. [79]

$$\boldsymbol{\varepsilon}(h) = \frac{1+\nu}{E}\int_0^h \widehat{\boldsymbol{ab}}(H,h)\,\boldsymbol{\sigma}(H)\,dH$$

Here, h is the drilled depth of the hole, $\boldsymbol{\varepsilon}(h)$ represents the measured strain combination for the given hole depth, $\boldsymbol{\sigma}(H)$ is the stress combination function with respect to depth variable, H, and $\widehat{\boldsymbol{ab}}(H,h)$ is the calibration constant function with respect to H for a given hole depth, h. Recall, however that the strain is measured with the desire to solve for the stresses which appear inside the integral. This inverse problem is thus a Volterra equation of the first kind for which $\widehat{\boldsymbol{ab}}(H,h)$, is in fact, the kernel function [79]. This is usually solved by expressing the residual stress function as a series expansion [95]. Continuous strain measurement throughout the hole-drilling process is ill advised due to potential heat effects as well as physically applied force from the drill bit, however, the strain can be measured incrementally. This creates a piecewise solution in which the components are represented as vectors and matrices with dimensions equal to the number of increments measured in the process, and can easily be inverted to solve for the in-plane stress components at incremental depths. [79]

One underlying requirement of this hole-drilling method is that the measured strain is purely elastic. This might seem a simple requirement to maintain, however in the right conditions, the removal of certain material might accentuate a stress

concentration which could result in plastic deformation. This would be readily apparent when the computed stress appears to exceed the yield stress of the material.

Uncertainty in the determination of residual stress via hole-drilling comes from two main sources. The first, as may be expected, is simply strain measurement error, a function of the gauge and measurement method, and easily propagated into the residual stress results. The other main source of error is the error in fit of the series expansion when solving the inverse problem. This error depends on the order of the series expansion, in other words how many terms are used, as well as the basis functions used for the expansion. This error is less easy to calculate, but has been determined recently via "Monte-Carlo-based" analysis of series expansions of increasing order. This work also showed that the uncertainty due to strain gauge resolution largely outweighed uncertainty due to the fit of a series expansion of just 2-3 terms as too many terms result in an ill-conditioned result. [95]

Surface Displacement Measurement

The surface displacement of each LSP "dimple" is yet another indicator of the effectiveness of the laser treatment. This displacement was measured using an axial chromatic confocal optical profilometer. This instrument uses optics with finely tuned chromatic aberrations to split the color spectrum into differing focal lengths. This creates a vertical measurement range of 400 micrometers over which the visible light wavelength spectrum is focused across the vertical range. When a surface is put into this measurement range, only the wavelength for a specific corresponding height will be in

focus, returned to a beam splitting mirror and pass through a pinhole filter to a spectrometer. This wavelength thus corresponds to a specific vertical position known with an accuracy of 40 nm, limited by the spectral resolution of the digital spectrometer. This measurement method requires no laser protection, is impervious to surrounding light and surface reflectivity, is capable of very fast scanning speeds, and allows for independent selection of lateral resolution and height accuracy. A diagram of the method can be seen in Figure 11. [96]

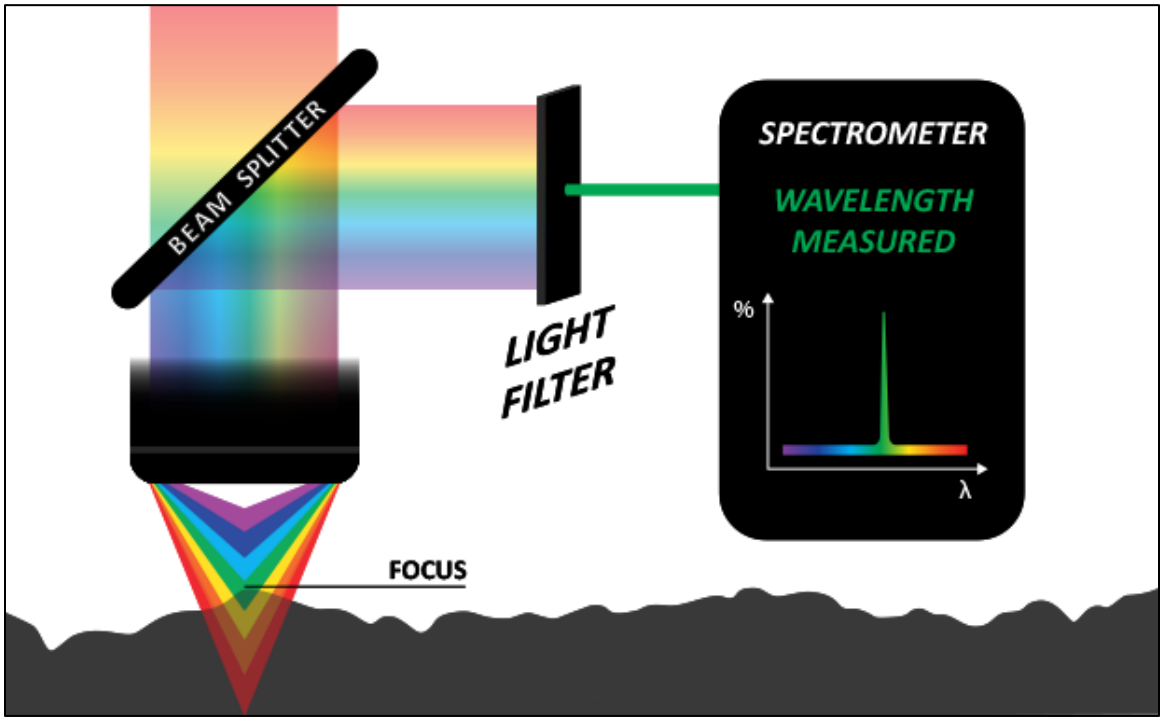

Figure 11: Diagram of chromatic confocal profilometry (adapted from [96]**)**

III. Modeling and Experimental Methods

Chapter Overview

Having established the theoretical foundations of the methods which were used, this chapter outlines the experimental methods used to collect empirical data, along with the details of the finite element model and optimization flow used to accomplish the desired data-matching for pressure impulse shape determination. This section will go into detail about FE modeling development, optimization methodology, and data collection, but discusses only how results influenced subsequent model development. Complete results will be in the following chapter, mirroring the order in which these methods are introduced. Details about the Abaqus FE code and Isight optimization code can be found in Appendix A. Abaqus Finite Element Code Details, and Appendix B. Isight Optimization Code Details, accordingly.

Research Flow

The overall flow of work can be seen in Figure 12. The flow is divided into experimental and computer portions on the top and bottom, respectively, as well as the pressure impulse determination and pressure impulse validation steps on the left and right. Blue boxes and arrows indicate modeling configuration or information flow, and green boxes and lines indicate experimental procedures and results or data flow. The experimental determination of Johnson-Cook material properties (bottom of Figure 12) is from an outside source [97] and was not an experimental portion of the current work, but drove the material model in Abaqus.

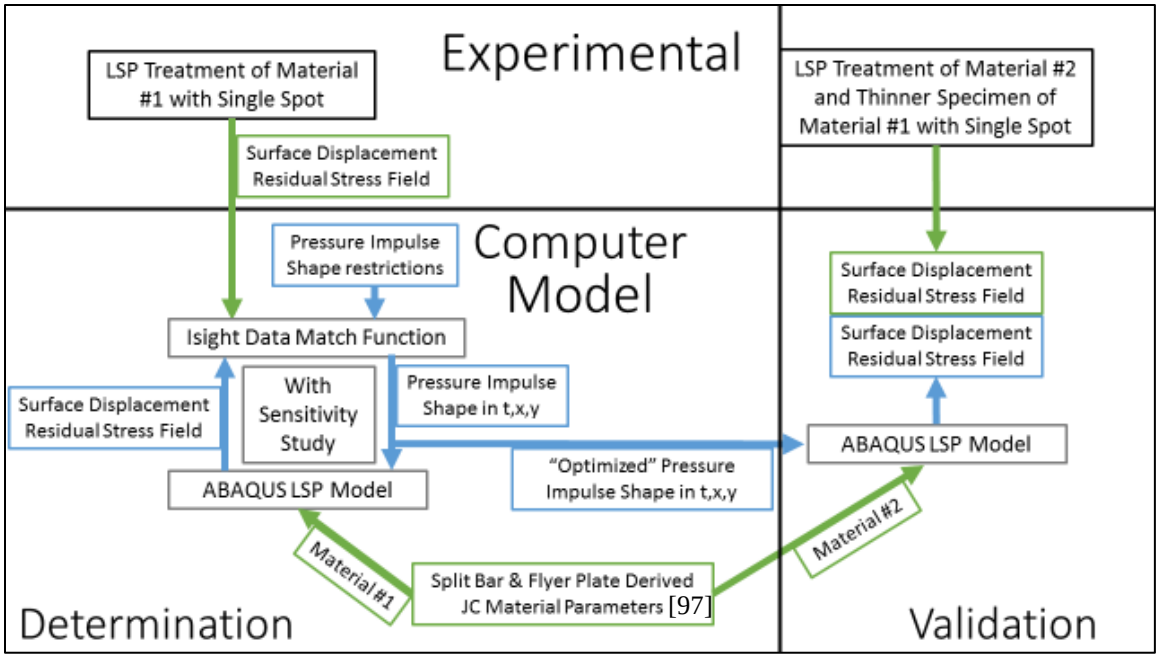

Figure 12: Modeling flow diagram (experimental data in green, modeling results in blue)

At the top of the diagram are the single spot LSP treatment experiments which fed residual stress and surface displacement data into the computer modeling portion of the research. The data was taken as an average over eight single LSP spots per material and thickness. Material 1 was 2024-T351 aluminum and material 2 was mill-annealed 6AL-4V titanium, both chosen for their small, uniform grain structure and well characterized material properties. The loop in the lower portion on the left shows the computer model which used optimization methods (within Isight code) and FEM (in Abaqus) to match data collected from the aluminum specimens to determine the "best-fit" pressure impulse shape in time and space. The best-fit pressure impulse shape was then applied to the titanium FE model (on the right side of the diagram) to validate the pressure impulse shape model against the data collected from the titanium samples. Also, a sensitivity study was conducted within the optimization process to determine how the optimization

algorithm responded to changes in algorithm input and configuration parameters as well as data and material properties uncertainty.

Modeling Work

The principal effort of this work used optimization and FEM codes to determine the pressure impulse shape in time and space that resulted in the best match to measured data from the aluminum specimens. The model development began with a 3D FE model built to match the work of Hfaiedh [51] in order to verify the basic FEM framework. This model was then modified to improve and verify the material model. Another FEM study was done to evaluate the response of four different model types, in terms of accuracy of output as well as computational expense. An initial optimization methodology was then developed to verify the process used to match a known pressure impulse shape. The FE model within the optimization methodology was then upgraded to match the experimental conditions including a wider, square laser spot, and 2024-T351 aluminum material properties. This final optimization configuration was used to match the aluminum empirical data and determine a best-fit pressure impulse shape in time and space. This best-fit pressure impulse was then transferred to a titanium FE model to validate the modeled shape of the impulse.

Initial Round Laser Spot 3D Model

An initial FE model was built in Abaqus and compared to published work of Hfaiedh et al. [51]. The purpose of this model was to verify the fundamental FEM techniques used to model LSP explicitly. Hfaiedh's work was chosen for the single spot

analysis and the inclusion of modeling details often lacking in work of this nature. This initial FE work was accepted and presented at the 2018 AIAA SciTech and SEM Annual conferences [98], [99].

The model was a full 3D, explicit integration model with a round laser spot and utilized a Johnson-Cook material model of 2050-T8 for comparison to published work (see material constants in Table 1) [51].

Table 1: Johnson-Cook material constants for 2050-T8 aluminum used in this model [51]

J-C Const.	A (MPa)	B (MPa)	C	n	m	$\dot{\varepsilon}_0$	T_m (K)
2050-T8	510	200	0.02	0.45	1	0.01	520

To avoid shock reflection, the untreated (side and bottom) faces of the model were bounded by infinite elements which allow stress waves to pass through them without reflection, essentially modeling an infinitely large specimen (See Figure 13). The bottom outside corners of the model were pinned in place by the infinite element to eliminate rigid body motion while also prevent boundary condition shock reflection. Elements of 0.05 mm were concentrated at the LSP spot center, and widened to 0.12 mm at the outer portions of the block.

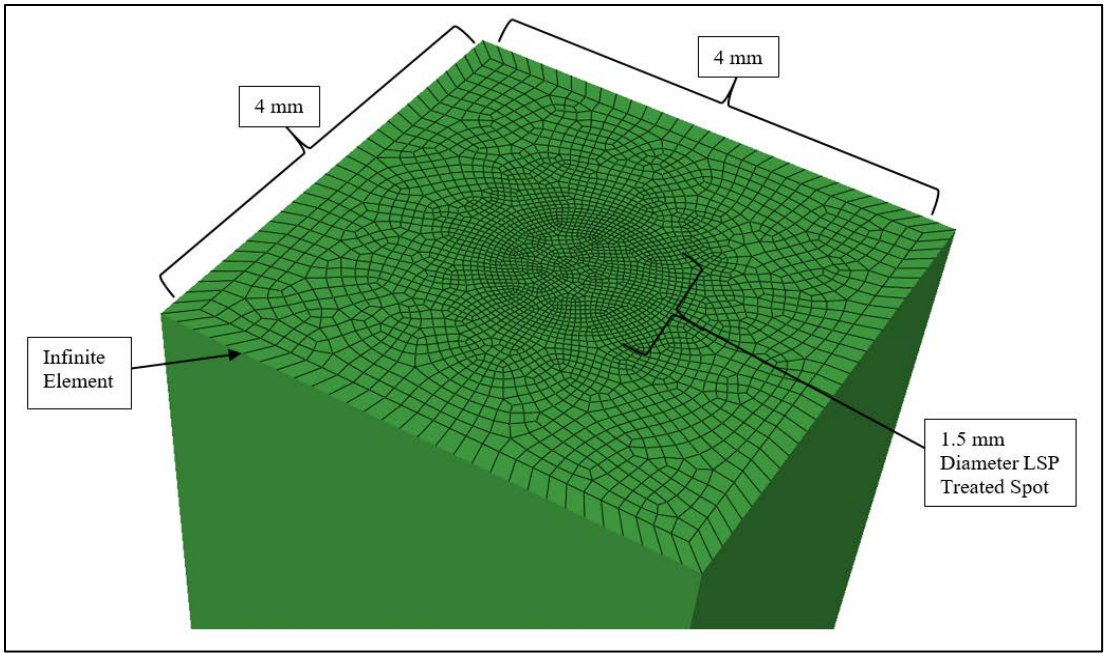

Figure 13: Round spot 3D finite element model [98]

The pressure impulse for this model was still assumed (simply for FE model development) to have an SRT profile in time. Spatially the pressure occupied a half power cosine shape as seen in Figure 14, chosen to match [51]. The SRT profile in time was directly traced from published work by Hfaiedh [51], again, chosen for its near-completeness of model description and results. Both the time and spatial profiles served as multipliers to a user input peak pressure which was varied from 1.1 to 1.8 GPa for initial modeling trials. The peak pressure was only achieved at the center of the laser spot, 10 ns after the initiation of the impulse, and the pressure reached zero at 210 ns after initiation.

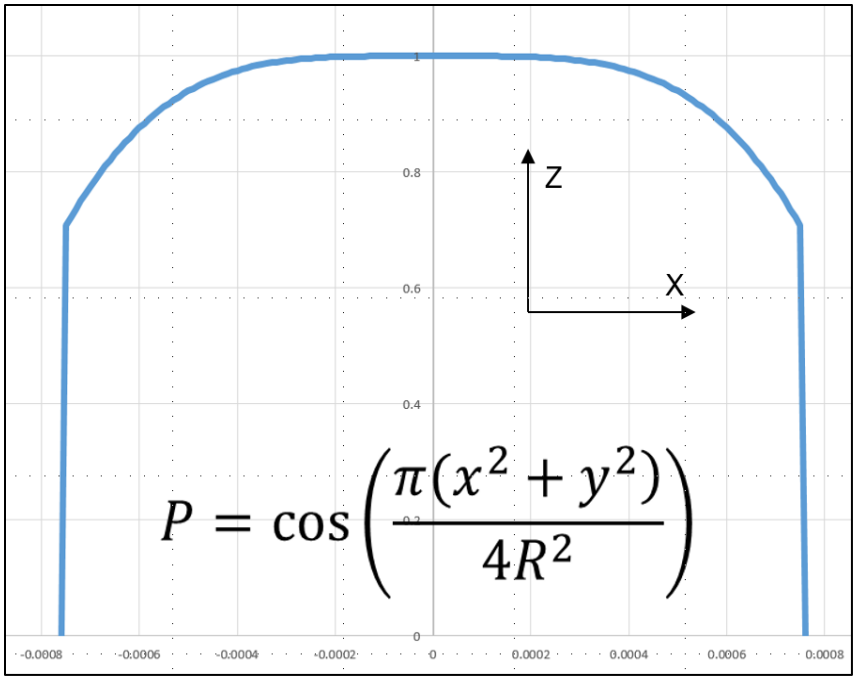

Figure 14: Cross-section of circular spatial pressure distribution across the 1.5 mm LSP spot

The very short time of the pressure peak required a very small time step in the simulation (1 ns) to ensure that the full effect of the pressure impulse was imparted onto the model and to keep the explicit simulation stable. Further, a great deal of kinetic energy is imparted into the model during the LSP event, and thus required a significant total run time (3.6 μs) to allow the stress wave to dissipate out of the volume. It was thought that this time would result in an equilibrium of residual stresses, but initial analysis of the model energy showed the need for longer run times to allow the kinetic energy to fully dissipate. The results from this model became very unreliable above 1.8 GPa, showing an increased tensile "spike" in the center of the treated spot at higher pressures. The trace of the compression wave through the material showed that high

compliance of the treated surface had caused a "backsplash" effect, accentuated in the center of the spot. This suggested an EOS should be used to allow for shock propagation.

While this model helped to construct the modeling framework, it could not be fully validated. Validation and verification of a single laser spot model against past work is quite difficult due to the lack of model detail and standard pressure profile shape in most work. It also presupposes that the pressure impulse shape is known, a fundamentally flawed assumption under investigation in this work. This initial model, however, demonstrated an acceptable low-pressure material response using the Johnson-Cook material model here, but highlighted the need to add an EOS to handle hydrostatic compression for higher peak pressures. The lessons learned from this initial model were incorporated into following refined models and demonstrated excellent improvement. Increased mesh and time-step resolution as well as a widened work piece resulted in smoother residual stress and surface displacement results.

Material Model Improvement and Verification

Based on the initial results, the Johnson-Cook viscoplasticity model was augmented with the Mie- Grüneisen EOS to handle hydrostatic shock propagation, and a study was done to trace the LSP event through time to verify the material model. The overall runtime was also extended to 8.2 μs to allow the model to dissipate the kinetic energy and reach equilibrium. The propagation of shock, stress, and strain through a single element located 0.3 mm below the LSP treated surface, was traced to show the development of residual stress due to plastic deformation resulting in retention of elastic strain. For an element slightly removed from the LSP treated surface, there will be a

slight delay until the shock reaches the element at which point the density will increase due to hydrostatic pressure on the element. This will also show itself in the single component in-plane stress and will be followed by a release of this shock loading. The shock will be followed by the slower elastic wave front, exhibiting a "knee" at the HEL elastic-plastic transition point. Finally, elastic fluctuations will accent a period of dynamic recovery during which material damping will dissipate elastic stresses until the kinetic energy approaches zero. The resultant permanent plastic deformation will leave behind a non-zero elastic strain which is directly related to the residual stress that remains. Figure 15, below shows two of these traces: on the left, the free surface velocity of two thicknesses of foil under laser impulse [100] and on the right, the dynamic stress response from a laser impulse [101]. The free surface velocity of the thinner example (in red) will very closely resemble the elastic strain just below the surface, including the aforementioned HEL "knee" above which the material responds at a different elastic-plastic strain rate. The free surface velocity of the thicker example (in green) would represent the elastic strain response much deeper below the LSP surface. The dynamic stress response on the right of Figure 15 shows the dramatic compressive spike which is the result of the intense shock, followed by the tensile rebounding and subsequent recovery of the stress state toward a net-compressive equilibrium after the event. These figures were used to qualitatively verify the material response to the LSP event.

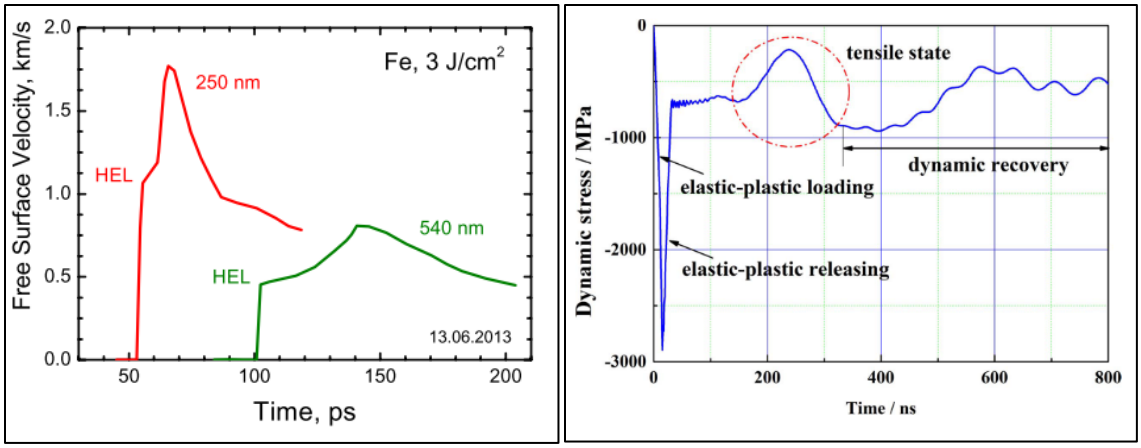

Figure 15: Example traces of: (Left) free surface velocity of a thin plate under laser pulse [100] **and (Right) dynamic stress response under laser impulse** [101]

A work and energy analysis was also accomplished for the entire model to show the distribution of energy through the LSP event. The large pressure impulse imparts a great deal of work into the system over a short amount of time. This work is transferred to the material in the form of kinetic and potential energy. The kinetic energy is eventually dissipated through plastic deformation and viscous (material) damping. The remaining energy trapped in the system is potential energy stored in the form of elastic residual stress. This was shown well in the comprehensive book put forth by Ding & Ye [1] from which Figure 16 was taken. In this figure, W_t is the total work applied to the FE model, all of which occurs within the first few ~200 ns (over the duration of the pressure impulse). W_i is the internal energy in the system, this includes elastic strain energy (not shown) as well as kinetic energy, W_k. The kinetic energy exhibits an initial spike from the hard shock of the material which imparts permanent plastic strain. W_v is the total energy absorbed by viscous (material) damping. The large changes which occur in Figure 16 at around 1000 ns are due to the shock front exiting the workpiece. The kinetic

energy is gradually dissipated out of the FE model by this damping work, and when it has diminished, the remaining internal energy is elastic strain energy. This is proportional to the residual stress stored in the model at the end of the event. This figure was also used to qualitatively verify the material response of the FE model.

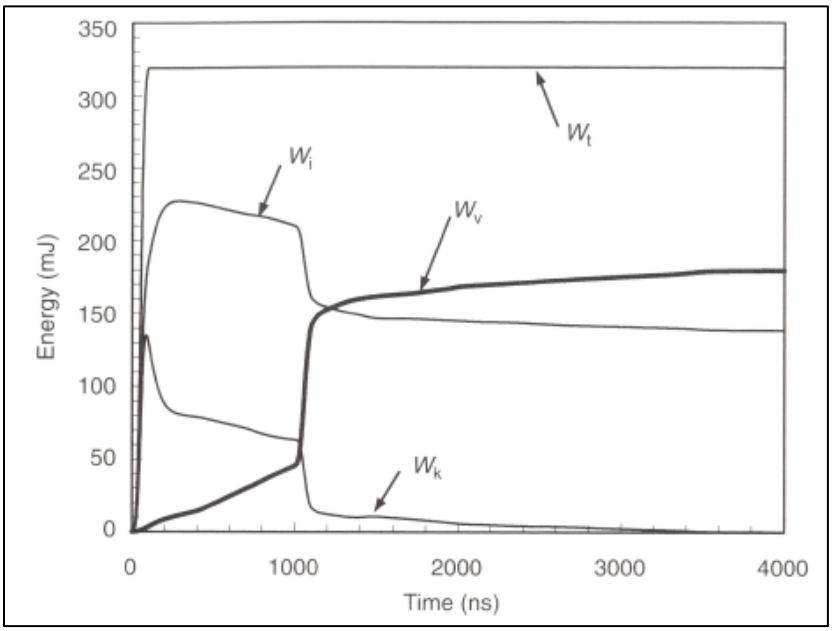

Figure 16: Work and energy trace for a whole model LSP event [1]

Finite Element Model Type Comparison

For the next iteration of FEM, a comparison study was conducted to determine the likeness of results from various forms of the same model. A comparison was made between a full 3D model, a quarter-symmetric 3D model, a 2D axisymmetric model, and a modified 2D axisymmetric model. The models were sized up to the 4.7 mm LSP spot which would be used for the data-matching. All of the models matched in overall dimension, mesh size, infinite elements, applied pressure profile, and material properties. The mesh size was determined from a convergence study conducted on the axisymmetric

model for efficiency, and that mesh density was used in all subsequent models. In this case a uniform pressure profile and generic SRT impulse shape were assumed. The Johnson-Cook viscoplasticity model and Mie-Grüneisen EOS were again used, this time for the 2024-T351 material which would be used for the remainder of the experiment. Though the results of the quarter-symmetric 3D model most closely matched the full 3D model, the 2D axisymmetric model gave a reasonable results, particularly considering the greatly reduced computation time it afforded. The axisymmetric model of the same spot width under-predicted the compressive residual stress nearer to the treated surface. To attempt to alleviate this difference, two modified axisymmetric models were tested. In one modified model, the peak pressure for the 4.7 mm wide spot was increased to match the total force imparted by the full 3D model pressure impulse. In the second modified model, the width of the axisymmetric spot was increased to match the area (and thus total force) of the 3D model. The original 4.7 mm wide axisymmetric model with equal peak pressure most closely matched the full 3D model. In the axisymmetric model, residual stress results deeper below the surface matched perfectly, and were slightly more tensile near the surface. For efficiency in the integrated optimization model, this axisymmetric model was used with a linear correction factor applied to account for residual stress differences near the treated surface. This correction method applied a different linear equation to each residual stress depth location. The linear equations were a regression of three points corresponding to peak pressures of 3, 4, and 5 GPa applied to the models for comparison. This correction method would serve as a “filter” through which axisymmetric residual stress results would be modified to better predict full 3D residual

stress results and reality. The optimization-based pressure impulse matching was attempted both with and without the correction method applied in order to determine its utility.

Optimization Model Proof of Concept

Next it was necessary to integrate the FEM into the optimization code to run a proof of concept data-matching tool and test the capabilities of that tool. This was done by matching an ideal target "data" created by the FE model. Isight optimization code is designed to exchange variables with various other codes and programs, including Abaqus, Excel, or MATLAB. The software is designed to transfer numerical parameters between any number of software and codes and employ one of many available optimization algorithms to minimize or maximize a given objective function. Isight has numerous optimization algorithms which can be utilized; this work used the Hooke-Jeeves pattern search algorithm. This algorithm first uses an "exploratory" step in the vicinity of the initial input variables to find a direction which results in improvement of the objective function. Then increasingly large "pattern" steps are made in this direction until improvement stops. This cycle is repeated until the exploratory step yields no direction for improvement. This method tends to work well for "black box" systems, as no differentiation of an objective function is required to determine the local gradients, rather a local slope is found by perturbation. [94]

The FE model for this part was a 2D axisymmetric, 4 mm diameter, 4 mm deep cylinder, with a 1.5 mm diameter round laser treatment zone at the top surface. A convergence study was conducted, and a fine mesh of 0.01 mm square 4-node elements

was more than adequate to handle the high pressure gradients imparted by the impulse. This resulted in 80,000 solid elements, skirted by 600 infinite elements in axisymmetry as seen in Figure 17. [43] Again Johnson-Cook and Mie-Grüneisen material properties were used to handle the hard shock as well as the viscoplastic behavior at large and varying strain rates (Table 2).

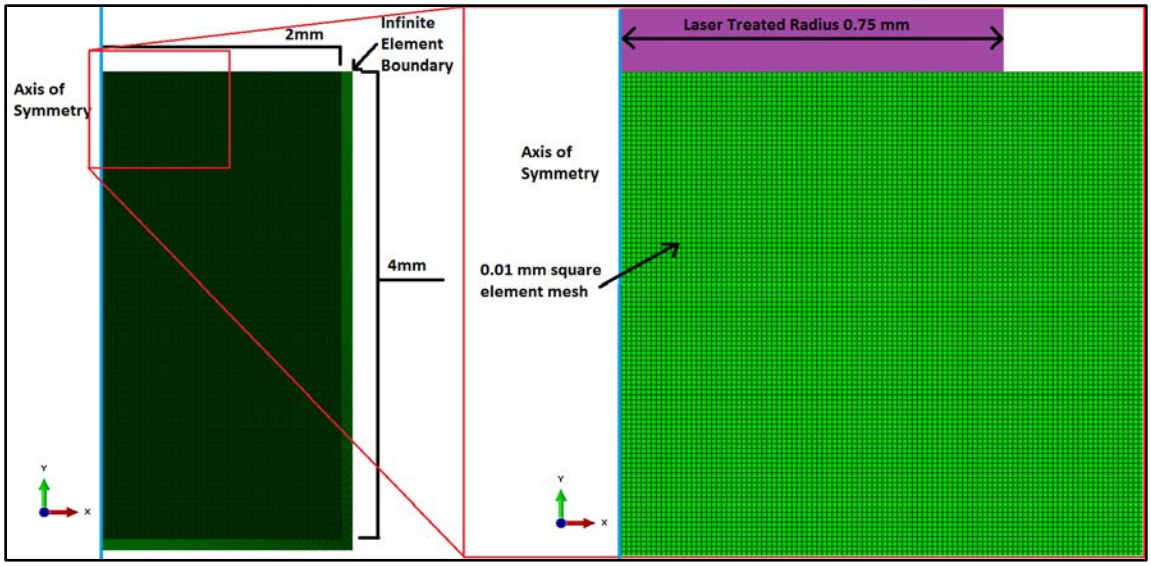

Figure 17: Abaqus FE model showing mesh, laser treated zone, and infinite element boundary [102]

Table 2: 2050-T8 Johnson-Cook and EOS material properties [51]

	Johnson-Cook Material Properties							**EOS Properties**	
Property	A (MPa)	B (MPa)	C	n	m	$\dot{\varepsilon}_0$ (1/s)	T_m (K)	s	c_0 (m/s)
Value	510	200	0.02	0.45	1.0	0.01	520	1.339	5386

The shape of the pressure impulse in both time and space was the object of manipulation by the optimization algorithm, and thus needed to be defined by a reasonable number of parameters to keep the dimensionality of the optimization space low. To accomplish this, the pressure impulse was limited to five defining parameters.

One parameter was used simply to define the maximum peak pressure of the event in GPa. One parameter was used to define the curvature of the spherical spatial pressure profile which acted as a multiplier allowing peak pressure at the center of the laser treated spot, and a reduced pressure at the outer edge of the laser spot (see Figure 18). [43]

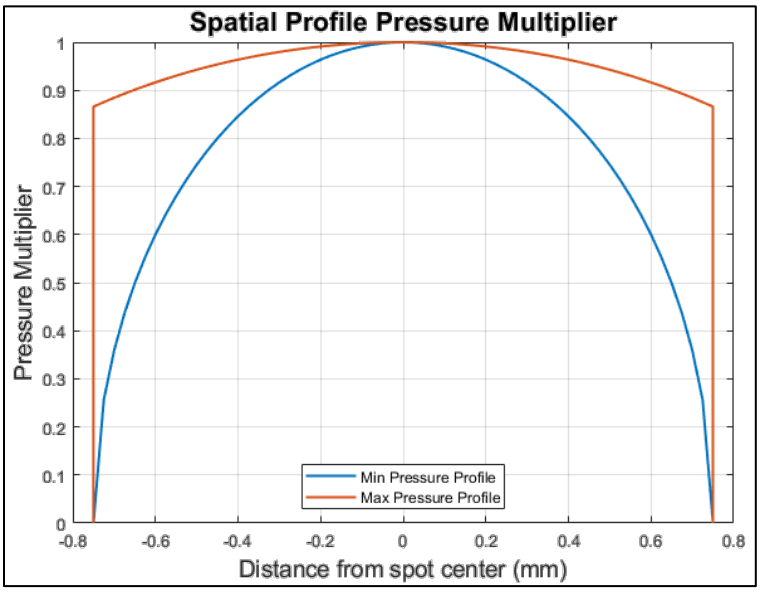

Figure 18: Spatial profile pressure multiplier upper and lower bounds [43]

The remaining three pressure parameters defined the profile of the pressure impulse in time by modifying three attributes of a generic SRT profile shape in tabular form (see Figure 19). One parameter defined the overall duration of the pressure impulse in nanoseconds. Another, scaled the FWHM of the peak width by an arbitrary multiplier (see Figure 19). The final parameter scaled the pressure dissipation rate after the peak pressure was reached, a kind of "pressure half-life" by way of another arbitrary multiplier (see Figure 19). With these pressure parameters, the chosen maximum peak pressure would only occur at the very center of the laser treated spot, as defined by the spatial profile multiplier, and at one specific instant in time, as defined by the time profile

multiplier. All other locations and times throughout the event had a reduced pressure as scaled by the combined multipliers. [43]

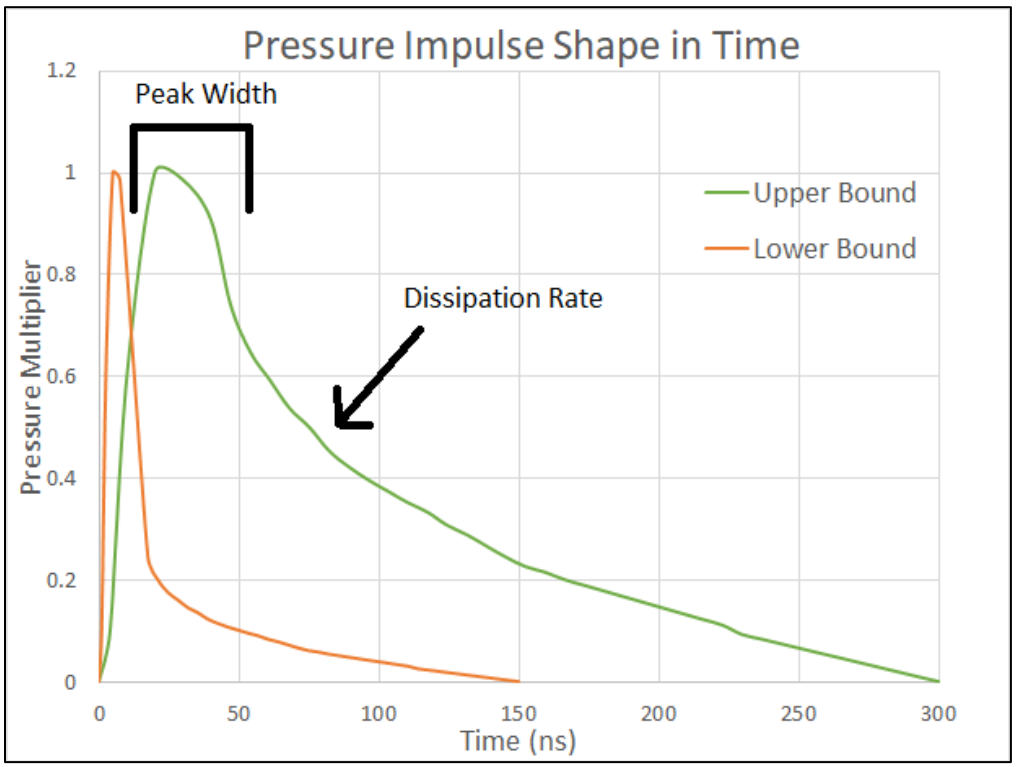

Figure 19: Time profile pressure multiplier upper and lower bounds [43]

Isight was put to use running the Hooke-Jeeves optimization algorithm. The input variables for the optimization flow were the five pressure impulse parameters, restricted in range and step-size (see Table 3) to a scope adequate for a proof of concept. The five-variable optimization space was composed of over 1.1 Million unique pressure impulse shapes which could be generated. For each iteration of selected input variables, the chosen parameters were processed by MATLAB and Excel to match the model mesh size and time step configuration and output tabular and text pressure values which were inserted into the Abaqus input file. The FE simulation was executed via python script

(Appendix F. Abaqus Execution Python Code). [43] The broad application of Isight is outlined here. For more details about how the code is setup refer to Appendix B. Isight Optimization Code Details.

Table 3: Optimization proof of concept input variables, range and increment [43]

Pressure Impulse Input Parameter	**Minimum Value**	**Maximum Value**	**Increment Size**
Peak Pressure (GPa)	2.0	7.0	0.25
Spatial Profile Curvature (see Figure 18)	1.0	4.0	0.25
Impulse Duration (ns)	150	300	10
Peak Width Scale Factor (see Figure 19)	0.5	2.0	0.1
Dissipation Rate Scale Factor (see Figure 19)	0.5	2.0	0.1

The selected pressure impulse, once run through the FE model, resulted in 75 vertical displacement values corresponding to the nodes extending across the top treated surface of the model, and 10 averaged residual stress values from the groups of elements representing simulated hole-drilling discs extending from the surface incrementally into the depth at the center of the laser spot. These values were related point by point to the FEM generated target values (see Figure 20), and the absolute values of the differences were inserted in to the optimization objective function below where X_i is a single point absolute residual stress difference and X_j is a single point absolute surface displacement difference . [43]

$$Objective = \sum_{i=1}^{10} \frac{X_i * W_1}{S_1} + \sum_{j=1}^{75} \frac{X_j * W_2}{S_2}$$

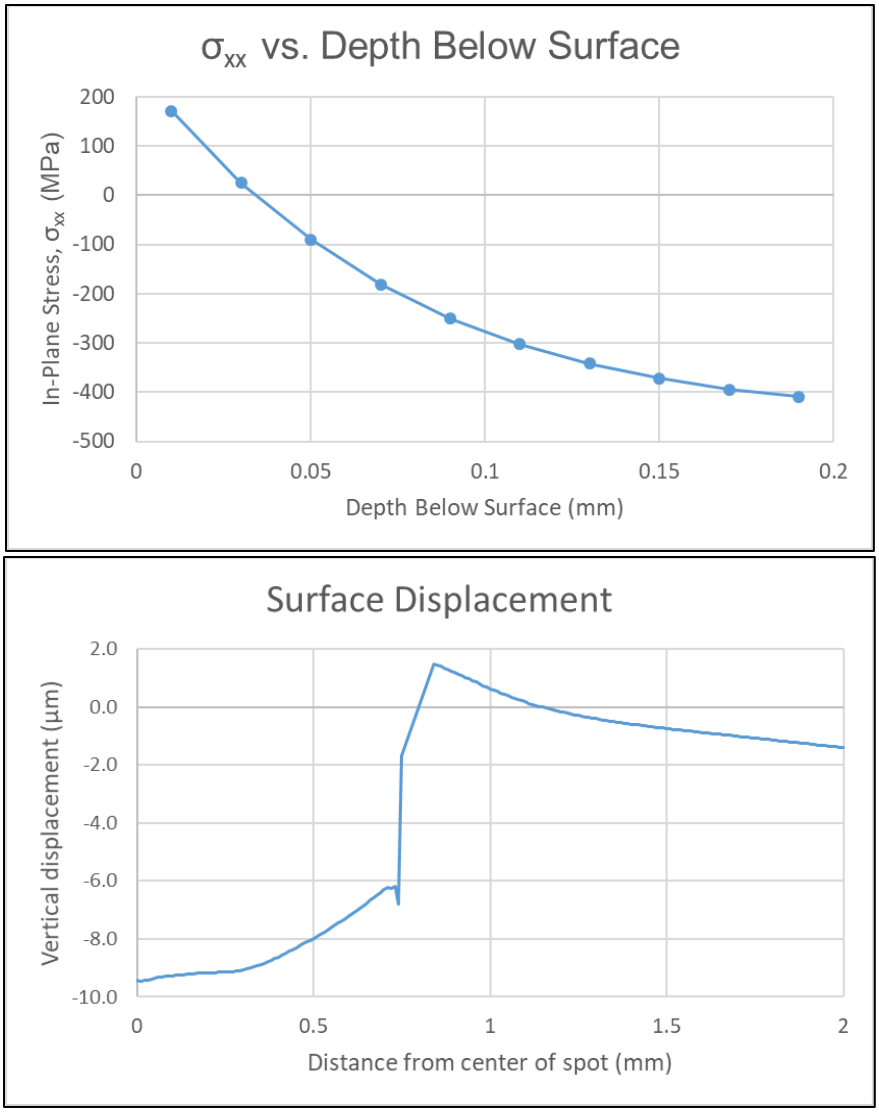

Figure 20: FEM generated residual stress (top) and surface displacement (bottom) profiles set as the target for optimization model [43]

The Isight optimization model flowed in the following way. First, the five pressure parameters were chosen and passed to Excel and MATLAB components to create the pressure profile and impulse shapes then convert to tabular and text inputs designed to fit into the FE model. The FEM was then run from a python script with these pressure inputs, and the residual stress and surface displacement results were extracted to

Excel where residual stress averages were computed to replicate the incremental hole-drilling measurements into the depth. The absolute differences between these FEM results and the target values were then calculated and summed into the objective function. The objective function result was then passed back to the Hooke-Jeeves algorithm, and new pressure impulse parameters were selected based on these results. The process was iterated for various pressure impulse shapes and as many times as dictated by the pattern search method (up to 1000 maximum) until the objective function was minimized, indicating the closest possible match to the target residual stress and displacement profiles. A diagram of this optimization loop can be seen in Figure 21. [43]

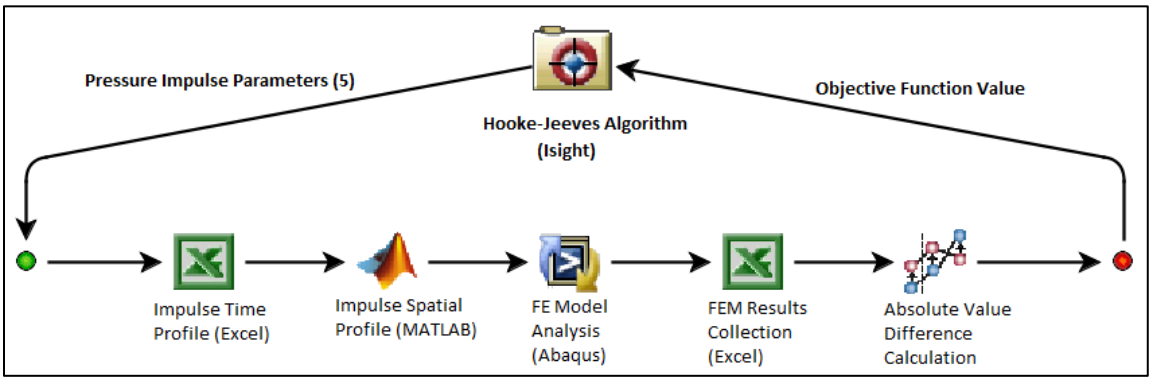

Figure 21: The optimization model flow in Isight code with MATLAB, Excel, and Abaqus [43]

User inputs to the optimization algorithm discussed thus far include the objective function weight factors and the input variable limits, increments, and starting points (initial pressure impulse parameters). The algorithm itself also has performance variables which must be chosen by the user. The first of these is the maximum number of allowable iterations. It is important that this value is set high enough to allow the algorithm to reach an optimization point, but not so high that extra computation time is

wasted continuing to seek an objective minimum after the best solution has already been discovered [94]. [43]

Another algorithm performance variable is the Hooke-Jeeves initial step size, limited to between zero and one. Simply put, this value dictates the initial pattern step size relative to the magnitude of the variable. Larger values mean that the pattern searching will more quickly traverse the optimization space, and thus will converge to a solution faster. However, this also means that the final solution may be less accurate. [43], [93], [94]

The final performance variable is the Hooke-Jeeves step size reduction factor, again limited to between zero and one. This value defines the size of the subsequent exploratory step after a pattern search has completed, again relative to the magnitude of the variable. Larger values mean that after a pattern search has improved the objective function, the following exploratory step will be closer to the same size and will result in a faster convergence toward a solution, but a reduced accuracy. [43], [93], [94]

A sensitivity study was conducted to determine the best algorithm settings for fast optimization as well as any tendencies of the optimization code to produce significantly different results based on user input including initial starting point and objective function weight values. Eight pairs of algorithm settings (initial step size and step reduction factor) were tested to observe the effects on the resultant objective function value and number of iterations to reach a minimized objective function value. While the specific objective function value by itself carried little meaning, the comparison of this value between algorithm settings is indicative of the quality of convergence.

With the algorithm settings more finely tuned, an investigation of objective function weight factors (W_1 and W_2) was conducted to determine their effects on the quality of match for both surface displacement and residual stress. There is no restriction on the values which can be used for the weight factors and it should be noted that if both weight factors were to be doubled, the objective function "surface" would simply be doubled in value, but remain unchanged in overall "shape" and the algorithm would converge toward the same best-fit pressure impulse shape. It is most useful then, to simply consider the ratio of weight factors (W_1/W_2), denoting how much the objective function favors one metric over the other (assuming non-zero weight factors).

When the most efficient algorithm settings were determined, the input parameter step increments were removed and the optimization code was allowed to work over a continuous 5 dimensional optimization space. This required over ten times as many iterations and in excess of 640 CPU-hours to conduct. The results, however, demonstrated the effectiveness of the optimization tool for matching an ideal pressure impulse shape and gave confidence to attempt to match experimental data. [43]

Fully Incorporated Optimization - FE Model

The final modeling effort in the current work was the development of the fully incorporated optimization & FE modeling scheme which was used to find the best-fit pressure impulse shape to match the empirical data collected in the aluminum specimens. This model utilized the same fundamental flow as the proof of concept optimization trial, but with an FE model built to match the experimental features, and with pressure impulse limitations more soundly rooted in the real-world physical mechanism by which they are

produced. The flow of the optimization proceeded as follows. First, Isight submits the user selected starting point pressure impulse parameters. These are run through a MATLAB code which produces the corresponding pressure impulse shape in time and space, in a form which is applied to the FE model input file. That input file is then executed in Abaqus using a python script for the predetermined settings, and the residual stress and surface displacement results are extracted. Those extracted results are run through an Excel spreadsheet which processes the results to align with experimental data comparison, namely simulated hole-drilling increments. A data-matching operation then compares the simulation results to the user uploaded target experimental data by computing the pointwise absolute value difference which is then passed on to be summed in the objective function. Isight then begins the Hooke-Jeeves pattern search algorithm by perturbing one or two input parameters and running the entire simulation loop again to determine the response of the objective function, and proceeds to iterate this process until the objective function reaches a minimum value. For this optimization, the previously determined best algorithm settings were again used.

As previously mentioned, the axisymmetric model provided similar results compared to the full 3D model and the 3D quarter-symmetric model. The difference in computational time between these two models, however, was substantial (two orders of magnitude). Further, the expansion of the optimization space to allow pressure variation across the 3D laser spot would dramatically increase the number of iterations required to converge to the best-fit pressure impulse shape. For model efficiency, therefore, the axisymmetric approximation was used under two cases, one with, and one without a

linear correction factor to account for the model differences. This model was a 4.7 mm wide LSP spot and again utilized Johnson-Cook viscoelasticity and Mie-Grüneisen EOS for material modeling but now for 2024-T351 aluminum as was used for experimental data (see Table 4). The element size, explicit time step, duration, and infinite element boundary all reflected the best practices determined in previous iterations.

Table 4: Aluminum 2024-T351 Johnson-Cook and Mie-Grüneisen material properties

	Johnson-Cook Material Properties							**EOS Properties**	
Property	A (MPa)	B (MPa)	C	n	m	$\dot{\varepsilon}_0$ (1/s)	T_m (K)	s	c_0 (m/s)
AL 2024-T351	369	684	0.0083	0.73	1.7	1	501.7	1.338	5328

The idealized proof of concept optimization model was a computer simulation trying to match a target produced by the same computer simulation. This allowed simplifying assumptions such as a spherical pressure profile shape which does not necessarily represent what might actually occur during the LSP event. If, for example, the profile is more Gaussian in shape, a model restricted to a spherical profile would have limited success matching the experimental data. Therefore, it was necessary to build an optimization space which allowed greater freedoms in choosing pressure profile shapes, but was not excessively large so as to drive up the number of iterations to converge to a data match. To do this, Isight was given parameter ranges which were rooted in physical constraints wherever possible. For example, the peak pressure range was based on laser intensity and guided by the work of Fabbro et al. (see Figure 22). The work showed the peak pressures obtained for various laser intensities and various impulse times in both open air as well as confined behind a flowing water layer (as in this work).

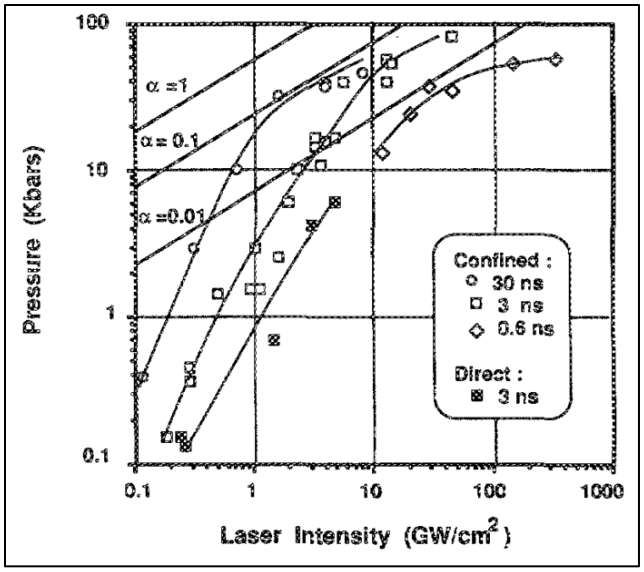

Figure 22: Relationship of impulse peak pressure with respect to laser intensity, impulse time and confinement condition [92]

In Figure 22, for confined conditions and a laser intensity of 4 GW/cm^2, the expected peak pressure will be between 10 and 60 Kbars (between 1 and 6 GPa) [92]. These values were set as the lower and upper bounds of the peak pressure variable within Isight.

Fabbro et al. [92] also outlined a one dimensional development of the pressure impulse shape in time as shown in the theory chapter before. It was found that for a range of assumed laser impulse profiles from triangular spike to Gaussian, to square plateau, the normalized pressure impulse profile varied only in FWHM peak width. The only other variable which changed the pressure profile in time was the adiabatic cooling, based physically on the specific heat ratio of the confined plasma bubble. This one dimensional simplification, however does not account for lateral escape of the pressure, and as a result, would never return to zero pressure. To alleviate this difficulty, the adiabatic dissipation term was modified by a reduction factor to ensure zero pressure

would be reached in reasonable time without dramatically reducing the work exerted on the metal. Thus, the "adiabatic cooling dissipation rate" modified by the optimization algorithm physically represents the combination of adiabatic cooling as well as lateral dissipation of the pressure impulse. Therefore, the number of input parameters for the time profile were reduced to two, while being rooted in the physical behavior of the pressure impulse formation.

The same physical bounding could not easily be applied to the spatial pressure profile as no work in this area was found to be available. The restrictions for the spatial profile then were as follows. The spatial pressure profile multiplier must necessarily be one at the maximum point, wherever that might be. The pressure multiplier must also reach zero at or near the outer edge of the LSP spot. Finally, the changes in slope along the profile curvature should not be too abrupt, as this would not accurately reflect the way in which pressure gradients behave naturally, in other words, it should have a continuous first derivative. With these constraints in mind, the spatial profile was broken into five points across the radius of the LSP spot for which Isight modified the pressure multiplier over a given range of 0.2 to 1.0. A MATLAB code then connected these points by means of a piecewise cubic Hermite interpolating polynomial. This is a piecewise polynomial interpolation which retains first derivative continuity (including at the axis of symmetry), but sacrifices second derivative continuity to reduce "overshoot" and help better retain the overall shape of points being connected. An example of this cubic Hermite interpolating polynomial fit can be seen in Figure 23 where the Isight chosen points are

labeled P1 through P5, and the polynomial fitting these points plus the constrained zero boundary is shown in red.

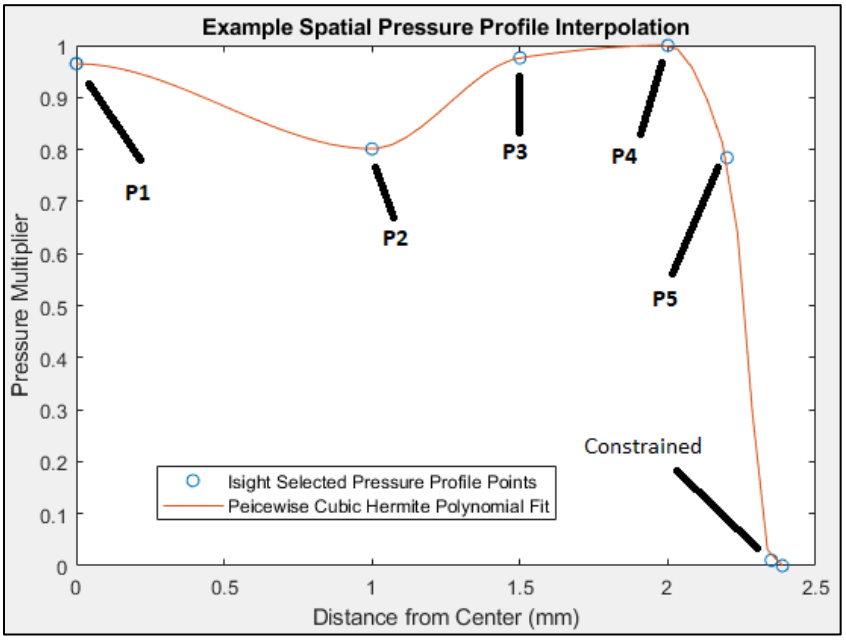

Figure 23: Spatial pressure profile formation by cubic fit of 5 pressure points

Thus, there were eight pressure profile parameters which Isight controlled, creating an eight-dimensional optimization space, and the allowable ranges of these parameters were governed as much as possible by real-world understanding and physical constraints (see Table 5). Isight applied this pressure impulse to the FEM input file, and the FE model python script was run (see Appendix F. Abaqus Execution Python Code).

Table 5: Isight controlled pressure impulse shape parameters and associated ranges

Pressure Impulse Input Parameter	Minimum Value	Maximum Value
Peak Pressure (GPa)	1.0	6.0
FWHM Peak Width (ns)	12	32
Adiabatic Cooling & Lateral Dissipation Rate	.91	.995
Spatial Pressure Point P1	0.2	1.0
Spatial Pressure Point P2	0.2	1.0
Spatial Pressure Point P3	0.2	1.0
Spatial Pressure Point P4	0.2	1.0
Spatial Pressure Point P5	0.2	1.0

The results of the FE model were exported in a way which allowed a direct comparison to the empirical data collected in phase one. Residual stress was averaged over 40 elements contained within the radius and depth equal to those of a single hole-drilling increment from collected data. This was done for 20 increments into the depth to directly compare to the 20 residual stress data points collected in the aluminum specimen. The surface displacement results of all nodes across the top of the FE model were extracted to compare to surface displacement data collected by the optical profilometer. In this case, the optical profilometry data had a much higher lateral resolution than the FE model mesh density, therefore, matching of an unequal number of points was needed. This could be done by interpolation of either the model points to collected data, or collected data to the model points. The latter was chosen to reduce the number of metric entries summed into the objective function which might bias the results. The pointwise absolute value differences to the experimental data were summed in the objective function which was the same as was used in the proof of concept optimization trial.

When the objective function was minimized, the associated pressure impulse shape was deemed to be the best-fit for the collected data and was ready for validation.

Validation of Best-Fit Impulse on Titanium Material Model

With a best-fit pressure impulse determined, these parameters were applied to the titanium FE model for validation. Recall that in the theoretical development of the pressure impulse shape in time, Fabbro [92] showed that the pressure is dependent on the "shock impedance" of the material on which the laser impulse is being applied. As such, when a best-fit pressure impulse is transferred to a different material, the peak pressure must be scaled accordingly, in this case scaled up from the more compliant aluminum, to the higher shock impedance of titanium. This scaling was done by taking into account the ratio of shock impedance by the following equation.

$$Scale\ Multiplier = \sqrt{\frac{\rho_{ti} C_{ti}}{\rho_{al} C_{al}}}$$

Here the densities ρ and sound speeds C for both aluminum and titanium are considered together as the "shock impedance" and the root of the ratio of these is taken as the multiplier for scaling up the peak pressure for the impulse. All other parameters were left the same, and the scaled pressure impulse shape was run through the identical model, but this time with titanium material properties applied as seen in Table 6.

Table 6: Mill-Annealed titanium Johnson-Cook and Mie-Grüneisen material properties

	Johnson-Cook Material Properties							EOS Properties	
Property	A (MPa)	B (MPa)	C	n	m	$\dot{\varepsilon}_0$ (1/s)	T_m (K)	s	c_0 (m/s)
TI 6AL-4V	1098	1092	0.014	0.93	1.1	1	1630	1.028	5130

Experimental Data Collection

The next phase of the current work was to collect the empirical data which served as the target for the optimization code, and the validation of the pressure impulse results. Two alloys were used for these samples; 2024-T351 aluminum and mill annealed Ti-6Al-4V titanium. Specimens were treated with single LSP impulses and the surface displacement (surface displacement), and residual stress into the depth were measured and averaged over a number of LSP spots. The typical standard deviation of random uncertainty for residual stress measurement is 10-15 MPa, and the commonly accepted tolerance of FEM accuracy is 20-35 MPa [86]. Using the upper and lower extremes of these values as the statistical standard deviation and acceptable margin of error accordingly, and seeking 99% confidence, the desired number of samples round up to 4 for a statistically significant study [103]. As the focus of this work was to match empirical data with simulation, as opposed to just demonstrate correlation, 8 samples per material/thickness were used to increase significance.

The material used for data-matching was 2024-T351 aluminum, which has well-characterized material properties, including Johnson-Cook material coefficients determined experimentally in previous work [97]. The forming of plates of this

aluminum alloy typically results in flattened grains near the surface often elongated to a few hundred microns in length. This could interfere with the consistency of LSP results [34], [104], so 25.4 mm plates were faced down to thicknesses of 10.16 and 15.24 mm, exposing the smaller (~ a few microns) and more uniform grain morphology in the middle of the plate. This improved morphology greatly reduces inconsistencies due to micromechanical effects within the area of the laser treated spot.

Samples of two different thicknesses (10.16 and 15.24 mm) were used for a validation of the boundary conditions of the finite element model. The actual treatment process utilizes a rubberized damping layer behind the plate to prevent or reduce stress wave reflection. The effectiveness of this backing could change the residual stress field in specimens of varying thicknesses. Since the residual stress field was nearly the same in both thicknesses of specimens, then the damping layer was quite effective, and the use of infinite elements in the FE model was an acceptable modeling technique. If there had been evidence of residual stress field variation due to wave reflection, then the FE model would have benefited from a finite backing with different material properties to more closely match the damping material.

Validation of the predicted pressure impulse was accomplished on 15.24 mm thick mill annealed titanium samples, for which the Johnson-Cook material properties have also been well researched in past work [97]. The same sample manufacturing and testing methods were used as in the aluminum, but the data was kept “blind” for the initial part of the study. Once the pressure impulse had been deduced by the optimization

code based on data from the aluminum samples, this pressure impulse was modeled onto titanium and validated against the collected data.

During the previously mentioned facing process, all plate specimens were machined to exacting tolerances and very fine surface finish in order to reduce negative effects due to surface variation (drawings can be seen in Appendix C. Specimen Machinist Drawings). The machining turned out even more accurate than drawing specs, resulting in flatness to within 0.002 mm across the surface of the plates. Both the 10.16 and 15.24 mm thick aluminum plates were approximately 230x460 mm in size and the eight LSP treated spots were spaced evenly in two rows of four with edge distances of approximately 58 mm and center to center spacing of approximately 116 mm. Figure 24 shows the aluminum plate in gray with the eight evenly distributed LSP treated spots as blue squares spaced far enough apart to eliminate stress field overlap and shock reflection from the edges of the plate.

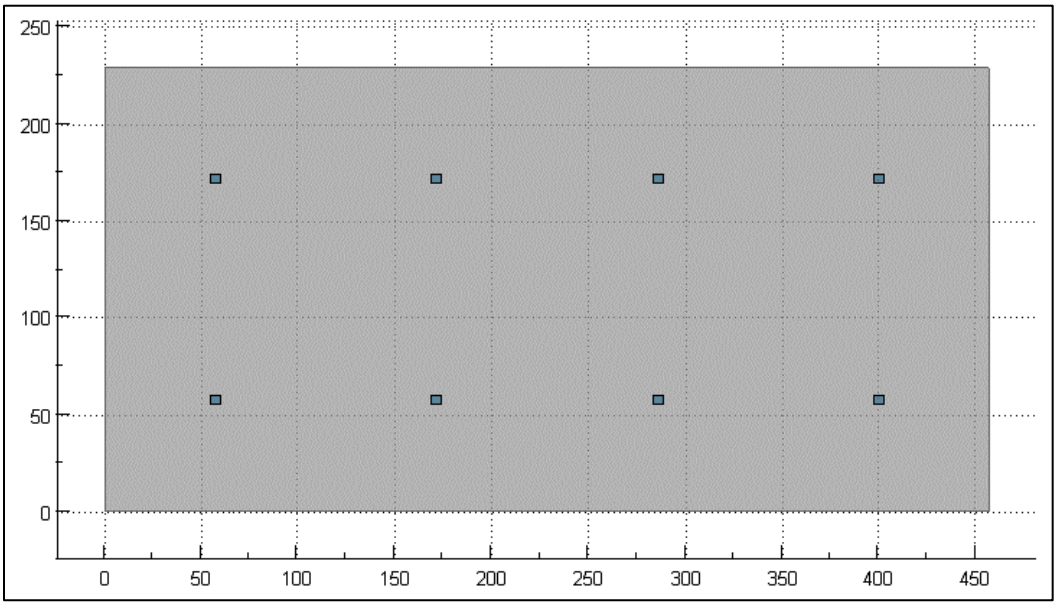

Figure 24: Aluminum plate sizing and LSP spacing diagram

The titanium plates were procured as surplus from another AFRL contract and thus were sized differently at approximately 100x500 mm. Four LSP spots were spaced evenly on the plates with 50 mm edge spacing and 130 mm center to center spacing to leave enough space in between LSP spots for the far field residual stress measurements.

Laser treatment was accomplished by Metal Improvement Company (MIC) in California. MIC uses a 16 Joule (+/-10%), neodymium-doped glass laser or ~1064 nm wavelength (infrared), with a fixed pulse duration of 18 ns (+/-3 ns). The beam is anamorphically shaped into a square which can be focused to a wide range of sizes to control the power density of the treatment. The chosen power density had to be one which was not too powerful for aluminum, but powerful enough to induce a measurable residual stress in titanium. Based on many examples from the literature reviewed, and confirmed by MIC, 4 GW/cm^2 was chosen for this work. This dictated a 4.7 mm spot width. The single impulse treatment spots were spaced across large plates with sufficient edge distance and center-to-center spacing to prevent reflected shock waves or overlap of residual stress zones and leave space in between treated spots to measure far-field residual stresses.

Surface deformation was measured using a Nanovea chromatic confocal contactless optical profilometer. This profilometer uses axial chromatism to measure vertical surface displacement with a maximum error of only 40 nm over a 400 μm measurement range (see Appendix H. Optical Profilometer Calibration Documentation). Residual stresses were measured by hole-drilling, accomplished by Hill Engineering in California. A 1.016 mm diameter hole was used in the center of the LSP treated spot,

measuring at 0.0254 mm increments to a depth of 0.508 mm. Eight samples were tested and averaged for each material or thickness in order to improve confidence in the residual stress measurement. Three additional hole-drilling measurements were conducted in each plate in a far field location to determine the non-LSP affected or "baseline" residual stresses. Representative images of these plates can be seen in Figure 25 & Figure 26.

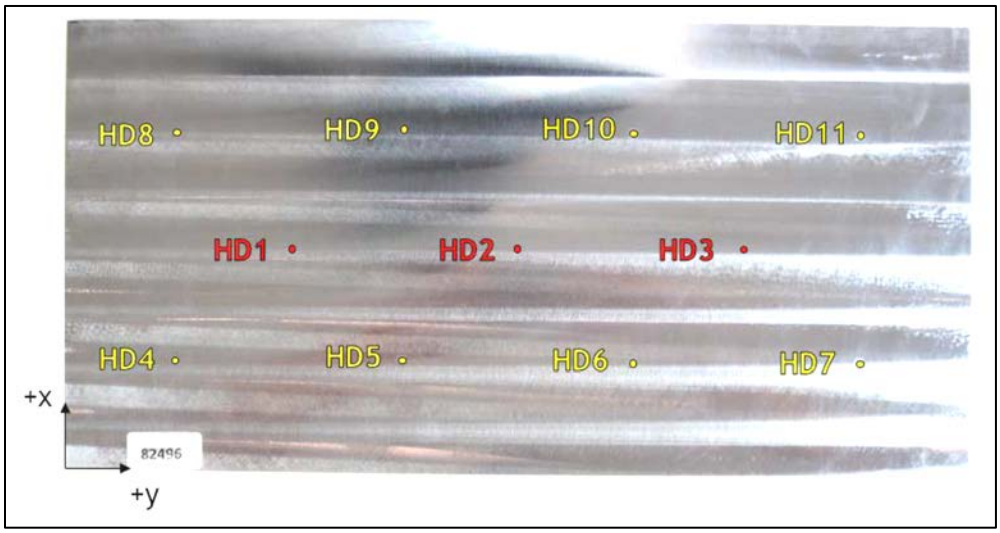

Figure 25: Representative aluminum plate and hole-drilling locations (LSP treated spots in yellow and far field baseline locations in red) [105]

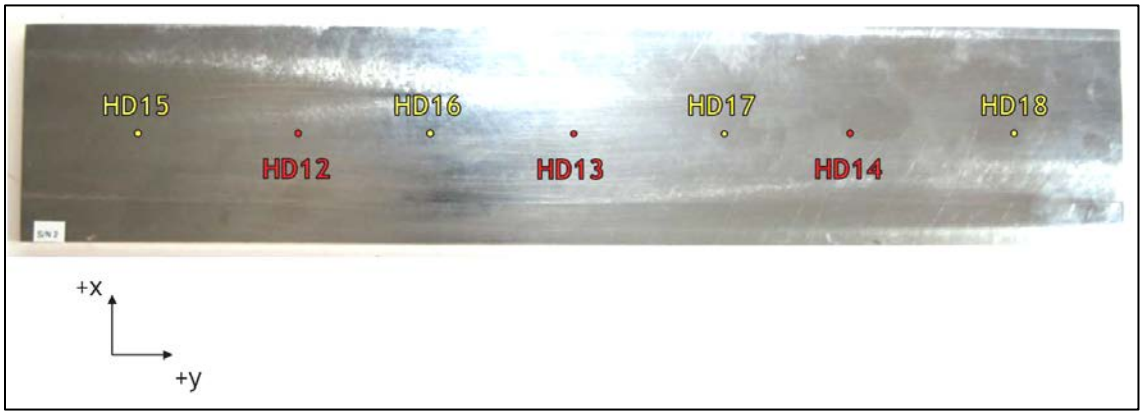

Figure 26: Representative titanium plate and hole-drilling locations (LSP treated spots in yellow and far field baseline locations in red) [105]

IV. Results and Discussion

Initial Round Laser Spot 3D Model Results

For the preliminary round spot model, the FE results for pressures varying from 1.1 to 1.8 GPa can be seen below. The surface displacement (Figure 27) shows the expected dimple shape, though with some jaggedness, indicating the need for a higher resolution mesh; later models had a uniform mesh of a finer resolution to eliminate high aspect ratio elements. High aspect ratio elements are those whose length is significantly greater than the width. This geometry becomes problematic when the stress field is very non-linear. The peak displacements for 1.8 GPa peak-pressure approached 8 μm. Comparatively, the work by Hfaiedh showed peak displacements of 10 μm for a 5 GPa impulse [51].

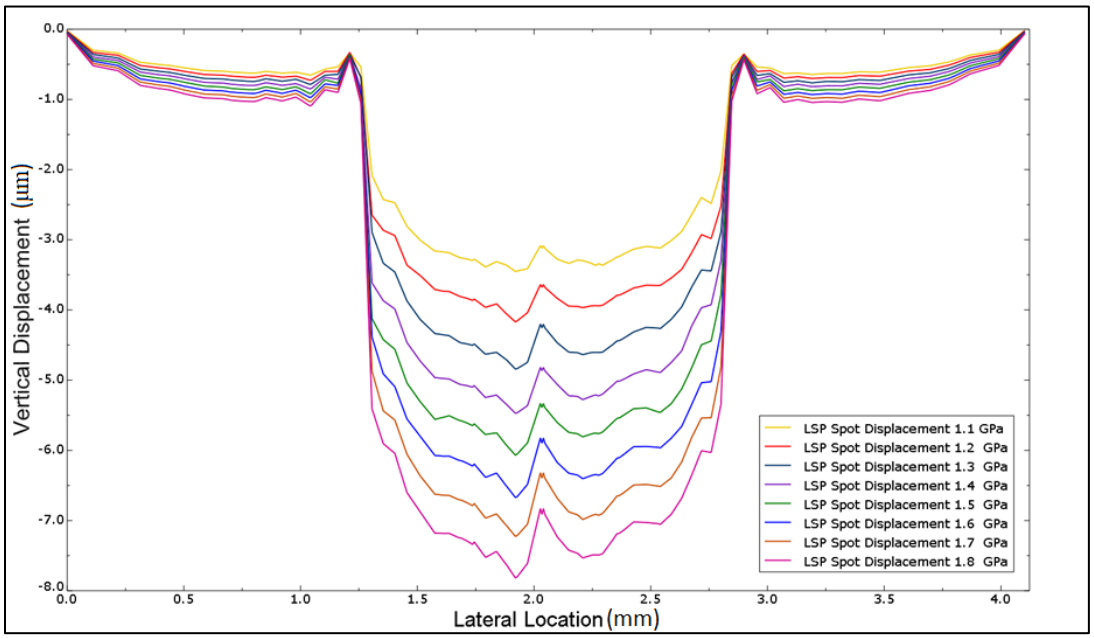

Figure 27: Surface displacement for various pressures in 2050-T8 aluminum model[98]

This difference suggested that the material model was allowing too much compliance for the input energy. The addition of an EOS alleviated this fact by providing a mechanism for a great deal of energy (from hydrostatic compression) to change the material density along the stiffening Hugoniot line, resulting in less plastic deformation at higher pressures than the plastic strain curve alone. Further, the surface displacement does not reach a zero displacement point until the very last node which is adjoined with the infinite element, indicating that the simulation needed a bigger working section; later models had an increased overall width to account for this need.

The single direction, in-plane residual stress at the surface (Figure 28) approximately conformed to the expected shape based on published work. The round laser spot showed a more tensile (or less compressive) peak in the center, and this has been noted in other work (for example [39], [47]). The peak compressive stresses for the 1.8 GPa impulse were around 350 MPa, compared to about 310 MPa for the 2 GPa impulse modeled by Hfaiedh [51]. This, again, was due to the presence of too much plastic deformation, and was alleviated in later models with the addition of the EOS. The tensile peaks at the outer boundary of the treated spot were larger than expected, approaching the material yield stress. This was another indication of excessive plastic deformation, but could also be partially explained by the higher aspect ratio elements surrounding the laser treated spot, as well as a mesh which required further refinement to handle the large stress gradients.

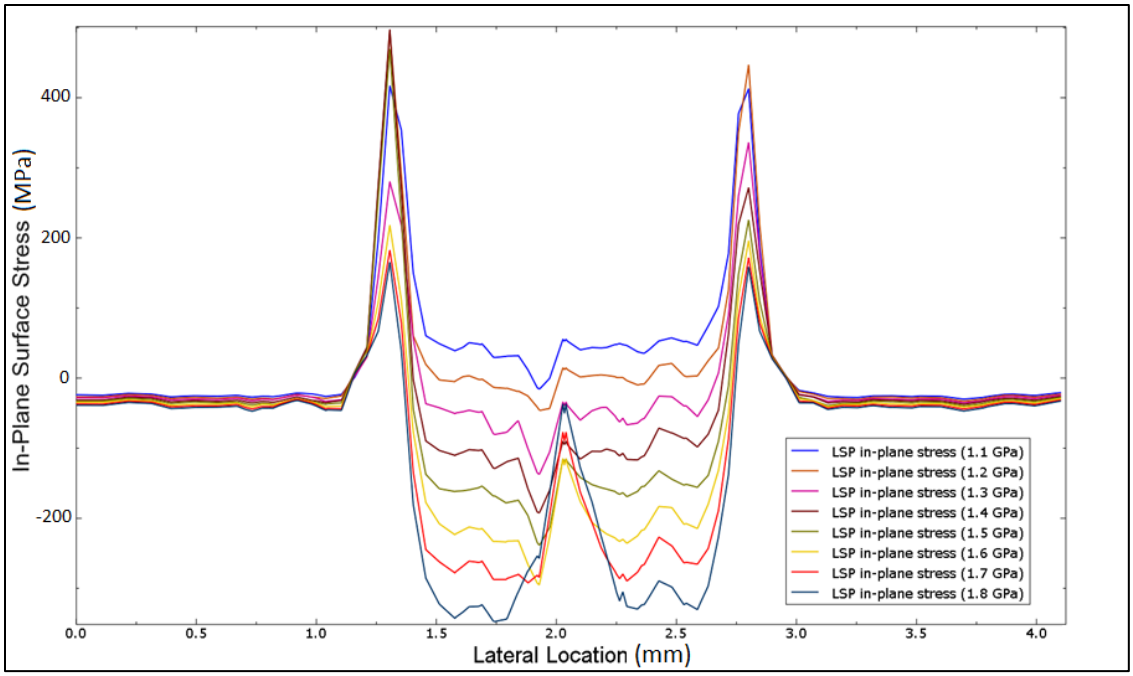

Figure 28: Surface in-plane residual stress field for various pressures in 2050-T8 aluminum [98]

One interesting characteristic of this model was an increasingly tensile peak in the middle of the treated spot under higher peak pressures. Some prior work documented this type of behavior [50], however, this model exhibited nearly zero residual stress at the very center of the spot for the highest (1.8 GPa) pressure. Again, this phenomena has been seen in past work ([39], [47]) though not to this extent. This was taken as another sign of the need for mesh refinement and the addition of the EOS, but may have also been more prominent due to the element-wise stress extraction, a measurement method which cannot be replicated in laboratory experiments. This will be discussed further below.

The residual stress at the center of the LSP spot, and into the depth was observed to follow the expected transition from compressive to lightly tensile as seen in Figure 29. The compressive stresses were less than, and not nearly as deep as would be expected

from a more powerful LSP treatment. This is likely due to the same mechanism which caused the tensile spike in the center of the laser treated spot. Residual stress into the depth can be seen in Figure 29.

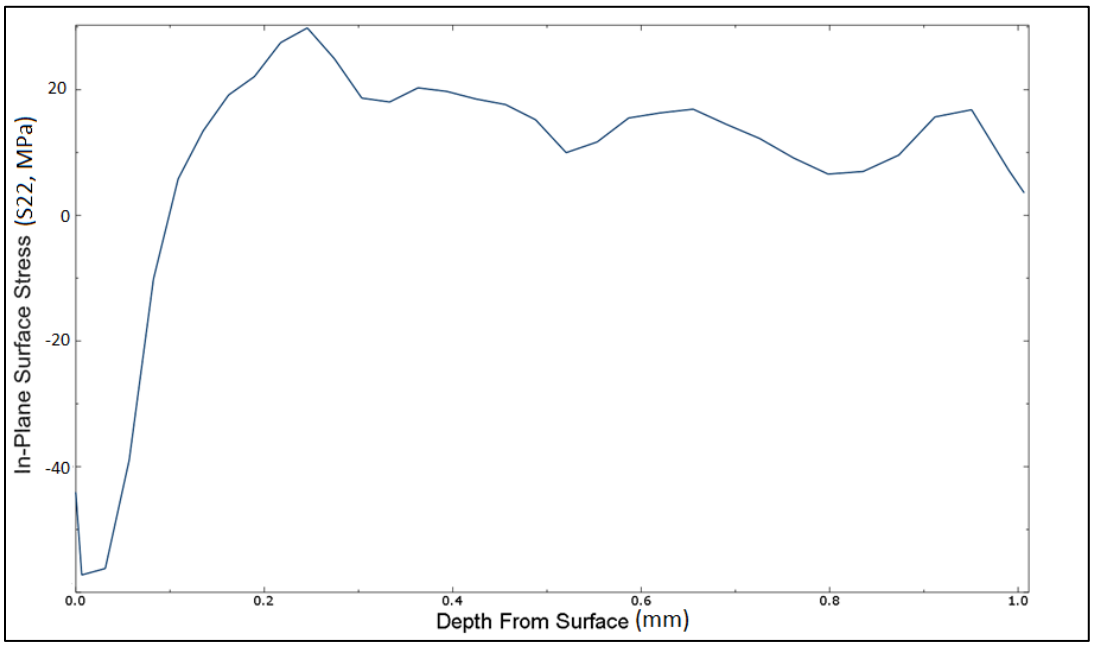

Figure 29: In-plane stress (σ22) at varying depths below the surface in 2050-T8 aluminum [98]

Again, this more tensile feature was noted in past research [50], however not to this extreme. The stress profile in Figure 29 was established by tracing a single line of elements down the center of the laser spot into the depth of the material. This represents a very small "gauge volume" over which the residual stress is being measured, one which would not be possible to reproduce experimentally. That is to say, it is quite possible that this accurately reflects a profile of residual stress which does exist in real specimens, but cannot be measured because real-world tests require a gauge volume large enough to produce measured changes within the resolution of laboratory equipment. The method of extracting these FEM results was ultimately modified to more closely replicate how

residual stress is measured in experiment, that is, by averaging the stress over increment discs of material drilled down to a given depth.

The results from this preliminary model led to many refinements for the subsequent models. First was the refinement of the mesh, and consequently, time increments, for better resolution of the LSP event. Also, the EOS was implemented to handle hydrostatic shock of the immense pressure impulse. Finally, the method of extracting residual stress was modified to more readily compare to experimental procedures.

Material Model Verification Results

To verify the material model, a trace of stress, strain, and density was conducted through time on a single element slightly below the LSP treated surface. Also, a work and energy exchange was tracked for the entire model. These were compared to similar outputs highlighted in the previous chapter (Figure 15 and Figure 16).

The single element trace can be seen in Figure 30. It begins with a short time delay over which no changes occur as the shock is still travelling from the treated surface toward the selected element. The arrival of the hard shock brings about a dramatic increase in density (shown in light blue), and consequently compressive stress (dark blue), which is very short in duration, and imparts all of the plastic strain (green line) which occurs in the event. The subsequent stabilization, after the shock has passed, results in a density which is slightly higher than the original density of the material due to permanent plastic deformation.

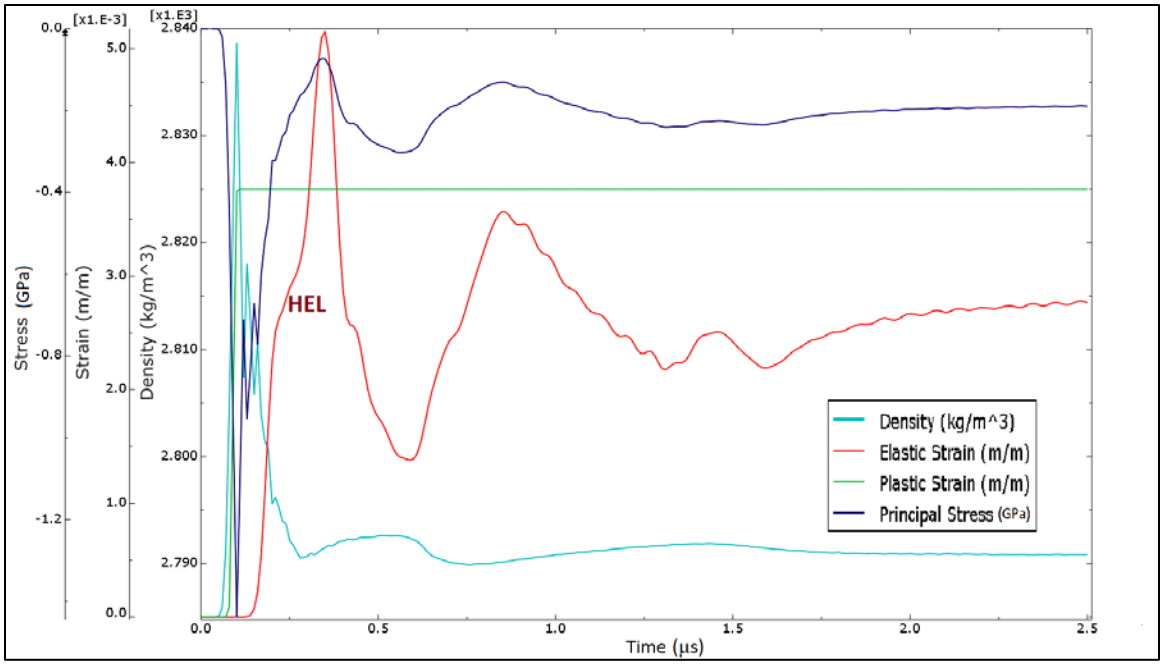

Figure 30: Single element trace of stress, strain, and density through the LSP event

After the highly compressive shock response, the stress component exhibits a more tensile rebound, followed by a period of dynamic fluctuation toward the equilibrium compressive residual stress state. This stress result matches very nicely with the right portion of Figure 15 in the previous chapter. Finally, the trace of elastic strain shown in red is a reflection of particle position and velocity. The elastic wave front arrives well after the shock and exhibits the expected HEL "knee" which was shown in the left portion of Figure 15. After the initial elastic wave propagation and density stabilization, the elastic strain directly reflects the remaining stress. When the model reaches equilibrium, both stress and strain values retain non-zero values that correspond to the residual stress state of the single element after LSP treatment.

Next, the work energy analysis of the entire model was used to further verify the material response. This can be seen in Figure 31. The total external work (shown in red)

is accumulated over the short (~200 ns) pressure impulse time. This work transfers energy into the model in the form of kinetic (purple line) and potential energy which add up to the total internal energy (blue line). Kinetic energy is lost in this highly dynamic system to plastic dissipation (green line) as well as viscous damping (orange line).

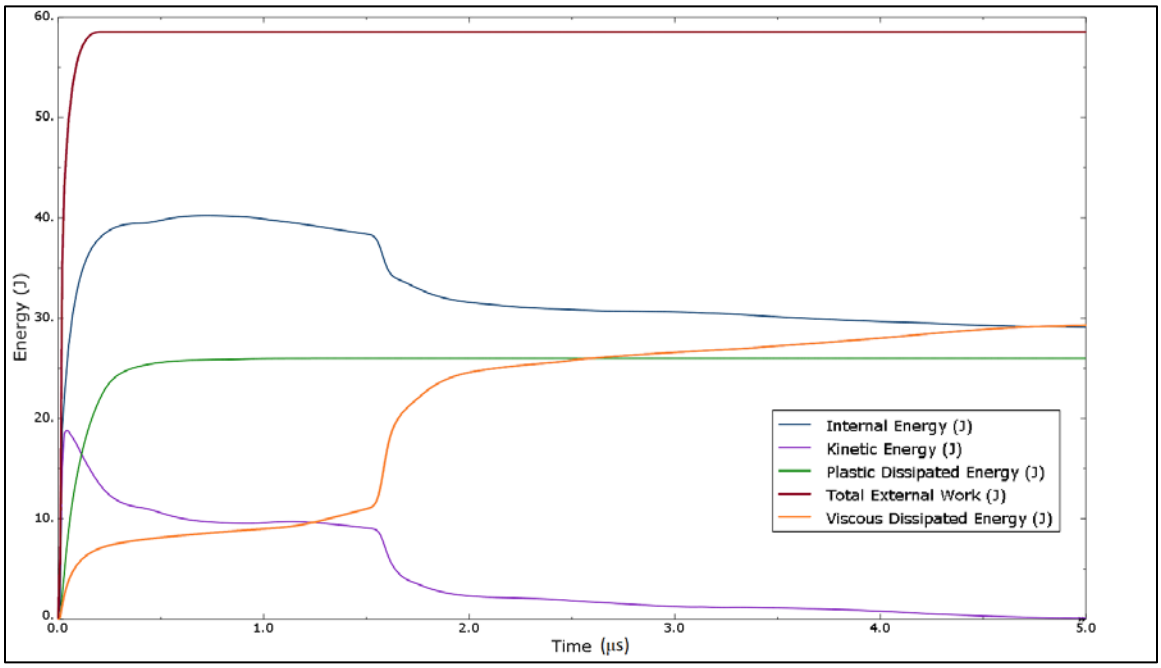

Figure 31: Whole model work and energy exchange over the LSP event

When the kinetic energy has been fully dissipated, the remaining internal energy in the blue line is proportional to the elastic residual stress contained in the model at the end of the LSP event. This all matches perfectly with the expected results shown in Figure 16 of the previous chapter.

These results showed that the combination Johnson-Cook, and Mie-Grüneisen model handle the material response expected for an LSP event and demonstrate the competency of this verified material model used for the remainder of the current work.

Finite Element Model Type Comparison

As discussed in the previous chapter, a comparison study was conducted to determine if a 2D model was accurate enough to represent a 3D model. The residual stress results were the focus of this comparison (see Figure 32), as that is the outcome which is most critical to match for model predictive accuracy. When compared to a full 3D model, the quarter-symmetry 3D model matched most closely, while also reducing computation time. Still, approximately 50 CPU-hours were required to run the quarter-symmetry 3D model. While this might seem reasonable in itself, when paired with potentially a thousand iterations through an optimization loop, the optimization run time was unreasonably long (weeks) for an initial study on this method. The plane-strain model results showed higher compressive residual stresses near the surface and lower compressive residual stresses deeper below the surface. It was expected that a plane-strain model might more accurately reflect a square laser spot, since there would be less "lensing" or "splash" of stresses converging in the center as in a round spot, or axisymmetric model. This was not the case, however, and the Poisson's ratio effect of this model skewed the stress results such that the x-direction and y-direction stresses were not equal as was seen in experimental data. While there was less lensing, this did not more accurately represent the square spot which seems to have some center-lensing, but not as much as a round spot. The axisymmetric model essentially turned the square spot into a round spot for which the diameter was equal to the width of the square spot. This seemed to be the best compromise of all models. It was extremely efficient in terms of computation requirements, and matched within 2% the full 3D residual stress results at

the deepest points. The model did, however exhibit some predictable, more tensile divergence of stresses nearer to the surface. This is a consequence of the aforementioned "lensing" which is caused by the round spot, and seemed consistent enough to anticipate across a few trial pressure impulse shapes. The comparison of the residual stress profiles from each model can be seen in Figure 32.

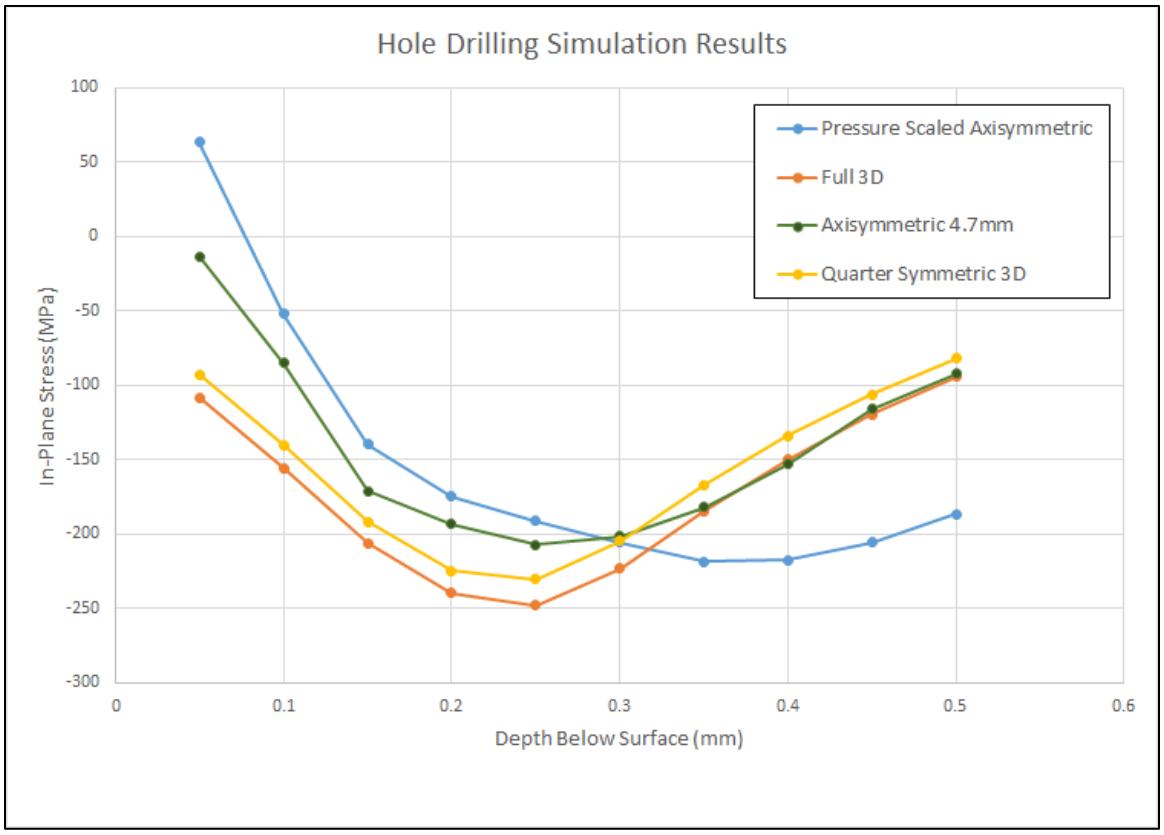

Figure 32: Comparison of residual stress profiles in four FE model configurations

An axisymmetric model with an increased peak pressure and one with increased width were also tested to determine if better matching the overall energy of the pressure impulse would compensate for the simplification of the square spot to an axisymmetric model. Pressure and diameter scaling did not improve the residual stress match, therefore

the original 4.7mm wide axisymmetric model was deemed close enough to represent the 3D event by using a simple linear adjustment to anticipate and account for the more tensile behavior near the treated surface. This linear adjustment would serve as a filter of the model residual stress results to better replicate 3D results and reality. A different linear equation was applied to each residual stress depth individually based on a regression fit of three points corresponding to three different applied peak pressures (see Table 7). In the equations, "Y" denotes the equivalent 3D residual stress value in MPa, and X denotes the axisymmetric model stress value in MPa. All associated linear conversion equations have an R^2 value better than 0.963. The full, data-matching optimization model was run both with, and without this linear correction method applied in order to determine its utility.

Table 7: Pointwise linear conversion equations and associated R^2 fit

Depth Increment	Linear Conversion Equation	R^2 value of fit
1 (0.05 mm)	Y=4.678*X+44.8	0.963
2 (0.1 mm)	Y=1.546*X+23.8	0.985
3 (0.15 mm)	Y=1.428*X-37.6	0.996
4 (0.2 mm)	Y=1.455*X-40.1	0.988
5 (0.25 mm)	Y=1.568*X-78.6	0.984
6 (0.3 mm)	Y=1.579*X-95.4	0.987
7 (0.35 mm)	Y=0.986*X+4.8	0.973
8 (0.4 mm)	Y=0.75*X+34.6	0.964
9 (0.45 mm)	Y=0.851*X+20.5	0.993
10 (0.5 mm)	Y=1.061*X-3.7	0.999

Optimization Proof of Concept

As previously mentioned, the Hooke-Jeeves algorithm settings can be changed. The number of iterations to converge to a solution typically varied between 60 and 90

(taking between 2.4 and 4 hours of computation time), so the maximum number if iterations allowed was set to 150, and never limited the algorithm. Further, the initial step size and reduction factor can be changed to affect the speed and accuracy of model convergence. An investigation was conducted to find settings for these values which achieved fast yet accurate convergence to an optimal solution. Both variables seemed to have a relatively small effect on the number of iterations to convergence, but the accuracy was more readily influenced, most greatly by the initial step size value. A summary of a few examples of paired Hooke-Jeeves variable settings are seen in Table 8. While this investigation was not exhaustive in the range and pairing of variables, it was deemed sufficient and favorable to achieve an objective function minimization to 0.0797 within 80 iterations. Further objective function improvement did not occur beyond this point. [43]

Table 8: Hooke-Jeeves algorithm settings variable investigation, most favored settings in yellow [43]

Hooke-Jeeves Step Reduction Factor	.1	0.5	0.5	0.25	0.75	0.75	.75	0.9
Hooke-Jeeves Initial Step Size	0.75	0.5	0.25	0.25	0.5	0.1	0.01	0.01
Resultant Objective Function	0.109	0.102	0.099	0.081	0.104	0.180	0.0797	0.0797
Iterations to Convergence	92	73	61	83	70	43	80	80

It should be noted that the actual value of the objective function carries little meaning in itself, though in this case it serves as a reasonable metric by which to improve the algorithm settings if all other variables remain constant. [43]

The next investigation studied the effects of objective function weight factors on the quality of data-matching. The goal being to improve the modeling of the LSP event, it is desirable to improve the matching of the surface displacement and residual stress field. The maximum percent difference of residual stress and surface displacement was compared for various weight factor ratios. The weight factor ratio, defined as W_1/W_2, can be thought of as how much the residual stress was favored over the surface displacement. A ratio of one means they were weighted equally, greater than one means that residual stress was weighted more heavily, and less than one means surface displacement was weighted more heavily. The results of various weight factor ratios is summarized in Table 9 in which W_1 corresponds to residual stress preference and W_2 corresponds to surface displacement. [43]

Table 9: Effect of objective function weight factor on maximum difference from target values [43]

Weight Factor Ration (W_1/W_2)	1.0	10.0	0.1	4.0
Residual Stress Maximum Difference (%)	15.9	1	60	6.2
Surface Displacement Maximum Difference (%)	4.8	11.1	6.3	4.4

These results give some flexibility to the use of this model. If the user wishes to better match surface displacement, as may be needed in a surface quality improvement situation, simply increase the corresponding weight factor relative to the other. The reverse is true to better match the residual stress field. The purpose of this work is to find an optimal match which is balanced for both metrics, and so weighting residual stress 4:1 relative to surface displacement most greatly reduced the combined maximum percent differences. [43]

The above trials were all conducted by setting the initial pressure parameter inputs to the smallest values to be consistent. To determine the effect of initial conditions on the convergence to the result, ten initial pressure impulse parameters were tested using the aforementioned best algorithm settings. These initial conditions consisted of one iteration where all parameters where set to the lowest values, and one where they were set to the highest. The remaining eight iterations were combinations of randomly chosen combinations of first and third quartile values of every parameter. The results from this study can be seen in Table 10.

Table 10: Pressure impulse results of 10 initial condition trials compared to target values (italicized)

Trial Numbers	**1,4-6**	**2,3,8**	**7,9,10**	***Tgt.***
Peak (GPa)	5.0	5.25	5.0	*4.0*
Curvature	2.25	2.0	2.0	*2.0*
Duration (ns)	200	200	210	*210*
Peak Width	0.9	1.0	0.9	*1.0*
Dissipation Rate	1.0	.08	1.1	*1.0*
RS Max % Difference	6.2	7.1	5.8	*0*
Displacement Max % Difference	4.4	5.8	4.1	*0*

Over all of the trials, the algorithm never landed exactly on the target pressure impulse parameters. The results were divided between three converged results. In each case, there was a trade-off in work between parameters, for example a higher peak pressure with a shorter, faster dissipating pressure impulse. These balances of work energy were what allowed three near-optimal solutions to achieve residual stress and displacement results within, at worst 7.1%, of target results. Prediction of residual stress to within 5.8% as in trials 7, 9, and 10 would be deemed sufficient for many engineering design applications. It showed, however, that the optimization space had varying combinations

which achieve similar results. While this is not ideal for finding a single optimal solution, the purpose of the method is to arrive at a "best-guess" pressure impulse shape which can accurately predict residual stress results in the FE Model. To this end, any of the results achieved above would be acceptable residual stress predictions.

Having streamlined the optimization model performance within the discretized optimization space, those model settings were applied to run over a continuous optimization space with the same upper and lower bounds. As would be expected in a space of infinite pressure impulse combinations, the computation time to converge to an optimal impulse shape was greatly increased to over 640 CPU-hours, requiring ten times as many iterations. The results, however, were the most accurate of all. The maximum difference of the residual stress relative to the target values was 4.5% and the maximum difference of the surface displacement results was 2.5% (see Figure 33). The shape of this optimal pressure impulse in time and space compared to the target pressure impulse can be seen in Figure 34 and Figure 35. [43]

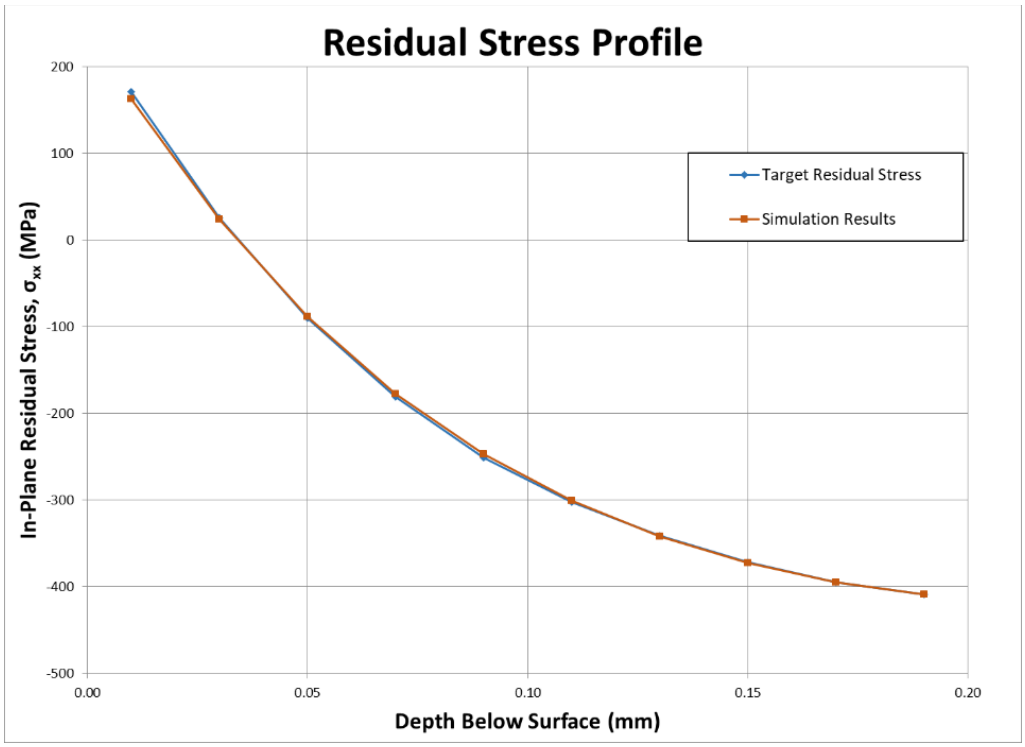

Figure 33: Continuous optimization space model residual stress matching results [43]

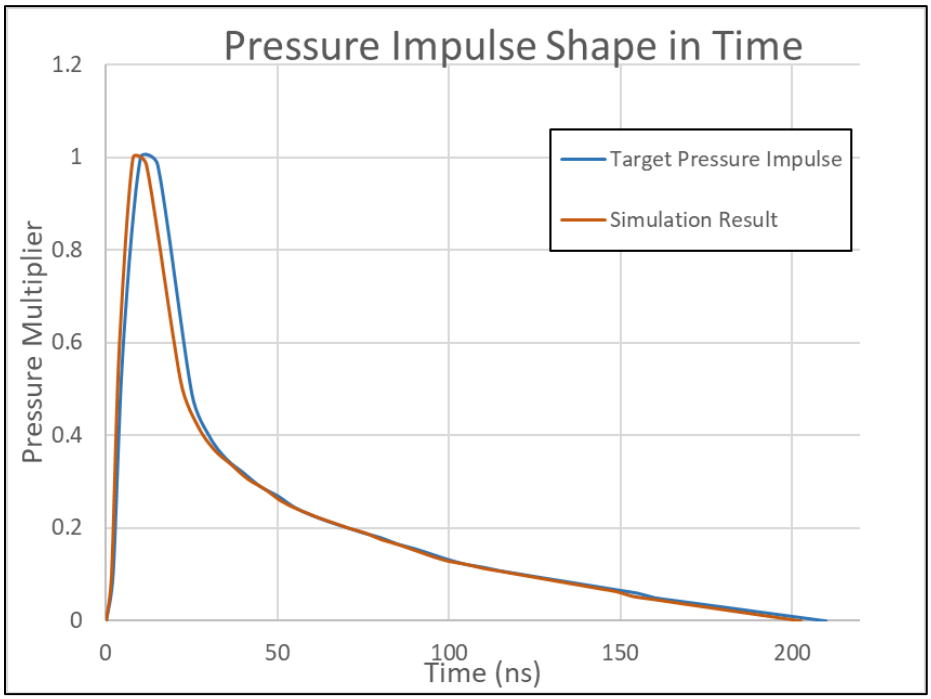

Figure 34: Continuous simulation predicted pressure impulse time profile compared to target [43]

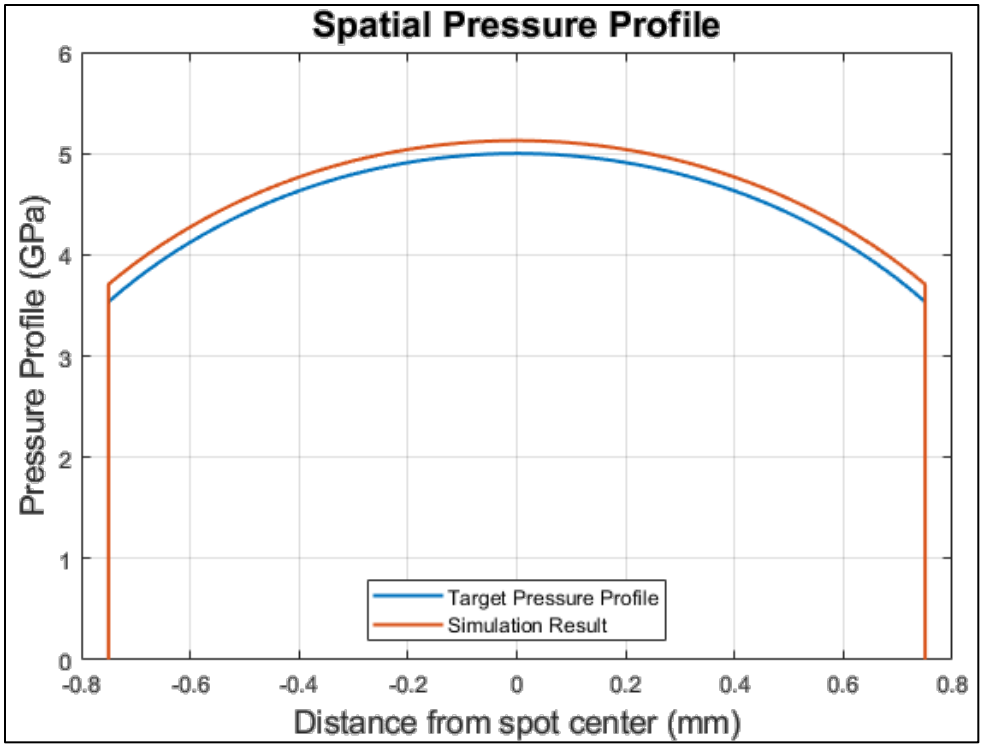

Figure 35: Continuous simulation predicted pressure impulse spatial profile compared to target [43]

Experimental Data

Before proceeding to the final data-matching results, it would be convenient to first take a look at the data which was collected for matching and validation. Recall that four plates were LSP treated; two aluminum plates of 10 mm and 15 mm thicknesses, each with eight laser spots, and two 15 mm titanium plates each with four laser spots. After LSP treatment, specimens underwent optical profilometry. Displacement data in the form of over 128,000 (x, y, z) pointwise coordinates were generated for each laser spot, and these were plotted as a surface contour as seen in the example in Figure 36. Each LSP dimple had different feature such as the surrounding machine marks, or small bump anomalies. The dimple shapes had some uneven rounding of corners and were not

perfectly square. Some of these features were unique in each individual LSP dimple, others appeared to be consistent across every treated spot.

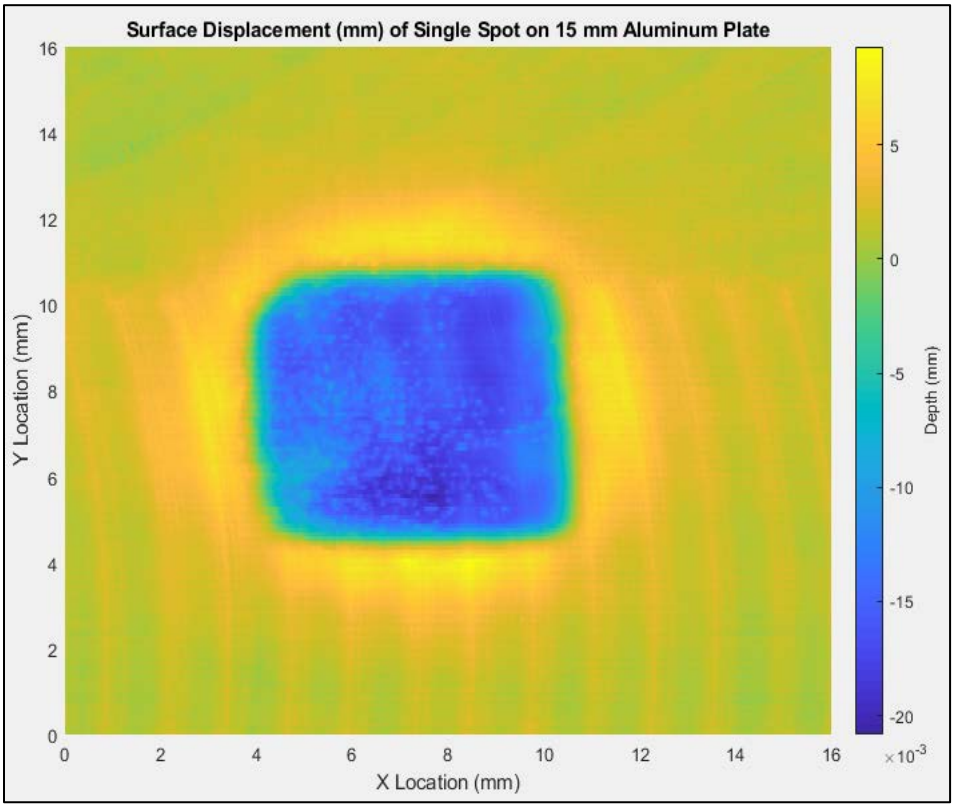

Figure 36: Single LSP spot raw surface displacement plot from 15 mm aluminum specimen

By pointwise averaging the surfaces together, anomalous traits were smoothed out, and the consistent surface displacement features of the LSP process were more easily seen (as in Figure 37). The surface consists of a generally flat lower indentation with raised areas around the perimeter. This raised area around the dimple was most prominent along the sides, and somewhat diminished around the corners. A few of the broad bumps contained within the LSP dimple were consistent across all treated spots indicating some consistent mechanism within the process which forms them. This might be some sort of wave

reinforcement or cancelation, or unevenness of laser power, but is consistent from pulse to pulse.

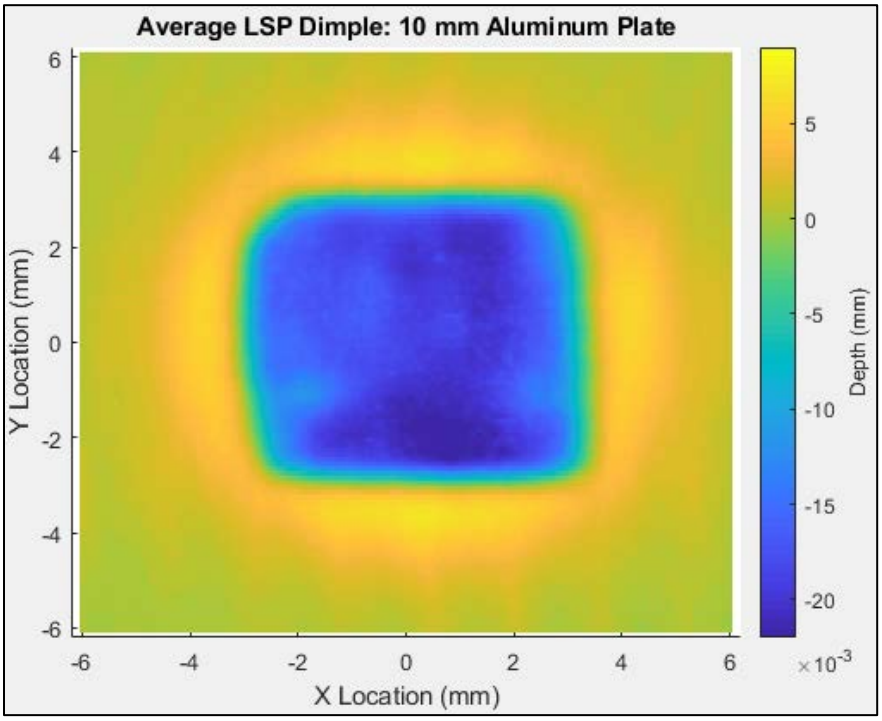

Figure 37: Average of 8 LSP dimples from 10 mm aluminum plate

This averaging was done via MATLAB code (see Appendix D. Surface Displacement Averaging MATLAB Code) by aligning the dimples both vertically and horizontally then trimming points outside the area encompassed by the FE model, and taking the pointwise average of the z-value across eight LSP spots for a given plate thickness or material combination. Titanium plates were averaged together as one since the two plates were identical in thickness.

Cross-sections cuts were taken through the middle of these spots to more easily compare 2D surface displacement and see the variation across all eight LSP spots for each plate in Figure 38, Figure 39, and Figure 40. A slight slope can be noticed from one

side of the spot to the other, consistent across all dimples, with the right side indented slightly deeper than the left. With the exception of a just one markedly different surface displacement, the surface displacement was quite consistent across all LSP spots in a given material. The titanium plate, however, under the same treatment, deformed only about 1/5th that of aluminum (~4 microns as compared to ~20 microns in aluminum) as would be expected for a stiffer and less ductile material. This also resulted in a higher noise ratio which made 3D surface averaging infeasible as the dimple surfaces were difficult to accurately align. The 15 mm aluminum plate displacements are in Figure 38, the 10 mm aluminum plate displacements in Figure 39, and the titanium plate displacements are in Figure 40 below.

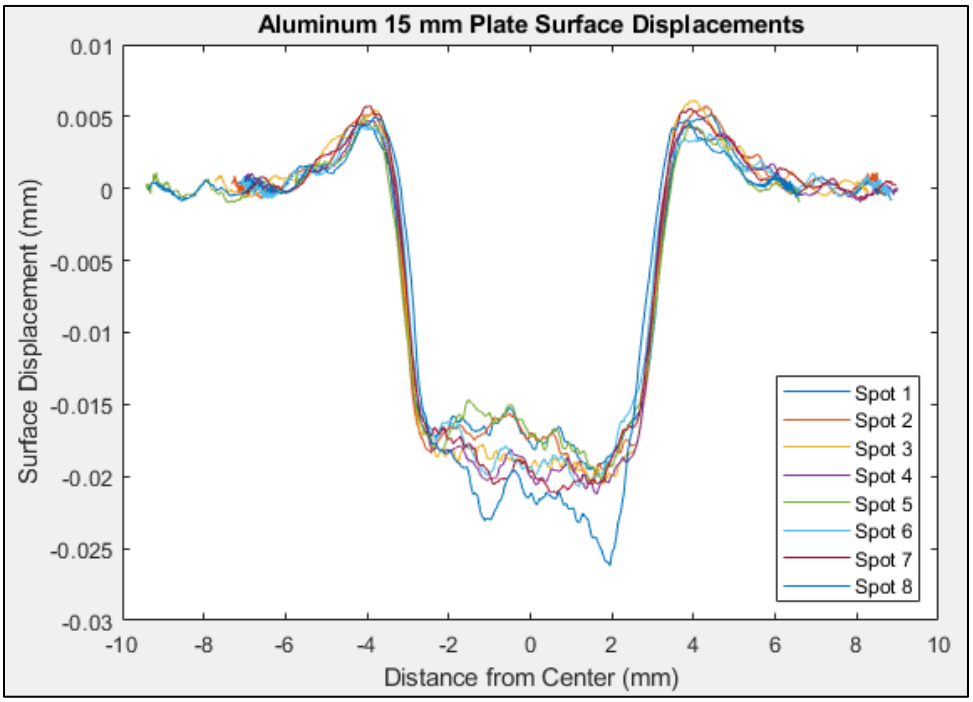

Figure 38: Middle cut surface displacement from all 8 LSP spots on the 15 mm aluminum plate

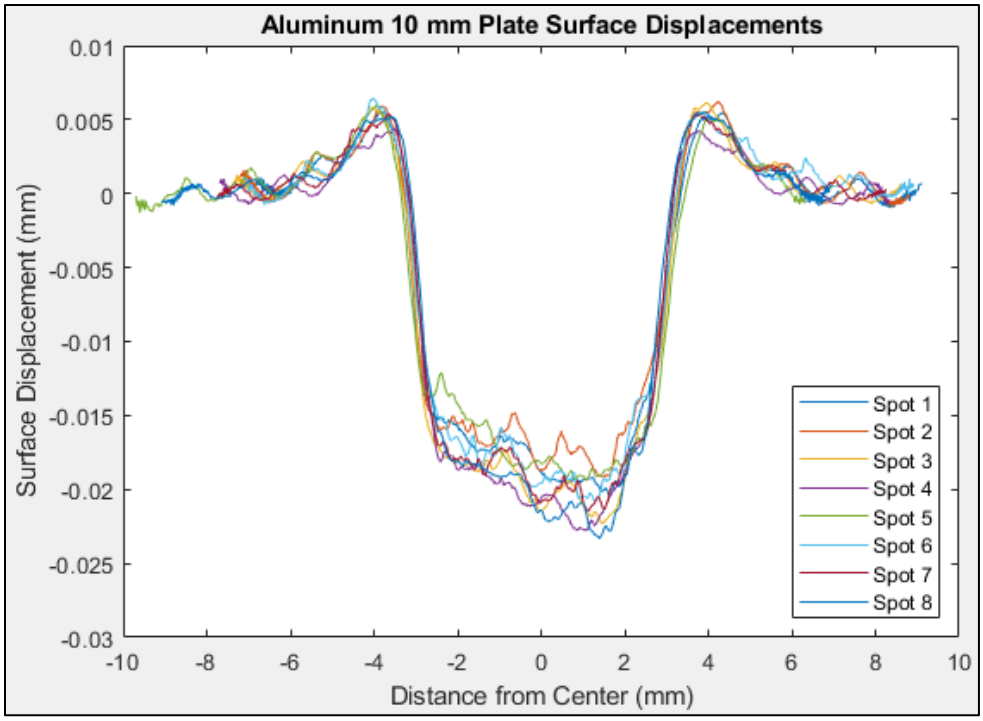

Figure 39: Middle cut surface displacement from all 8 LSP spots on the 10 mm aluminum plate

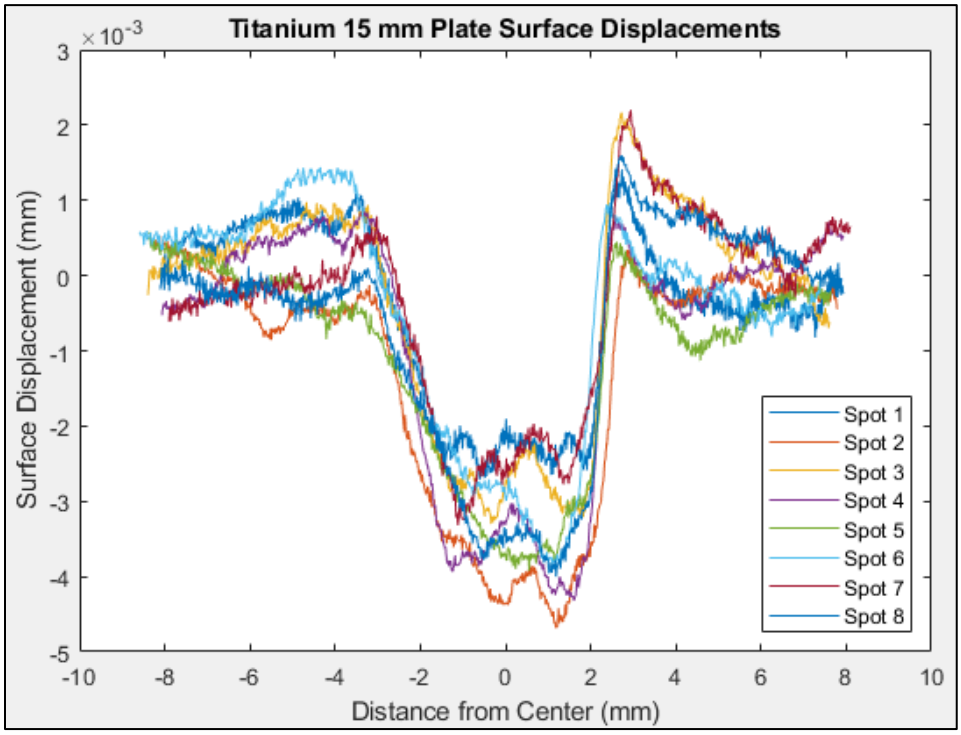

Figure 40: Middle cut surface displacement from all 8 LSP spots on the 15 mm titanium plate

To get a better idea of the consistency and to make the displacement data more useable for data-matching, average values were calculated for each plate, to include plus and minus one standard deviation "brackets." All plates have similar standard deviations, though as a percent of maximum displacement, the aluminum plate displacements appeared more consistent. These averages in aluminum are of a reasonable consistency to facilitate data-matching. The mean and +/-1 standard deviation displacement plots for the 15 mm and 10 mm aluminum and 15 mm titanium can be seen in Figure 41 through Figure 43, accordingly.

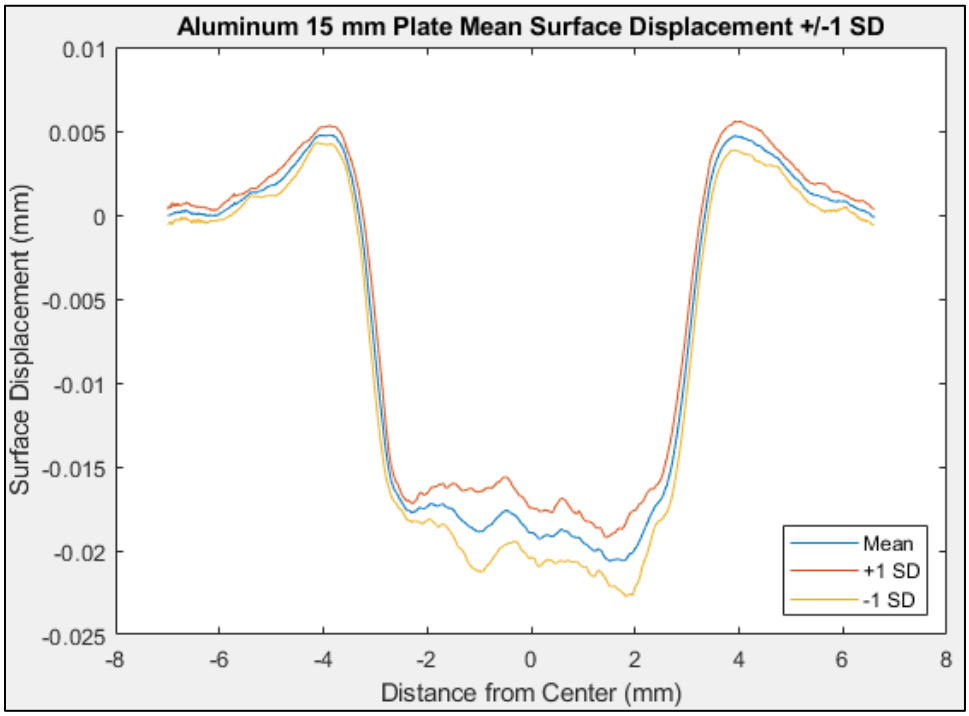

Figure 41: Mean and +/-1 SD surface displacement for the 15 mm aluminum plate

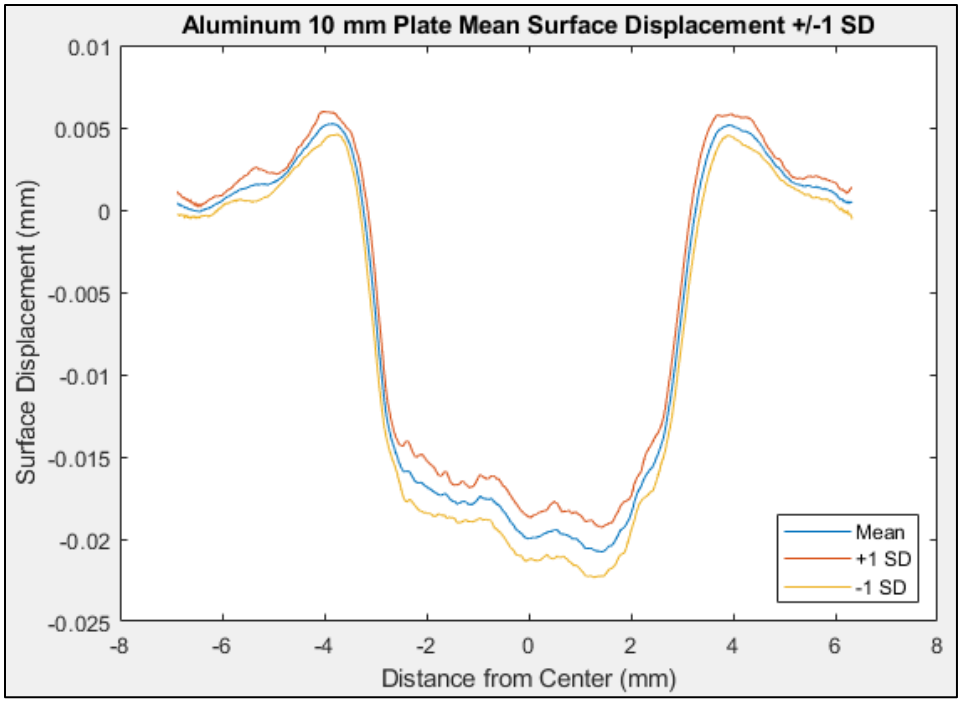

Figure 42: Mean and +/-1 SD surface displacement for the 10 mm aluminum plate

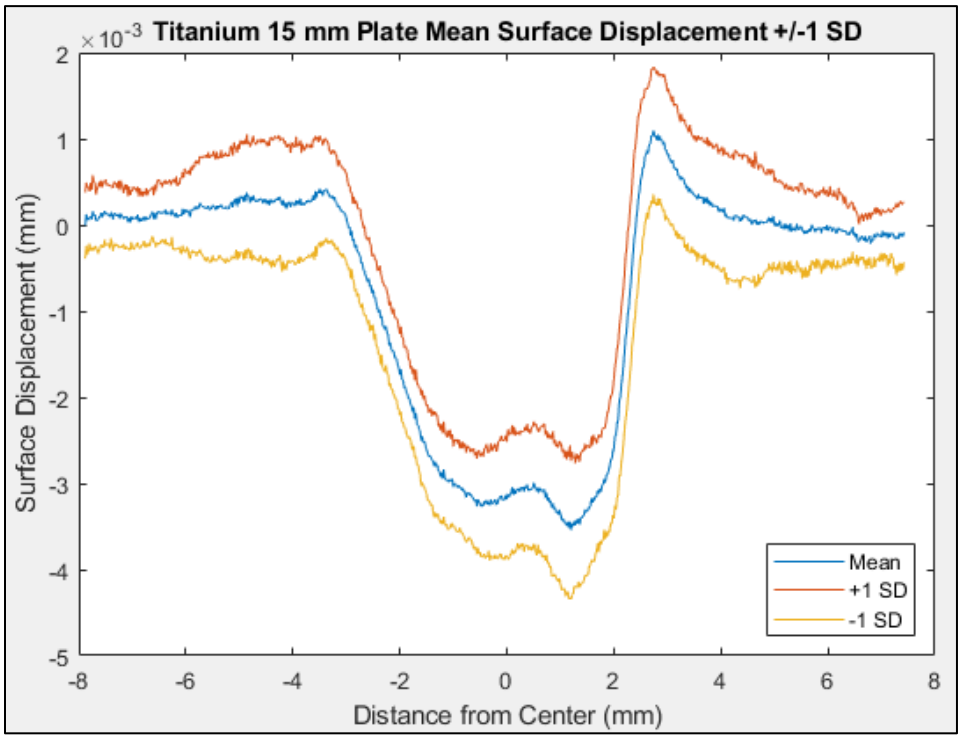

Figure 43: Mean and +/-1 SD surface displacement for the 15 mm titanium plate

The “right-sloping” trends are more clearly visible in these averages, and even continue into the left “side-wall” of the titanium LSP spot. Averaging of the right and left halves of the LSP treated dimple removed concern for the purposes of matching a one-sided axisymmetric model to the averaged data in the current work. However, some discussion of this interesting anomaly is warranted. One might easily consider the beam angle of incidence as a possible cause of what appears to be an “angle problem.” However, in considering the direct effects of this possibility, the energy density over the surface or beam time-on-target will not be affected at all, as the beam has negligible attenuation or arrival time difference for small angular variation. One more feasible possibility is the direction of roll-on application for the ablative aluminum tape used for the process. It is impossible to know however, what direction was used for these plates, and the fact that the slope correlated perfectly to the orientation of the more rounded corner of the LSP spot indicates that it is fixed within the laser system, as opposed to the preparation process. The most likely explanation for this sloping tendency, especially considering the consistent rounding of the upper-left corner of LSP spots, is spatially uneven gain or imperfect phase conjugation of the laser system resulting in a non-uniform power density across the laser spot. Ultimately, this effect is a small one, and when applied in a traditional LSP treatment method with overlapping arrays of LSP bursts, the effect will be “flattened out” by the overlapping effects to result in a more uniform surface finish.

To check for differences of surface displacement between the 15 mm and 10 mm aluminum plates, the mean surface displacements of these two plates were plotted

together as seen in Figure 44. There was negligible difference between the two profiles, which indicates adequate damping of the back surface support during the treatment process.

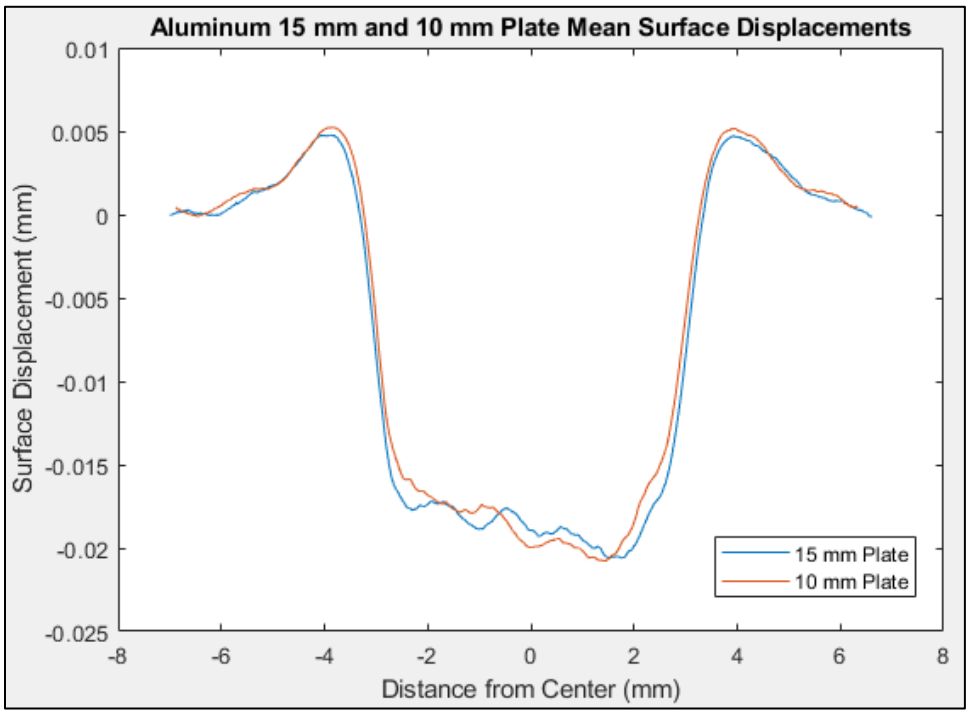

Figure 44: Comparison of surface displacement in 15 mm and 10 mm aluminum plates

After profilometry, the specimens were shipped to Hill Engineering for residual stress measurement by way of hole-drilling. The hole-drilling data consisted of 20 incremental, in-plane x, y, and shear stress measurements for each of 36 holes drilled across all specimens. Twelve of these holes (three per plate) measured the far field for ambient residual stress. The remaining 24 holes were in the center of each LSP spot across the aluminum and titanium plates. Each incremental residual stress measurement for each hole was accompanied by a measurement uncertainty, computed as outlined in

Chapter II. The Hill Engineering report also provided average stress profiles for both untreated and LSP treated locations from each specimen. Across all measurements, the x and y stresses were very close in value and shear stress was negligible. For this reason, only the average principal stress will be the point of discussion for the remainder of this work to remain consistent, and to compare to the single in-plane stress which was output by the axisymmetric model. An example plot of the average residual stress in untreated, and LSP-treated aluminum and titanium plates, as provided in the residual stress report, can be seen in Figure 45. Please note that the report was provided in Imperial units, and the plate naming convention was non-descriptive. The 15 mm and 10 mm aluminum plates are labeled as numbers 82495 and 82496, respectively. The 15 mm titanium plate was processed as two separate plates which are labeled S/N 1 and S/N 2. (The entire Hill Engineering report can be found in Appendix G. Hill Engineering Residual Stress Report **[105]**).

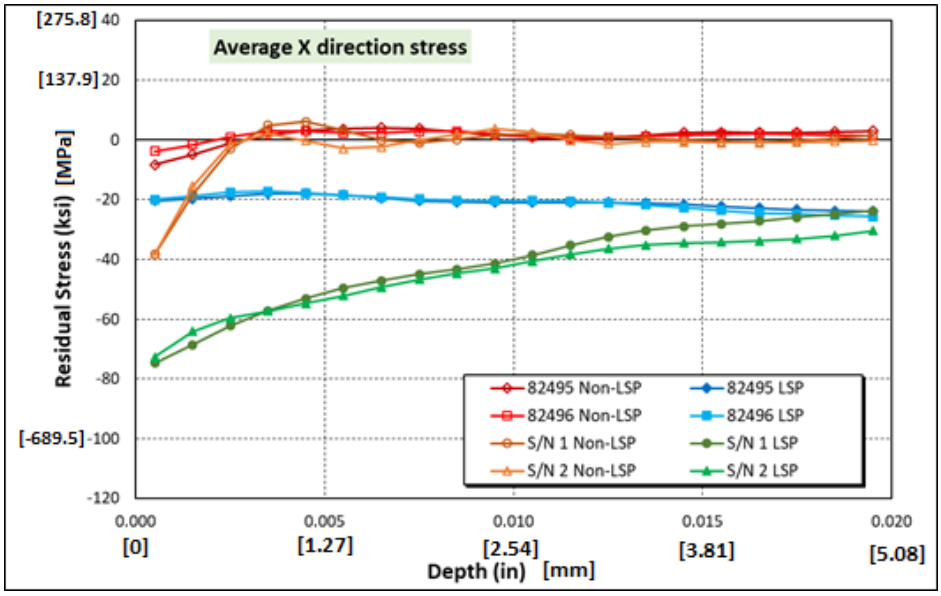

Figure 45: Average untreated and LSP treated stress profiles each plate [105]

To determine how much residual stress was imparted by laser treatment, the ambient residual stress, that is the residual stress measured in the far field and determined to be inherent in the plate before laser treatment, was subtracted from the LSP measured residual stress. This assumption is safe for ambient residual stresses which are very small, however the titanium samples exhibited a significantly higher ambient compressive residual stress near the surface, likely imparted during the plate facing process. Existing compressive stresses of this magnitude might influence the effectiveness of the LSP treatment, resulting in less imparted compressive stress at the surface, and slightly more immediately beneath the surface. This was noted when comparing the effects of the "best-fit" pressure impulse in the titanium FE model to this residual stress data.

In a way similar to the surface displacement data, residual stress data was averaged, and this time bracketed by both measurement uncertainty lines as well as standard deviation lines. This gave an idea of the consistency of data and made a consolidated target for the data-matching operation. The first item of comparison was the residual stress profiles of the 15 mm and 10 mm aluminum plates to check for large differences which may be due to stress wave reflection from back boundary effects. Both of these residual stress profiles exhibited increasing compressive stress into the depth with relatively broad standard deviations from spot to spot. The measurement uncertainty is exceptionally low, indicating good accuracy of measurement, though it broadens at the most extreme measurement depths as a consequence of strain gauge resolution limitations. There was a slight difference in the 10 mm plate vs. 15 mm plate

residual stress profiles between the 0.1 and 0.2 mm depths, however, the difference fell within ~30 MPa which would be considered successful accuracy for compressive residual stress treatment, and was almost entirely encompassed by the standard deviations. The comparison of the thick and thin aluminum plates can be seen in Figure 46. Blue lines correspond to the 10 mm aluminum plate, and red lines to the 15 mm aluminum plate. The darkest line is the mean, and the dashed lines each represent the measurement uncertainty bracket.

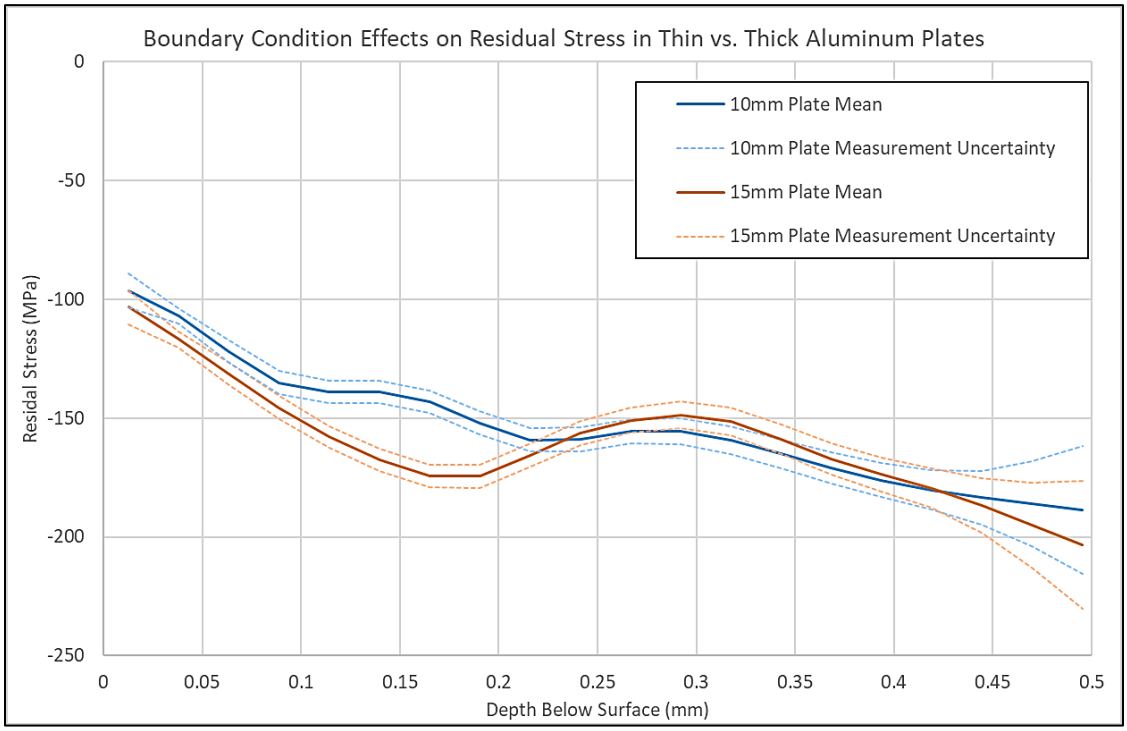

Figure 46: Comparison of residual stress field in 10 mm and 15 mm aluminum plates

Next a comparison can be made between the aluminum and the titanium residual stress fields for the same LSP treatment. Recall that the titanium exhibited significantly less surface displacement than the aluminum, as would be expected for a stiffer, stronger material. One might be led to believe this reduced plastic deformation means that the

imparted residual stress is also less, however, the opposite is true, and in-fact, the residual stress imparted to the titanium is approximately three-fold at its peak, and equal to that of the aluminum at the deepest measured point. The slope of the titanium results also leads one to believe that compressive residual stresses do not extend as deeply into the substrate as in the aluminum plates. Also of note, the standard deviation of stresses within titanium treated spots was quite a bit larger than in aluminum, indicating more variation for a given treatment. This would be an important consideration to the design engineer incorporating LSP into the manufacturing process. The aluminum (in blue) and titanium (in red) residual stress profiles are compared in Figure 47.

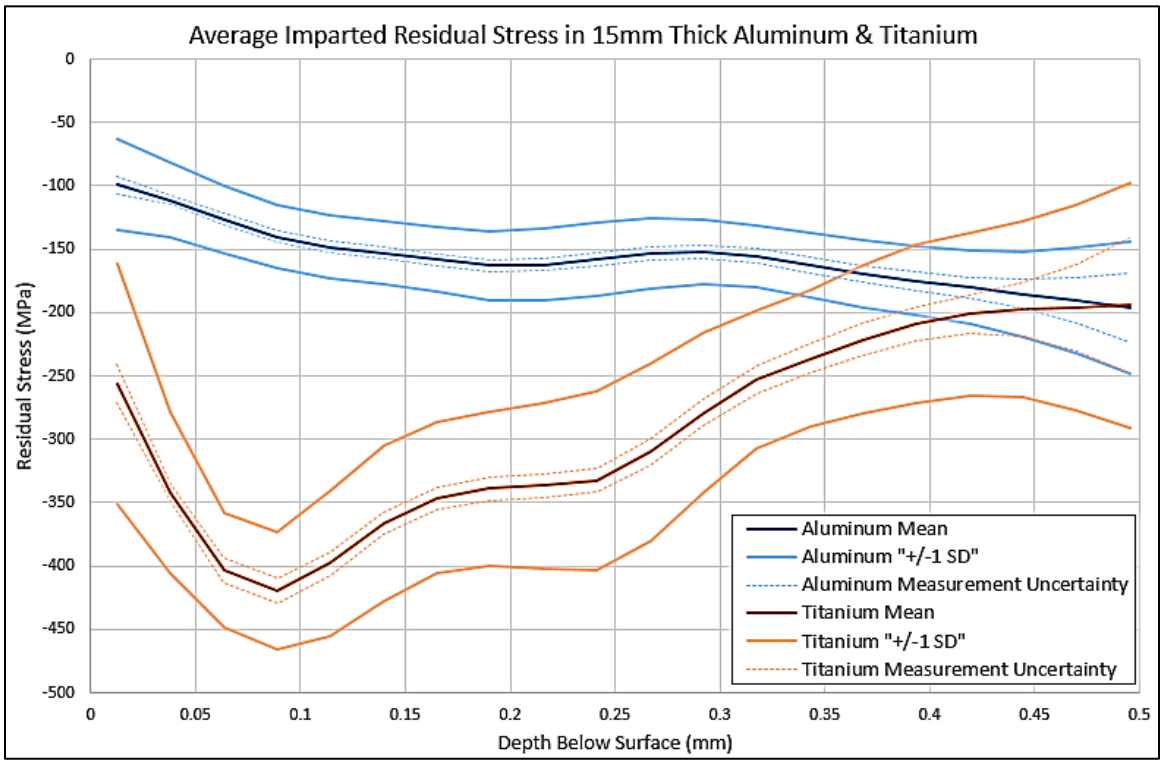

Figure 47: Comparison of residual stress profiles in aluminum and titanium plates

The titanium appears to exhibit the more tensile (less compressive) stress near the surface as has been seen in some models. Recall, however that the ambient residual stress in the titanium plate included a rather substantial compressive stress near the surface (orange lines in Figure 45). Therefore, the apparent tensile trend in the center of the spot should remain suspect, at least nearest the surface, as it would be expected that less compressive residual stress could be imparted into material which already contained a good deal more compressive residual stress initially.

Fully Incorporated Optimization – FE Model Results

The fully incorporated optimization method set out to match the residual stress data from the aluminum plates by determining the best-fit pressure impulse shape. This matching was attempted both with, and without the linear correction factor to account for residual stress differences between the axisymmetric model and 3D. Without the linear correction factor, the data-matching model did a reasonable job at lining up with the measured residual stresses. The comparison of model residual stress results (in blue) and measured residual stress results (in red) can be seen in Figure 48.

As expected, the axisymmetric model predicted a much more tensile residual stress toward the surface, and as a result the rest of the stress profile matched a few MPa below the target data. The stress profile further into the depth, however, fluctuated almost entirely between the measured standard deviation brackets, although seemingly on the lower side. It seems as if, in compensating for the tensile peak near the surface, the optimization algorithm achieved more compressive stresses deeper below the surface. (See Figure 48)

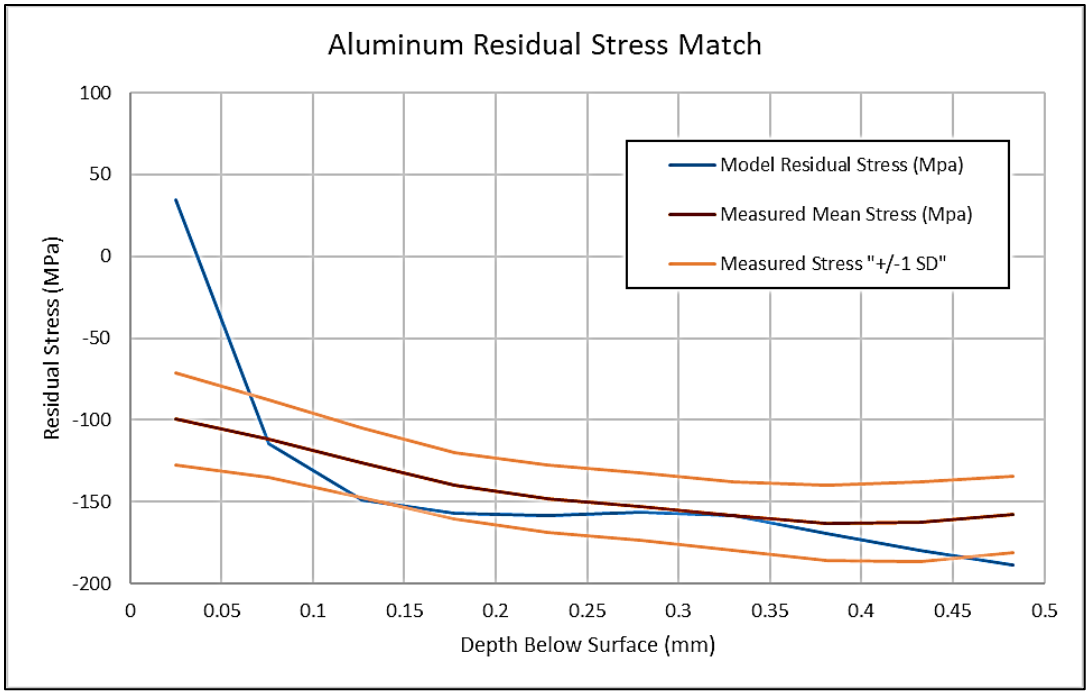

Figure 48: Optimization-matched residual stress field in aluminum plate from uncorrected model

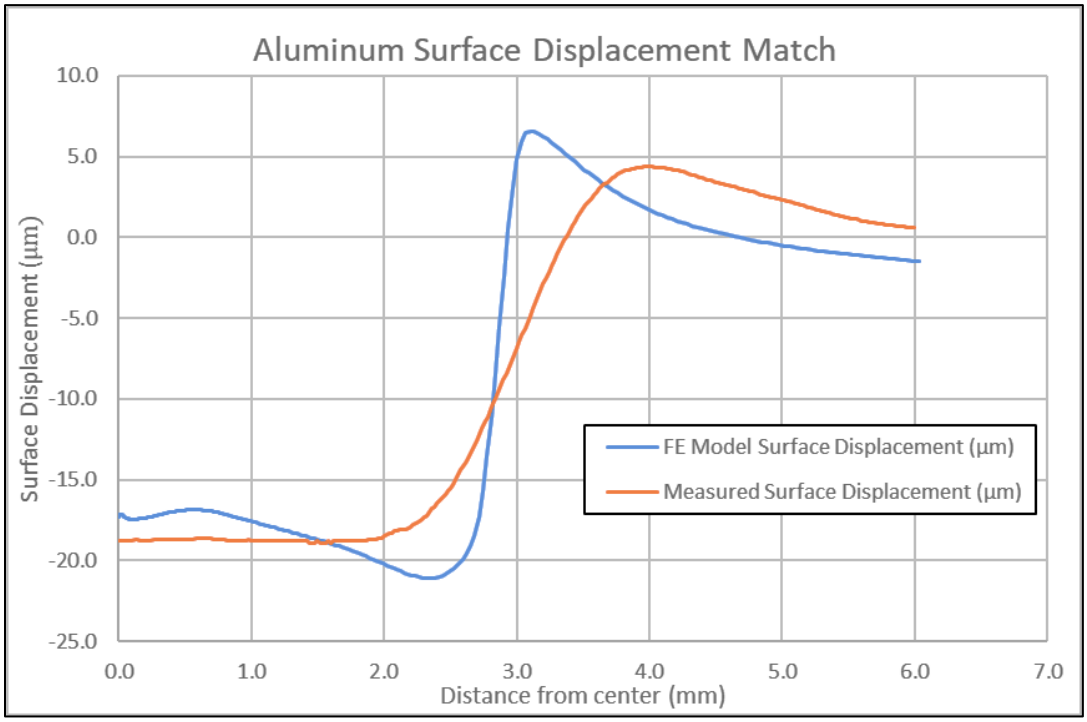

Figure 49: Optimization-matched surface displacement in aluminum plate from uncorrected model

The comparison of FE model and average measured surface displacement can be seen in Figure 49. The magnitudes of the surface displacement are in fairly close agreement with measured values, however, the dimple has a much steeper "sidewall" and a bit more "overshoot" at both sides of this sidewall. It seems the binding to zero pressure at the outer edge of spatial pressure profile is not the most accurate constraint, and perhaps some mechanism to allow some "spilling over" of the pressure to beyond the edge of the laser treated spot would produce a more accurate model. It would be best if the fixed-zero pressure point were further outside the width of the laser spot, and a number of points between the edge of the laser, and the zero point could be given the opportunity to carry some pressure in this transition region. This architecture was given considerable thought, in aspiration to give more flexibility within the optimization space. In pushing the fixed-zero point outward, however, it would be necessary to add at least a couple of points within the transition zone which are added dimensions within the optimization space. This was deemed too expensive to the process, both computationally, and in terms of project scope considering this is a first attempt at such a complex process.

The pressure impulse parameters which were used to produce this pressure profile shape can be seen in Table 11. The optimization matched peak pressure was just over 4.2 GPa, and the associated FWHM peak width was 18 ns with a moderately fast adiabatic cooling dissipation rate. It is possible, as was seen in the proof of concept optimization case, that similar residual stress results could be achieved by a lower pressure, paired with a wider peak width and/or slower pressure dissipation rate. The optimization trial

history for this simulation, however, showed that numerous parameter combinations like this were tested, and yet, the solution converged to the parameters below for the closest match.

Table 11: Optimization-matched pressure impulse parameters from uncorrected model

Pressure Impulse Input Parameter	Optimization Match Value
Peak Pressure (GPa)	4.2031
FWHM Peak Width (ns)	18.1
Adiabatic Cooling & Lateral Dissipation Rate	.91591
Spatial Pressure Point P1	0.9739
Spatial Pressure Point P2	0.9597
Spatial Pressure Point P3	0.9876
Spatial Pressure Point P4	1.0
Spatial Pressure Point P5	0.9226

The spatial profile was very nearly a plateau, with just a slight dip in the center and a lightly rounded corner at the edge of the laser spot (see Figure 50). Interestingly, this profile is not far removed from the work of Hasser et al. [57] as in Figure 4(a) from Chapter I, in which the peak pressure is actually produced near the outside of the laser spot, and a diminished pressure is seen toward the middle. The profile established here is unlike that previous work in that it is first derivative continuous, making it a more feasible match to what might occur in the actual LSP event.

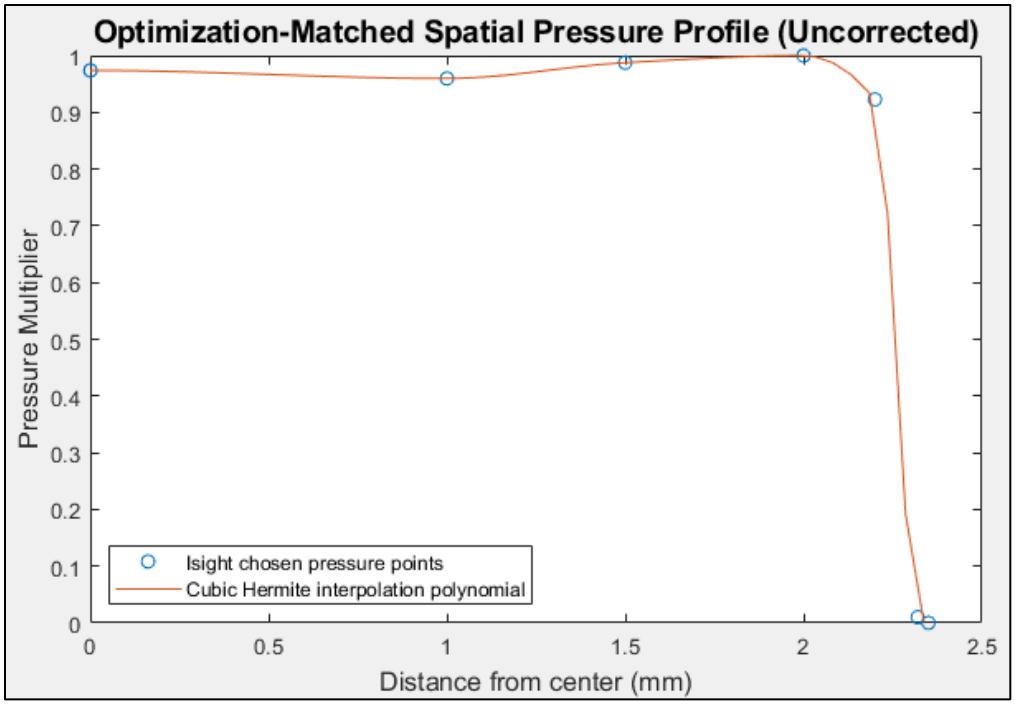

Figure 50: Optimization-matched spatial pressure profile from uncorrected model

Next, the optimization process was run again with all the same parameters, but the residual stress field was corrected with the linear regression equations to account for the near-surface tensile behavior of the axisymmetric model. In this case, FE model residual stress results were modified by these correction equations before being compared to experimental data, and by extension before being inserted into the objective function. The results of this trial showed slight improvements in the matching in aluminum.

The residual stresses can be seen in Figure 51. The model residual stress still exhibited slightly more tensile behavior at the surface, but was not as prominent in this corrected model. Further, the residual stresses below the surface fit well between the standard deviation ranges of measured data. The upward trend of model residual stresses

at the deepest measured points might indicate that the overall depth of residual stresses is less than in the previous attempts, but for the measured depths, it still lies within an acceptable range.

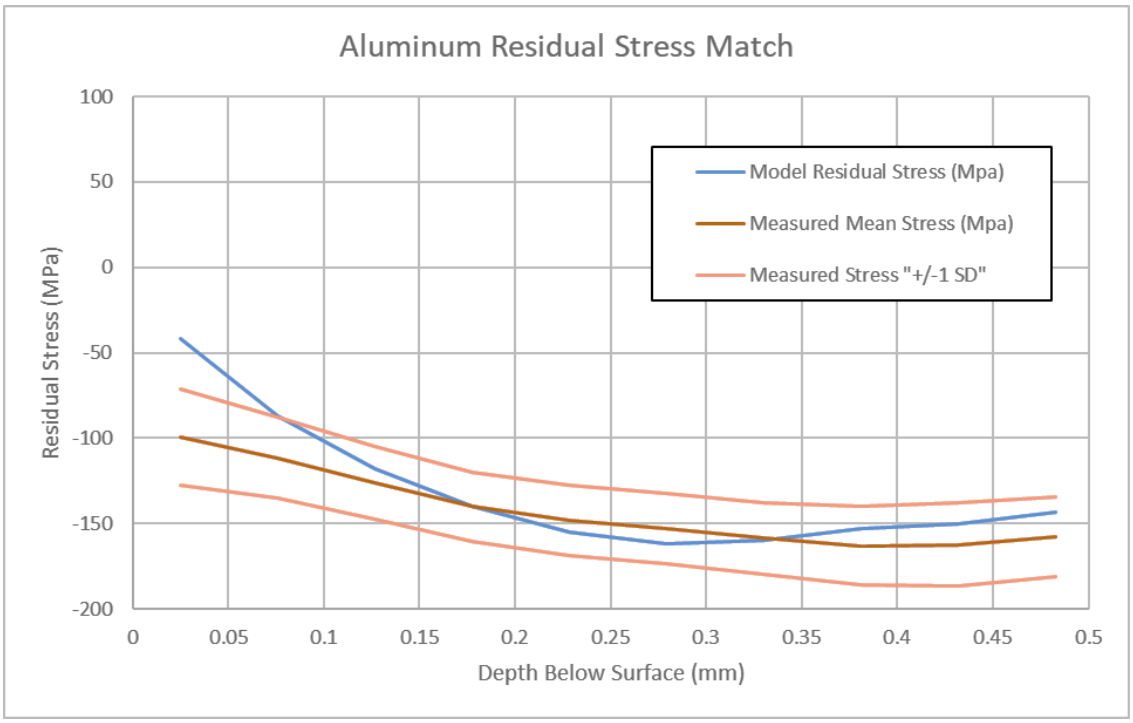

Figure 51: Optimization-matched residual stress field in aluminum plate from corrected model

The surface displacement results exhibited the same problems as noted in the previous trial, and were also not significantly different, although they were slightly closer to measured data in a few areas. These results can be seen in Figure 52.

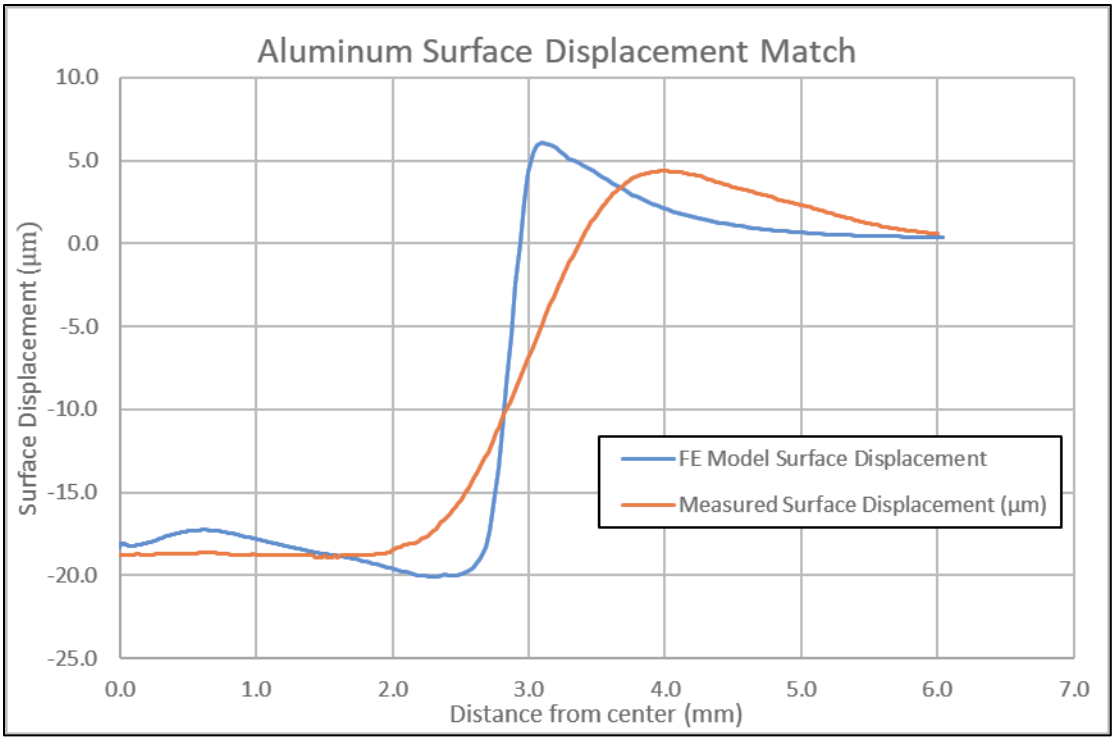

Figure 52: Optimization-matched surface displacement in aluminum plate from corrected model

The pressure impulse parameters from the corrected model can be seen in Table 12. The peak pressure was slightly less compared to the uncorrected model, and the peak width was somewhat wider with a marginally slower dissipation rate. The spatial pressure points resulted in a shape similar to the uncorrected model.

Table 12: Optimization-matched pressure impulse parameters from corrected model

Pressure Impulse Input Parameter	Optimization Match Value
Peak Pressure (GPa)	4.1642
FWHM Peak Width (ns)	18.4
Adiabatic Cooling & Lateral Dissipation Rate	.91391
Spatial Pressure Point P1	0.9648
Spatial Pressure Point P2	0.9696
Spatial Pressure Point P3	0.9952
Spatial Pressure Point P4	1.0
Spatial Pressure Point P5	0.9519

The matched spatial pressure profile from the residual stress corrected trial can be seen in Figure 53. It is not significantly different from the uncorrected trial, but does have a slightly more abrupt drop-off at the outer edge of the laser spot.

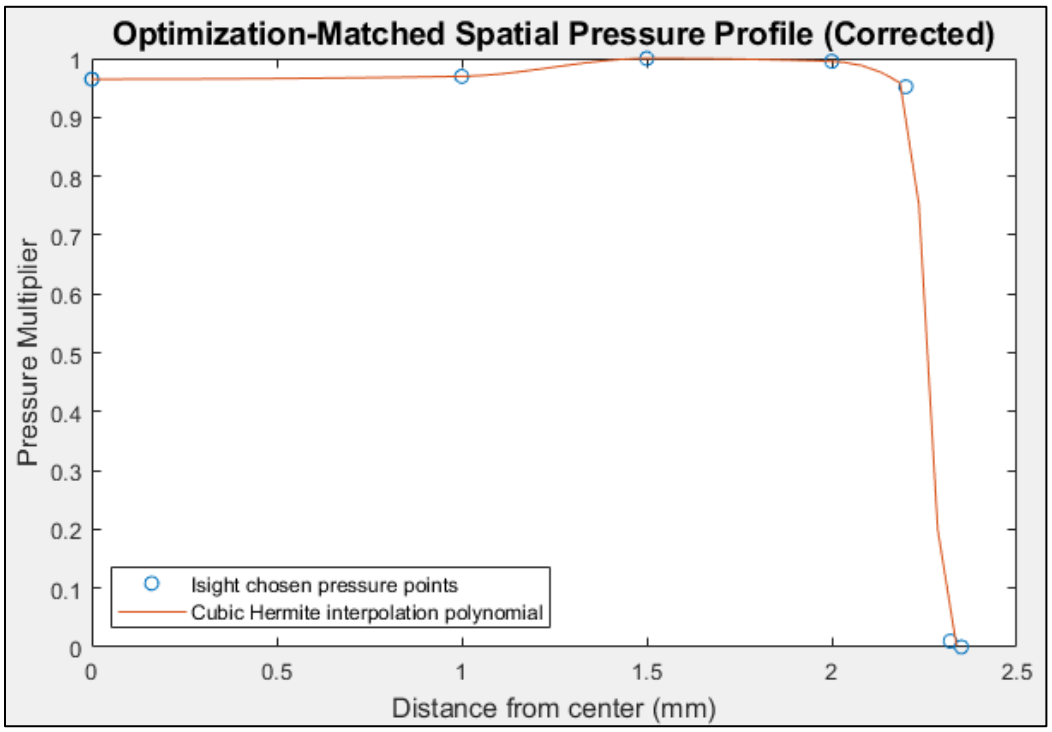

Figure 53: Optimization-matched spatial pressure profile from corrected model

Without yet considering how these pressure profiles translate to the titanium model for validation, the linear correction factor on the residual stress data did appear to improve the quality of data-match slightly.

Validation of Best-Fit Impulse on Titanium Material Model

The final step of the current work was to validate this best-fit pressure impulse on the titanium model. Recall that to transfer the best-fit pressure impulse, it must be scaled by the root of the ratio of the shock impedance of the materials as outlined in the previous

chapter. This scaling resulted in a peak pressure of 5.3224 GPa, which was then applied, with all other pressure impulse parameters the same, to the titanium model. The resultant residual stress profile can be seen in Figure 54, where the blue line is the simulation resultant residual stress profile in titanium, and the red line is the measured data.

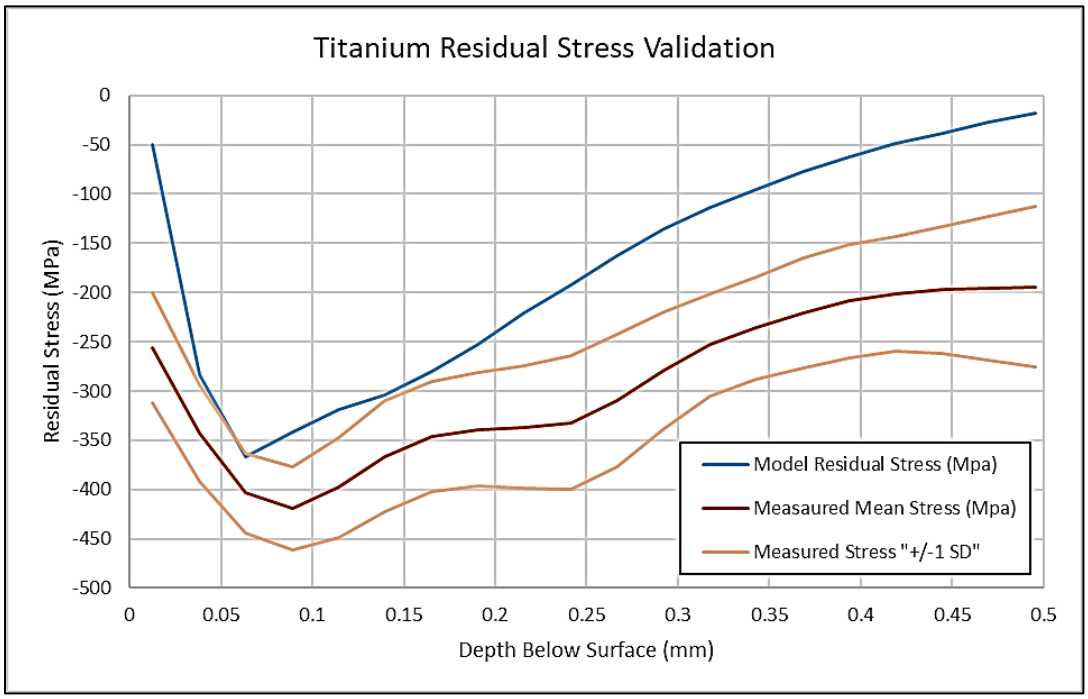

Figure 54: Residual stress from uncorrected best-fit pressure impulse applied to titanium

The uncorrected model residual stress profile does not perfectly match collected data, though it followed a very similar contour, which is notably different than that of the aluminum. The stresses are consistently less compressive throughout the entire depth. The residual stress results did, however exhibit the expected tensile trends near the surface, though these strayed less from experimental data than the tensile spike in aluminum.

This underestimation of the compressive residual stress could be the result of many things. First, the theoretical work of Fabbro [92] from which the pressure scale multiplier was derived was one-dimensional, perhaps oversimplifying the problem too much to account for unknown 3D effects. It is also possible that the material properties of the materials used differed from published material properties in one or both of the test materials. It is not expected that the aluminum material properties would have much variation as the manufacturing process for that alloy is quite consistent, though some small variation in modulus or yield strength would be feasible. The material properties for titanium, however are very dependent on temper. The mill-annealing process is designed to reduce this variance, however there could still be some differences. It would have been ideal, to determine the Johnson-Cook material parameters of the plate from which the titanium specimens were taken, and this was planned, and is in fact still under contract to be accomplished for other work. However, the timeline for that contract slipped out of alignment with the timeline of the current work, and previously published values had to suffice. If, for example, the aluminum modulus was slightly stiffer, and yield strength was slightly higher, and the opposite was true of titanium, this combination of variance would indeed lead to the underestimated titanium residual stress exhibited here. Similarly one of the Johnson-Cook parameters followed a similar trend, the same result could be achieved. Ideally a sensitivity analysis on material properties could be accomplished to test this theory but it was deemed beyond the feasible scope of the current work. Finally, in the flow of the current work, the aluminum, and titanium specimens were laser treated more than a month apart. While it should be expected that

identical laser treatment could be produced at any given time. It is possible that some variation in the LSP process resulted in a slightly more powerful treatment of the titanium. This could be anything from a thicker inertial water layer containing the pressure, to slight variations in the focus or power output of the laser, even if within the accepted tolerances put forth for LSP standards.

The surface displacement of the titanium in response to the best-fit pressure impulse can be seen in Figure 55.

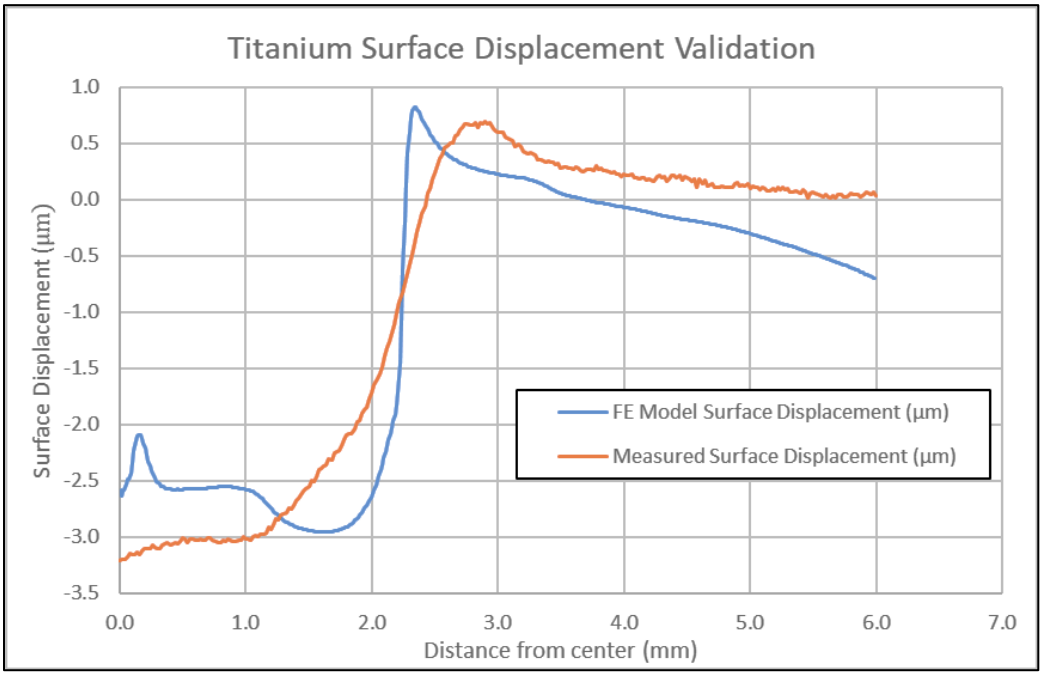

Figure 55: Surface displacement from uncorrected best-fit pressure impulse applied to titanium

The surface displacement in the titanium model exhibits the same overly-steep sidewalls as were seen in aluminum. The magnitudes of the high and low points were within relatively close range of measured data. Most interestingly, however, was the more pronounced trough-like dip at the bottom of the LSP dimple sidewall, and an

unusual bump very near the center of the treated spot, which would in-fact be a ring within the dimple. These seem like the kinds of formations which might arise from a liquid medium impacted by a drip, and are perhaps formed by similar mechanisms. The model was rerun with a longer total time to ensure that this bump was not a wave caught traveling through the model, however the results were the same.

Next the pressure impulse from the corrected model was applied to titanium for impulse validation. These results were similar, but slightly improved. First, the residual stress was still significantly less compressive than measured, but actually reached within one standard deviation of the average measured residual stress around a depth of 0.15 mm. The residual stress results can be seen in Figure 56.

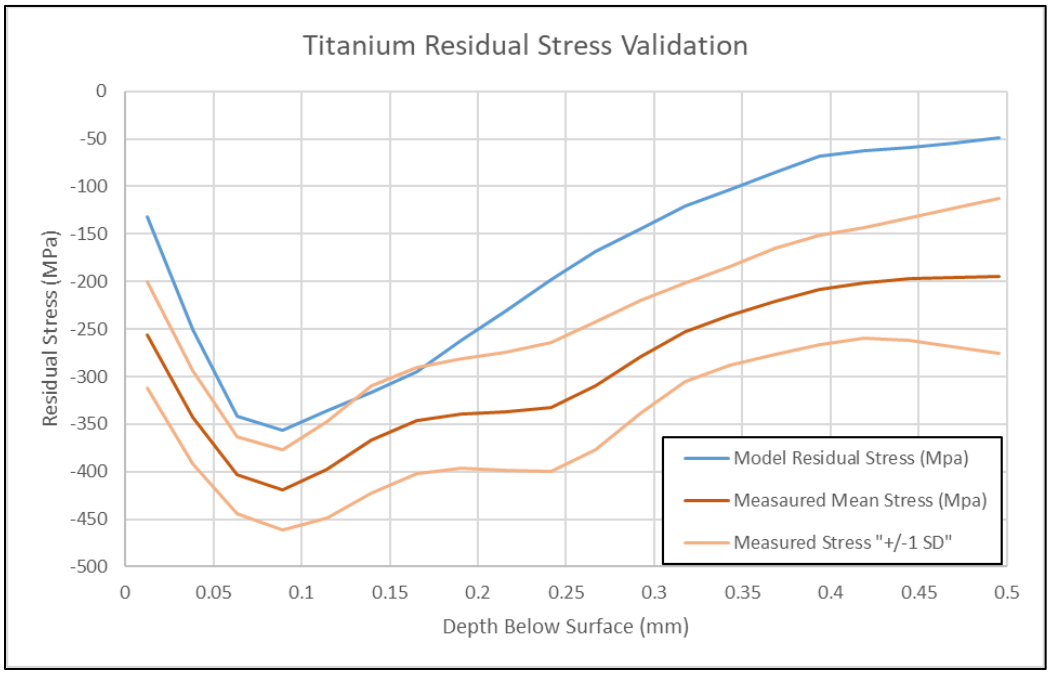

Figure 56: Residual stress results of corrected best-fit pressure impulse applied to titanium

The surface displacement in titanium showed negligible difference between the corrected and uncorrected models.

IV. Summary and Conclusions

Summary

The current work set out to test a novel method for LSP pressure impulse shape determination in both time and space via optimization methods. The goal was to find the best-fit impulse shape to match empirical residual stress and surface displacement data and bring about a method by which pressure impulse shapes could be "cataloged" for various laser settings to be applied to FE modeling efforts on demand. The current work sought to address a major shortfall in the LSP modeling field in that pressure impulse shapes have not ever directly been measured and thus are always assumed, sometimes poorly. This results in inaccurate residual stress predictions which are not yet reliable enough to incorporate in engineering solutions without validation by full-scale, or at least by representative component testing. Improved pressure impulse models could preclude these expensive tests.

A methodical review of literature was conducted to determine the state of LSP research and modeling to date. The documented material improvements brought about by LSP treatment are very much beneficial and able to be tailored to specific material or structural needs. These include surface hardness, surface finish, and compressive residual stresses. Most notably, the improved resistance to fatigue and crack growth are of high value to structural metals in particular. FE modeling of LSP has a number of best-practices which are fairly consistent across the field. Johnson-Cook viscoplasticity is the most common foundational material model in use of late. The use of an EOS is also common, though less consistent, and apparently dependent on LSP settings and

expected peak pressures. Numerous software applications are common in the field. Most commercially available FE software programs are capable of handling this type of modeling. High performance computing is occasionally used to handle large, single explicit step models, especially if the LSP burst is to be repeated numerous times. Less computational power is required to carry out an explicit kinetic phase, implicit equilibrium phase model, however, this is more complex to set up for numerous model configurations. Explicit modeling is the most common at this time. Most notably, there is a large variety of examples of assumed pressure impulse shapes in both time and space. The field has not seemed to settle on one specific standard. The SRT pressure impulse shape in time is the most commonly used, however, there are still many variations of this type. Spatially, there is no widely used shape. There have been many forms of different partial Gaussian profiles, but still a significant number of other assumed shapes. It is this lack of measured or determined pressure impulse shape which was of most interest for the present work. Further, there are a number of measurable artifacts which come about from LSP treatments. Surface hardness and finish do not change enough to measure small differences between LSP settings. Surface displacement, and residual stress field, however, are easily measured, and vary greatly with different LSP settings making them the ideal artifacts to attempt to match.

Finite element models were developed and tested, including verification of a Johnson-Cook viscoplasticity and Mie-Grüneisen EOS material model. Initial models showed the effectiveness of the Johnson-Cook viscoplasticity model, but developed residual stress and surface displacement anomalies at higher pressure, indicating the need

for hard shock handling. This was accomplished via the Mie-Grüneisen EOS. A full model work-energy analysis was conducted and qualitatively matched published work. Complete validation was not accomplished due to insufficient specific model settings to which a comparison could be made.

A model type study was conducted to test the likenesses of various 2D and 3D representations of the LSP process. A full 3D (square), quarter-symmetric 3D (square), axisymmetric, and modified axisymmetric model were compared under the same assumed pressure impulse to determine how residual stress results varied across these model types. The quarter-symmetric 3D model most closely matched the full 3D model. The axisymmetric model produced a slightly more tensile residual stress near the laser treated surface due to a stress-focusing effect. Modified axisymmetric models with both wider treated spots, as well as higher peak pressures were tested to better match the total applied work of the 3D square spot. Ultimately, the original axisymmetric model was still more accurate than the modified forms. To the prospect of thousands of iterations, the efficiency of a 2D model was deemed more important than perfect accuracy, and the axisymmetric model was utilized for the remainder of the work by incorporating pointwise linear correction factors which would assimilate axisymmetric residual stress results to their equivalent 3D results. A comparison of multiple LSP model types was something not found in any prior work to date.

Residual stress and surface displacement data was collected and averaged for numerous single LSP spots. Spots were treated via 16 Joule neodymium-doped glass laser with a pulse duration of 18 ns over a 4.7 mm wide square spot resulting in an energy

density of 4 GW/cm^2. Eight spots were applied to each of three plates. Two plates of 2024-T351 aluminum were tested (one 10 mm and one 15 mm thick). One plate (split in two) of 15 mm thick mill-annealed titanium was also tested. Surface displacement was measured via optical profilometer and averaged for each of the plates. Residual stress was measured via hole-drilling in both the far field (ambient) and in the center of each LSP spot (treated) to determine imparted residual stress. Surface displacement in the aluminum was greater than that of titanium, however the magnitude of compressive residual stress imparted into the titanium was greater, though not as deep.

A Hooke-Jeeves optimization algorithm was built to modify pressure impulse shape in both time and space within a 5-dimensional optimization space to attempt to match FE model residual stress and surface displacement results to the empirically-collected data. A simplified proof of concept model was built within a discretized optimization space to attempt to match a known pressure input, and did so in under 100 iterations, and to within less than 7.1% error, though non-uniquely. Over continuous optimization space, the model matched results to within 4.5% maximum error. These modeling methods were then transferred to a fully continuous optimization space, built to better reflect the LSP process used on the measured specimens. This full simulation was used to determine the best-fit pressure impulse shape by matching the results obtained in 2024 aluminum. Surface displacement results showed some inaccuracies, particularly in the region of transition between treated and untreated material. The residual stress, however matched, generally to within ~25 MPa, and slightly better in the linearly

corrected axisymmetric model. Most residual stress measurements were within the one standard deviation of the measured average.

This best-fit impulse shape was then transferred to a titanium FE model to attempt to validate this pressure impulse shape. This was done by scaling up the peak pressure to account for a higher shock impedance of titanium. When applied to titanium, the residual stress and surface displacement did not match as accurately. Residual stress was under-predicted by a significant amount, though slightly less so in the linear corrected model.

Conclusions

A few key conclusions can be drawn from this work. First, the pairing of the Johnson-Cook viscoplasticity and Mie-Grüneisen EOS produces a material model which should be considered the standard in the field of LSP explicit modeling if it was not already so. Hydrocodes might be able to more accurately model certain material situations, particularly when damage is prominent, however, FE codes which allow for Johnson-Cook and Mie-Grüneisen bring sufficient material model fidelity for the LSP process within reach of design engineers which are often less familiar with in-depth codes. The empirically based Johnson-Cook model handles the deviatoric viscoplasticity for most strain rates. The addition of the Mie-Grüneisen EOS allows the handling of a hard shock by linking material density to shock and particle velocity for very high hydrostatic pressure circumstances. The combination of these two into an explicit simulation is ideal for LSP modeling.

Next, the substitution of a 2D axisymmetric model to approximate a square LSP spot provides sufficiently accurate results to speed up model run time where it is

necessary to dramatically reduce CPU-hours. Modifications to the axisymmetric model to better match energy input are not helpful, but rather a linear adjustment can be implemented to improve the prediction. By using this pointwise linear adjustment, results from an axisymmetric model can be used to determine equivalent 3D model results, fit to within R^2 of 0.96.

More notably, the method of using an optimization algorithm to match FE model results to a set target can successfully be employed to achieve an accurate match. This method was also successfully utilized to find a pressure impulse shape which resulted in an FE model match of empirical residual stress data to within 5%. As to whether this optimization matched pressure impulse shape can be transported to a different FE model, specifically one with different material properties, that remains inconclusive. Initial results of transferred pressure impulse in titanium were less accurate. The results show promise in that the shape of the residual stress curve very closely matched. The magnitude, however, has room for improvement. This could be a consequence of simplifying assumptions made in this fledgling initial study, or more likely variance of material model constants which could be fixed in future by matched material testing to determine more precise model constants. This is where the most room for future work can be found, as the initial model has showed some promise worth pursuing.

Suggested Future Work

This work sets forth a foundation on which similar processes could be used within the field of LSP modeling to continue to improve FE model prediction of residual stresses. Initial pressure impulse matching shows promise which could be capitalized

upon by a few key improvements. First, it would be of high value to employ cluster computing to execute a fully 3D model incorporated into the optimization algorithm. This would require increased pressure impulse shape parameters to handle both corners of the laser spot as well as anisotropic pressure distribution, and would thus create a much larger optimization space which might require improve optimization algorithms to efficiently match empirical results.

Second, it might be necessary to empirically determine the material properties of the exact material sample to which the pressure impulse is matched. This would be a big hurdle for the employment of the method in common engineering application, but if a single, well characterized material could be used for pressure impulse determination, the design application of LSP to common materials would still be significantly improved. Further, material characterization of an alloy for testing might still, in some cases such as the F-22, be less expensive than full-scale testing for LSP validation.

Contributions

Within the present work, the analysis of single LSP spot displacement and residual stress data is the first of this magnitude, and among the first of its kind, particularly in collecting a statistically significant sample size. Eight identical LSP bursts were applied to each of three specimens consisting of two materials and their associated residual stress and surface displacements were measured. This data-set is of high value to the research community, and the possible analysis conducted in the present work has only touched the surface of its utility. Efforts will be made to make this set of data available to the research community for future work.

The method of using an optimization algorithm to attempt to determine pressure impulse shape by data-matching of LSP artifacts was entirely novel to this field. Optimization has been used to a small degree to optimize results for a given LSP treatment or optimize LSP settings for a desired result, however, the reverse engineering of the pressure impulse shape by attempted data-matching has never been attempted (or at least published).

Finally, the validation of an optimization-matched pressure impulse shape in a second material was the first attempted. While the results of this validation may be been less than perfect, they show promise that this method could be improved and capitalized upon to improve LSP modeling accuracy and streamline its incorporation into engineering design at every level.

Appendix A. Abaqus Finite Element Code Details [88]

1. Introduction

Abaqus is a suite of powerful engineering simulation programs, based on the finite element method, that can solve problems ranging from relatively simple linear analyses to the most challenging nonlinear simulations. Abaqus contains an extensive library of elements that can model virtually any geometry. It has an equally extensive list of material models that can simulate the behavior of most typical engineering materials including metals, rubber, polymers, composites, reinforced concrete, crushable and resilient foams, and geotechnical materials such as soils and rock. Designed as a general-purpose simulation tool, Abaqus can be used to study more than just structural (stress/displacement) problems. It can simulate problems in such diverse areas as heat transfer, mass diffusion, thermal management of electrical components (coupled thermal-electrical analyses), acoustics, soil mechanics (coupled pore fluid-stress analyses), piezoelectric analysis, electromagnetic analysis, and fluid dynamics.

Abaqus offers a wide range of capabilities for simulation of linear and nonlinear applications. Problems with multiple components are modeled by associating the geometry defining each component with the appropriate material models and specifying component interactions. In a nonlinear analysis Abaqus automatically chooses appropriate load increments and convergence tolerances and continually adjusts them during the analysis to ensure that an accurate solution is obtained efficiently.

1.1 The Abaqus products

Abaqus consists of three main analysis products—Abaqus/Standard, Abaqus/Explicit, and Abaqus/CFD. Several add-on analysis options are available to further extend the capabilities of Abaqus/Standard and Abaqus/Explicit. The Abaqus/Aqua option works with Abaqus/Standard and Abaqus/Explicit. The Abaqus/Design and Abaqus/AMS options work with Abaqus/Standard. Abaqus/Foundation is an optional subset of Abaqus/Standard. Abaqus/CAE is the complete Abaqus environment that includes capabilities for creating Abaqus models, interactively submitting and monitoring Abaqus jobs, and evaluating results. Abaqus/Viewer is a subset of Abaqus/CAE that includes just the postprocessing functionality. Abaqus also provides translators that convert geometry from third-party CAD systems to models for Abaqus/CAE, convert entities from third-party preprocessors to input for Abaqus analyses, and that convert output from Abaqus analyses to entities for third-party postprocessors. The relationship between these products is shown in Figure 1–1.

Abaqus/Standard

Abaqus/Standard is a general-purpose analysis product that can solve a wide range of linear and nonlinear problems involving the static, dynamic, thermal, electrical, and electromagnetic response of components. This product is discussed in detail in this guide. Abaqus/Standard solves a system of equations implicitly at each solution "increment." In contrast, Abaqus/Explicit marches a solution forward through time in small time increments without solving a coupled system of equations at each increment (or even forming a global stiffness matrix).

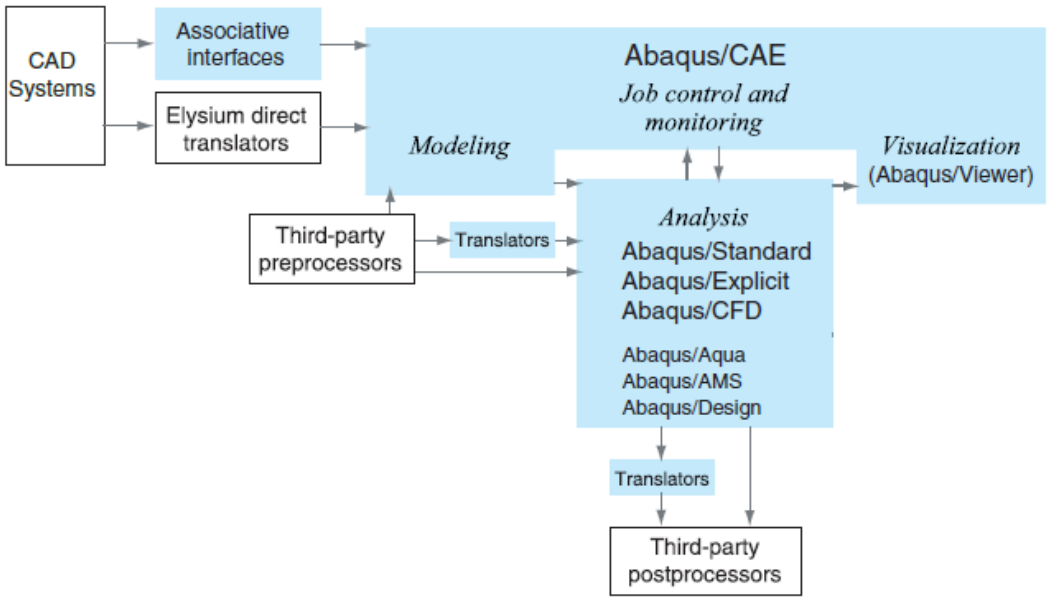

Figure 1–1 Abaqus products.

Abaqus/Explicit

Abaqus/Explicit is a special-purpose analysis product that uses an explicit dynamic finite element formulation. It is suitable for modeling brief, transient dynamic events, such as impact and blast problems, and is also very efficient for highly nonlinear problems involving changing contact conditions, such as forming simulations. Abaqus/Explicit is discussed in detail in this guide.

Abaqus/CFD

Abaqus/CFD is a computational fluid dynamics analysis product. It can solve a broad class of incompressible flow problems including laminar and turbulent flow, thermal convective flow, and deforming mesh problems. Abaqus/CFD is discussed in this guide.

Abaqus/CAE

Abaqus/CAE (Complete Abaqus Environment) is an interactive, graphical environment for Abaqus. It allows models to be created quickly and easily by producing or importing the geometry of the structure to be analyzed and decomposing the geometry into meshable regions. Physical and material properties can be assigned to the geometry, together with loads and boundary conditions. Abaqus/CAE contains very powerful options to mesh the geometry and to verify the resulting analysis model. Once the model is complete, Abaqus/CAE can submit, monitor, and control the

analysis jobs. The Visualization module can then be used to interpret the results. Abaqus/CAE is discussed in this guide.

Abaqus/Viewer

Abaqus/Viewer is a subset of Abaqus/CAE that contains only the postprocessing capabilities of the Visualization module. The discussions of the Visualization module in this guide apply equally to Abaqus/Viewer.

Abaqus/Aqua

Abaqus/Aqua is a set of optional capabilities that can be added to Abaqus/Standard and Abaqus/Explicit. It is intended for the simulation of offshore structures, such as oil platforms. Some of the optional capabilities include the effects of wave and wind loading and buoyancy. Abaqus/Aqua is not discussed in this guide.

Abaqus/Design

Abaqus/Design is a set of optional capabilities that can be added to Abaqus/Standard to perform design sensitivity calculations. Abaqus/Design is not discussed in this guide.

Abaqus/AMS

Abaqus/AMS is an optional capability that can be added to Abaqus/Standard. It uses the automatic multi-level substructuring (AMS) eigensolver during a natural frequency extraction. Abaqus/AMS is not discussed in this guide.

Abaqus/Foundation

Abaqus/Foundation offers more efficient access to the linear static and dynamic analysis functionality in Abaqus/Standard. Abaqus/Foundation is not discussed in this guide.

Geometry translators

Abaqus provides the following translators for converting geometry from third-party CAD systems to parts and assemblies for Abaqus/CAE:

- The SIMULIA Associative Interface for Abaqus/CAE creates a link between CATIA V6 and Abaqus/CAE that allows you to transfer model data and propagate design changes from CATIA V6 to Abaqus/CAE.
- The CATIA V5 Associative Interface creates a link between CATIA V5 and Abaqus/CAE that allows you to transfer model data and propagate design changes from CATIA V5 to Abaqus/CAE.
- The SolidWorks Associative Interface creates a link between SOLIDWORKS and Abaqus/CAE that allows you to transfer model data and propagate design changes from SOLIDWORKS to Abaqus/CAE.

- The Pro/ENGINEER Associative Interface creates a link between Pro/ENGINEER and Abaqus/CAE that allows you to transfer model data and propagate design changes between Pro/ENGINEER and Abaqus/CAE.
- The Geometry Translator for CATIA V4 allows you to import the geometry of CATIA V4-format parts and assemblies directly into Abaqus/CAE.
- The Geometry Translator for Parasolid allows you to import the geometry of Parasolid-format parts and assemblies directly into Abaqus/CAE.

In addition, the Abaqus/CAE Associative Interface for NX creates a link between NX and Abaqus/CAE that allows you to transfer model data and propagate design changes between NX and Abaqus/CAE. The Abaqus/CAE Associative Interface for NX can be purchased and downloaded from Elysium Inc. (www.elysiuminc.com).

The geometry translators are not discussed in this guide.

Translator utilities

Abaqus provides the following translators for converting entities from third-party preprocessors to input for Abaqus analyses or for converting output from Abaqus analyses to entities for third-party postprocessors:

- **abaqus fromansys** translates an ANSYS input file to an Abaqus input file.
- **abaqus fromdyna** translates an LS-DYNA keyword file to an Abaqus input file.
- **abaqus fromnastran** translates a Nastran bulk data file to an Abaqus input file.
- **abaqus frompamcrash** translates a PAM-CRASH input file into an Abaqus input file.
- **abaqus fromradioss** translates a RADIOSS input file into an Abaqus input file.
- **abaqus adams** translates the results in an Abaqus SIM database file into an MSC.ADAMS modal neutral (`.mnf`) file, the format required by ADAMS/Flex.
- **abaqus moldflow** translates finite element model information from a Moldflow analysis into a partial Abaqus input file.
- **abaqus toexcite** translates data in an Abaqus substructure SIM database to an EXCITE flexible body interface (`.exb`) file.
- **abaqus tonastran** translates an Abaqus input file to Nastran bulk data file format.
- **abaqus toOutput2** translates an Abaqus output database file to the Nastran Output2 file format.
- **abaqus tosimpack** translates data in an Abaqus substructure SIM database to a SIMPACK flexible body interface (`.fbi`) file.
- **abaqus tozaero** enables the exchange of aeroelastic data between Abaqus and ZAERO.

The translator utilities are not discussed in this guide.

Appendix B. Isight Optimization Code Details [94]

What is Isight?

You can use Isight to model multi-step simulation and engineering data analysis processes, and to automate execution of these processes. Isight repeatedly executes the process under control of a design driver (e.g., DOE component, Optimization component) to explore the design space.

The Design Gateway

The Isight Design Gateway is shown below.

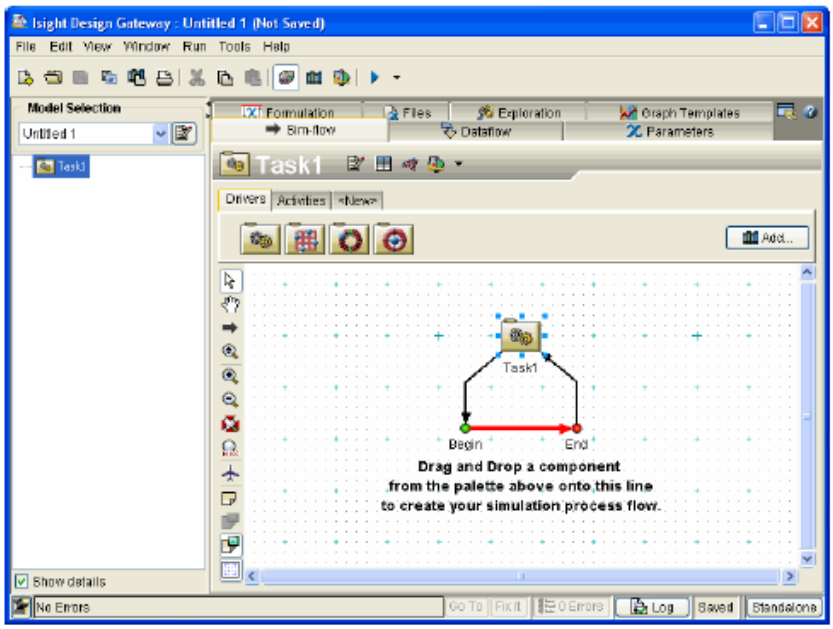

This interface is the main Isight interface. It allows you to create models, manipulate components, and perform other functions associated with model design and development.

This interface allows you to perform the following basic actions:

- You can drag-and-drop components from the component tabs to the **Sim-flow** tab to create a model simulation process flow. The component tabs (Drivers, Activities, etc.) allow you to arrange your components in a way that is convenient for you. You can even create custom tabs using the <**New**> tab.
- Once added to the simulation process flow, you can double-click any component to access its editor.
- The menu and toolbar buttons allow access to additional features (Publish, Preferences, Run, etc.) as well as other interfaces (Runtime Gateway, Generator, etc.).

For more information on this interface Design Gateway, refer to the *Isight User's Guide*.

The Runtime Gateway

The Isight Runtime Gateway is shown below.

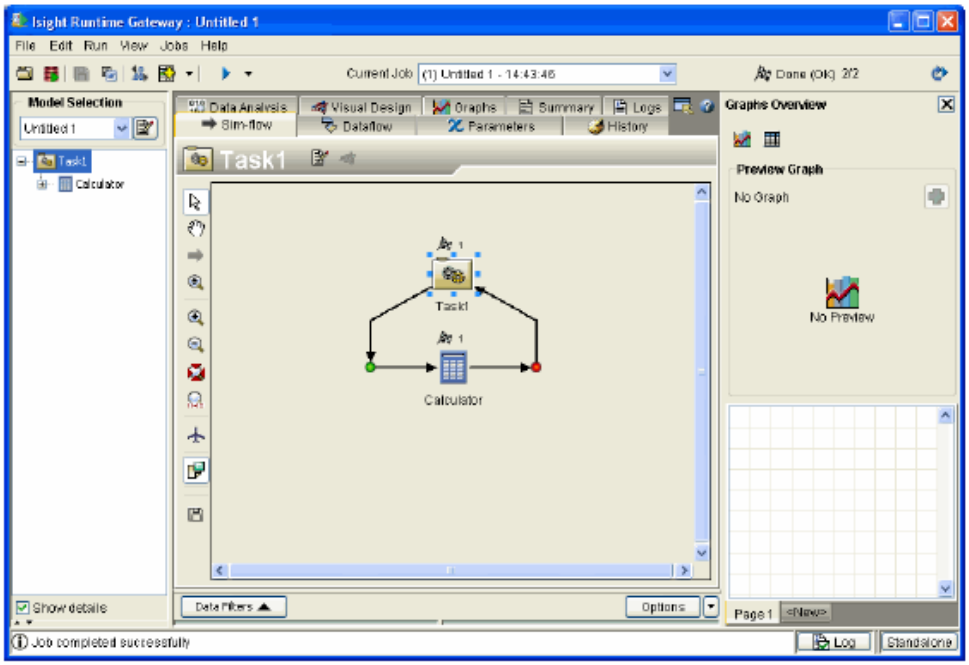

This interface differs from the Design Gateway because you can control execution of a model and view results, but you have limited access to the components and simulation process flow. You can create graphs and tables, view parameter information, create approximations, access data analysis tools, and resubmit models for execution on the Runtime Gateway. The following main features are available:

- **Sim-flow** tab. Allows you to view the overall model simulation process flow and access component editors.
- **Parameters** tab and **History** tab. Allow you to view results information for individual components.
- **Graphs** tab and **Data Analysis** tab. Provides access to graphs, tables, and postprocessing tools for viewing results.
- **Visual Design** tab. Allows you to create and view approximations.

- **Logs** tab. Provides execution information and may be helpful when errors occur during execution.
- **Run** menu. Allows you to execute the model simulation process flow repeatedly, without having to return to the Design Gateway.

Using Postprocessing Tools

While some of the postprocessing tools are discussed in the remaining chapters, there are many other tools that can assist you in viewing and analyzing results. These include Problem Formulation (run-time grading) and parameter filtering. Proceed to one of the following sections:

- "Understanding Problem Formulation (Run-time Grading)" on this page
- "Understanding Parameter Filtering," on page 40

Understanding Problem Formulation (Run-time Grading)

Problem formulation allows you to define a problem to be solved for each process component in a model, which by default will be inherited from the parent process component (only for the parameters that exist at that level).

This feature allows you to define the following information for scalar parameters and array elements:

- Lower/upper bounds
- Objective (minimize, maximize, target)
- Scale and weight factors (for objectives and bounds separately)

The problem formulation can be used to grade the designs for any of the components in that subflow. The Runtime Gateway uses this formulation to visually indicate how the runs of any component measure up against the stated objectives/constraints.

Typically, the formulation is defined using the Design Gateway. However, you can also define problem formulation on the Runtime Gateway. For more details about run-time grading, refer to the *Isight Runtime Gateway Guide*. For more information on using this feature in the Design Gateway, as well as detailed information on how Isight uses the feature, refer to the *Isight User's Guide*.

Understanding Parameter Filtering

You can use the Runtime Gateway Data filter feature to filter the history of runs for the selected component, reducing the amount of information displayed, which may allow you to better analyze the execution data. Filtering can be based on the desired minimum/maximum values you want included for any parameters and/or based on the "grading" of the runs using the problem formulation (lower/upper bounds, objectives). The filtered data set is what is displayed on the Parameters, History, Data Analysis, and Graphs tabs.

Note: Some of the postprocessing graphs from design driver component (for example, the Main Effects graphs for DOE) still use the full, unfiltered data set even after filtering.

For more details about parameter filtering, refer to the *Isight Runtime Gateway Guide*.

Components

Components are used as building block for models. Excel, Simcode, and DOE are examples of some of the components that SIMULIA has developed and can be included with Isight. These components are used in the examples included in this book.

You can also develop your own components to use within the Isight environment. For more information on using all SIMULIA-provided components, refer to the *Isight Component Guide*. For more information on creating custom components, refer to the *Isight Development Guide*.

Appendix C. Specimen Machinist Drawings

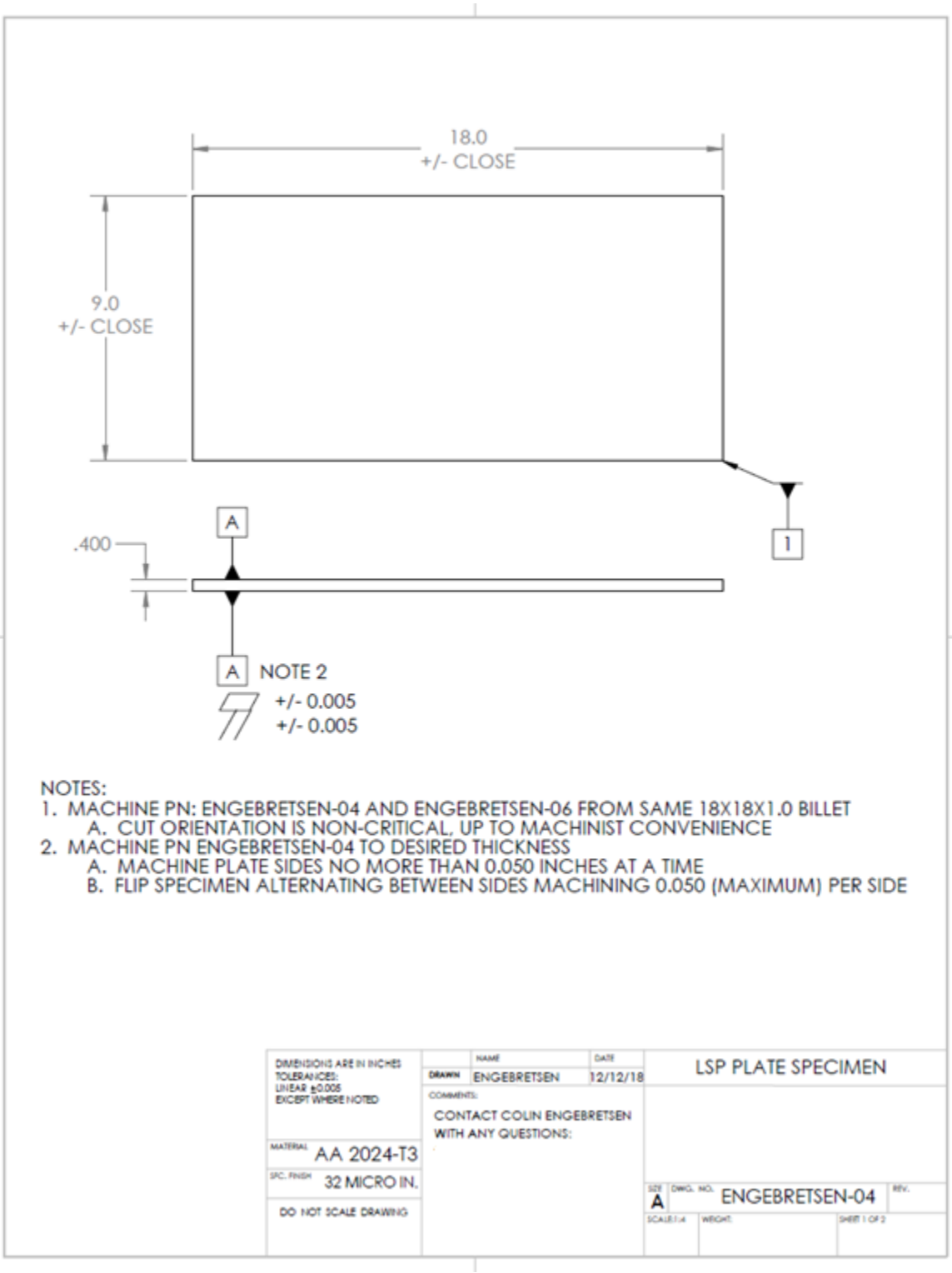

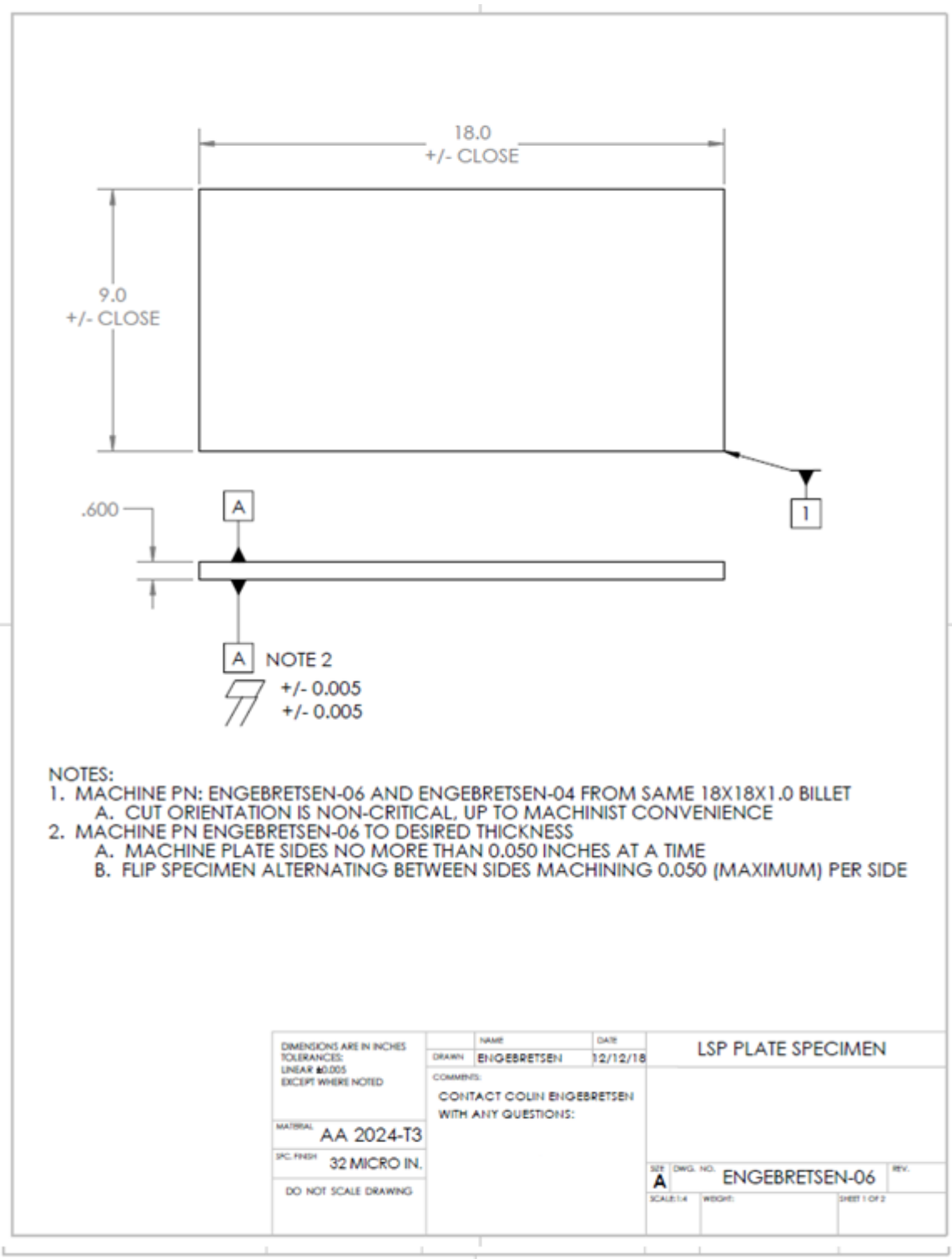

NOTES:
1. MACHINE PN: ENGEBRETSEN-06 AND ENGEBRETSEN-04 FROM SAME 18X18X1.0 BILLET
   A. CUT ORIENTATION IS NON-CRITICAL, UP TO MACHINIST CONVENIENCE
2. MACHINE PN ENGEBRETSEN-06 TO DESIRED THICKNESS
   A. MACHINE PLATE SIDES NO MORE THAN 0.050 INCHES AT A TIME
   B. FLIP SPECIMEN ALTERNATING BETWEEN SIDES MACHINING 0.050 (MAXIMUM) PER SIDE

DIMENSIONS ARE IN INCHES TOLERANCES: LINEAR ±0.005 EXCEPT WHERE NOTED	NAME	DATE	LSP PLATE SPECIMEN
	DRAWN ENGEBRETSEN	12/12/18	
	COMMENTS: CONTACT COLIN ENGEBRETSEN WITH ANY QUESTIONS:		
MATERIAL AA 2024-T3			
SPC. FINISH 32 MICRO IN.			
DO NOT SCALE DRAWING		SIZE A DWG. NO. ENGEBRETSEN-06	REV.
		SCALE:1:4 WEIGHT:	SHEET 1 OF 2

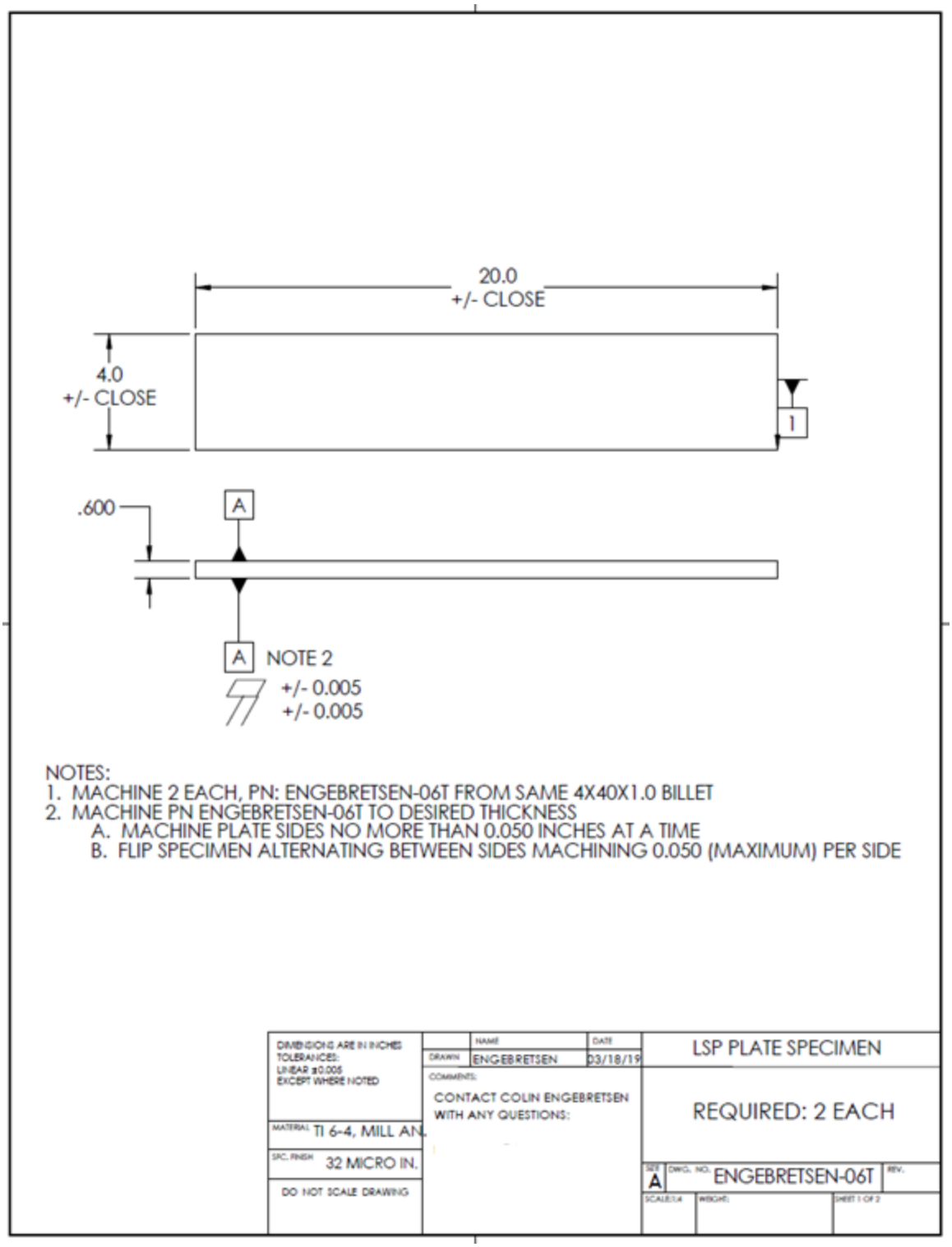

NOTES:
1. MACHINE 2 EACH, PN: ENGEBRETSEN-06T FROM SAME 4X40X1.0 BILLET
2. MACHINE PN ENGEBRETSEN-06T TO DESIRED THICKNESS
   A. MACHINE PLATE SIDES NO MORE THAN 0.050 INCHES AT A TIME
   B. FLIP SPECIMEN ALTERNATING BETWEEN SIDES MACHINING 0.050 (MAXIMUM) PER SIDE

DIMENSIONS ARE IN INCHES TOLERANCES: LINEAR ±0.005 EXCEPT WHERE NOTED		NAME	DATE
	DRAWN	ENGEBRETSEN	03/18/19
	COMMENTS: CONTACT COLIN ENGEBRETSEN WITH ANY QUESTIONS:		
MATERIAL: TI 6-4, MILL ANN.			
SRC. FINISH: 32 MICRO IN.			
DO NOT SCALE DRAWING			

LSP PLATE SPECIMEN

REQUIRED: 2 EACH

SIZE	DWG. NO.	REV.
A	ENGEBRETSEN-06T	

SCALE: 1:4 | WEIGHT: | SHEET 1 OF 2

Appendix D. Surface Displacement Averaging MATLAB Code

```
close all
clc
% Depth Cutof
D=-.002;
% Size of Buffer on either side of dimple
ybuff=36;
xbuff=154;
% Which Plate is used (must match prefix name of imported matrices
plates={'one','two'};
for m=1:length(plates)
    plate=plates{m};
Zsum=zeros(300,800);
sizes=zeros(8,2);
for n=1:8
% Temp. renaming of each surface to preserve original data
    eval(['surf=',plate,num2str(n),';'])
% Extracting data into vectors
X=surf(:,1);
Y=surf(:,2);
Z=surf(:,3);
% Turning vectors into surface sized vectors/matrices
Ybar=unique(Y);
Xbar=unique(X);
Z2=reshape(Z,[801,161]);
Z2=Z2';
% Centering all spots about the dimple
[row,col]=find(Z2<D);
row=unique(row);
col=unique(col);
row=row(6)-ybuff:row(end-5)+ybuff;
col=col(6)-xbuff:col(end-5)+xbuff;
Ybar=Ybar(row)-Ybar(round(median(row)));
Xbar=Xbar(col)-Xbar(round(median(col)));
Z2=Z2(row,col);
% New figure for each surface
figure
surface(Xbar,Ybar,Z2,'edgecolor','none');
title([plate,num2str(n)])
caxis([-.022 0.009])
axis([-6.2 6.2 -6.2 6.2])
Zsum(row-row(1)+1,col-col(1)+1)=Zsum(row-row(1)+1,col-col(1)+1)+Z2;
sizes(n,:)=[size(Z2)];
end
Z2=Zsum(1:length(Ybar),1:length(Xbar))/8;
Z2=Z2-mean(mean([Z2(1:4,1:12),Z2(1:4,end-11:end),Z2(end-
3:end,1:12),Z2(end-3:end,end-11:end)]));
figure
surface(Xbar,Ybar,Z2,'edgecolor','none');
caxis([-0.022 0.009])
axis([-6.2 6.2 -6.2 6.2])
end
```

Appendix E. Surface Displacement Alignment and Averaging MATLAB Code

```
for i=1:8
    eval(strcat('Y=Y', num2str(i),';'));
    eval(strcat('X=X', num2str(i),';'));
    ind1=find(abs(Y)==min(abs(Y(1:400))));
    ind2=find(abs(Y)==min(abs(Y(401:801))));
    ind1=ind1(1);
    ind2=ind2(1);
    if Y(ind1)>0
        ydif=Y(ind1+1)-Y(ind1);
        xdif=X(ind1+1)-X(ind1);
        x1zero=X(ind1)+xdif*(-Y(ind1)/ydif);
    elseif Y(ind1)<0
        ydif=Y(ind1)-Y(ind1-1);
        xdif=X(ind1)-X(ind1-1);
        x1zero=X(ind1-1)+xdif*(-Y(ind1-1)/ydif);
    else
        x1zero=X(ind1);
    end
    if Y(ind2)>0
        ydif=Y(ind2+1)-Y(ind2);
        xdif=X(ind2+1)-X(ind2);
        x2zero=X(ind2)+xdif*(-Y(ind2)/ydif);
    elseif Y(ind2)<0
        ydif=Y(ind2)-Y(ind2-1);
        xdif=X(ind2)-X(ind2-1);
        x2zero=X(ind2-1)+xdif*(-Y(ind2-1)/ydif);
    else
        x2zero=X(ind2);
    end
        midx=(x2zero-x1zero)/2+x1zero;
        eval(strcat('X',num2str(i),'=X-midx;'));
end
start=max([X1(1);X2(1);X3(1);X4(1);X5(1);X6(1);X7(1);X8(1)]);
for i=1:8
    eval(strcat('inds=find(X',num2str(i),'<start);'));
    eval(strcat('X',num2str(i),'(inds)=[];'));
    eval(strcat('Y',num2str(i),'(inds)=[];'));
end
smallest=min([length(X1);length(X2);length(X3);length(X4);...
        length(X5);length(X6);length(X7);length(X8)]);
    X=[];
    AVG=[];
    sdev=[];
for i=1:smallest
    X(i,1)=start+0.02*i;
    AVG(i,1)=mean([Y1(i);Y2(i);Y3(i);Y4(i);Y5(i);Y6(i);Y7(i);Y8(i)]);
    sdev(i,1)=std([Y1(i);Y2(i);Y3(i);Y4(i);Y5(i);Y6(i);Y7(i);Y8(i)]);
end
minus=AVG-sdev;
plus=AVG+sdev;
plot(X,AVG,X,plus,X,minus)
```

Appendix F. Abaqus Execution Python Code

```
# -*- coding: mbcs -*-
#
# Abaqus/CAE Release 6.14-1 python script
# Internal Version: 2014_06_04-18.11.02 134264
# Colin Engebretsen
#

# from driverUtils import executeOnCaeGraphicsStartup
# executeOnCaeGraphicsStartup()
#: Executing "onCaeGraphicsStartup()" in the site directory ...
from abaqus import *
from abaqusConstants import *
session.Viewport(name='Viewport: 1', origin=(0.0, 0.0), width=441.729187011719,
    height=247.200012207031)
session.viewports['Viewport: 1'].makeCurrent()
session.viewports['Viewport: 1'].maximize()
from caeModules import *
from driverUtils import executeOnCaeStartup
executeOnCaeStartup()
session.viewports['Viewport: 1'].partDisplay.geometryOptions.setValues(
    referenceRepresentation=ON)
a = mdb.models['Model-1'].rootAssembly
session.viewports['Viewport: 1'].setValues(displayedObject=a)
session.viewports['Viewport: 1'].assemblyDisplay.setValues(
    optimizationTasks=OFF, geometricRestrictions=OFF, stopConditions=OFF)
mdb.JobFromInputFile(name='Axi',
    inputFileName='I:\\My Documents\\Abaqus\\2019\\Q3D&AxiFinal4Isight\\Ax118x157Final.inp',
    type=ANALYSIS, atTime=None, waitMinutes=0, waitHours=0, queue=None,
    memory=90, memoryUnits=PERCENTAGE, getMemoryFromAnalysis=True,
    explicitPrecision=SINGLE, nodalOutputPrecision=SINGLE, userSubroutine='',
    scratch='', resultsFormat=ODB, parallelizationMethodExplicit=DOMAIN,
    numDomains=8, activateLoadBalancing=False, multiprocessingMode=DEFAULT,
    numCpus=8)
mdb.jobs['Axi'].submit(consistencyChecking=OFF)
mdb.jobs['Axi'].waitForCompletion()
o3 = session.openOdb(name='I:/My Documents/Abaqus/2019/Q3D&AxiFinal4Isight/Axi.odb')
session.viewports['Viewport: 1'].setValues(displayedObject=o3)
session.viewports['Viewport: 1'].view.setValues(nearPlane=0.0241018,
    farPlane=0.0363003, width=0.00800811, height=0.00464673,
    viewOffsetX=-0.00100671, viewOffsetY=0.00233465)
session.Path(name='AcrossTop', type=POINT_LIST, expression=((0.0, 0.0, 0.0), (
    0.0059944, 0.0, 0.0)))
session.Path(name='HD1', type=POINT_LIST, expression=((0.0, -3e-05, 0.0), (
    0.00045, -3e-05, 0.0)))
session.Path(name='HD2', type=POINT_LIST, expression=((0.0, -8e-05, 0.0), (
    0.00045, -8e-05, 0.0)))
session.Path(name='HD3', type=POINT_LIST, expression=((0.0, -0.00013, 0.0), (
    0.00045, -0.00013, 0.0)))
session.Path(name='HD4', type=POINT_LIST, expression=((0.0, -0.00018, 0.0), (
    0.00045, -0.00018, 0.0)))
session.Path(name='HD5', type=POINT_LIST, expression=((0.0, -0.00023, 0.0), (
    0.00045, -0.00023, 0.0)))
session.Path(name='HD6', type=POINT_LIST, expression=((0.0, -0.00028, 0.0), (
    0.00045, -0.00028, 0.0)))
```

```
session.Path(name='HD7', type=POINT_LIST, expression=((0.0, -0.00033, 0.0), (
    0.00045, -0.00033, 0.0)))
session.Path(name='HD8', type=POINT_LIST, expression=((0.0, -0.00038, 0.0), (
    0.00045, -0.00038, 0.0)))
session.Path(name='HD9', type=POINT_LIST, expression=((0.0, -0.00043, 0.0), (
    0.00045, -0.00043, 0.0)))
session.Path(name='HD10', type=POINT_LIST, expression=((0.0, -0.00048, 0.0), (
    0.00045, -0.00048, 0.0)))
session.viewports['Viewport: 1'].view.setValues(nearPlane=0.0241609,
    farPlane=0.0362412, width=0.00832824, height=0.00483249,
    viewOffsetX=-0.00114209, viewOffsetY=0.00265961)
session.viewports['Viewport: 1'].odbDisplay.setPrimaryVariable(
    variableLabel='U', outputPosition=NODAL, refinement=(COMPONENT, 'U2'))
pth = session.paths['AcrossTop']
session.XYDataFromPath(name='AxiU2-1', path=pth, includeIntersections=True,
    projectOntoMesh=False, pathStyle=UNIFORM_SPACING, numIntervals=119,
    projectionTolerance=0, shape=UNDEFORMED, labelType=TRUE_DISTANCE_X)
session.viewports['Viewport: 1'].odbDisplay.setPrimaryVariable(
    variableLabel='S', outputPosition=INTEGRATION_POINT, refinement=(COMPONENT,
    'S11'))
pth = session.paths['HD1']
session.XYDataFromPath(name='AxiHD1S11', path=pth, includeIntersections=True,
    projectOntoMesh=False, pathStyle=UNIFORM_SPACING, numIntervals=10,
    projectionTolerance=0, shape=UNDEFORMED, labelType=TRUE_DISTANCE_X)
pth = session.paths['HD2']
session.XYDataFromPath(name='AxiHD2S11', path=pth, includeIntersections=True,
    projectOntoMesh=False, pathStyle=UNIFORM_SPACING, numIntervals=10,
    projectionTolerance=0, shape=UNDEFORMED, labelType=TRUE_DISTANCE_X)
pth = session.paths['HD3']
session.XYDataFromPath(name='AxiHD3S11', path=pth, includeIntersections=True,
    projectOntoMesh=False, pathStyle=UNIFORM_SPACING, numIntervals=10,
    projectionTolerance=0, shape=UNDEFORMED, labelType=TRUE_DISTANCE_X)
pth = session.paths['HD4']
session.XYDataFromPath(name='AxiHD4S11', path=pth, includeIntersections=True,
    projectOntoMesh=False, pathStyle=UNIFORM_SPACING, numIntervals=10,
    projectionTolerance=0, shape=UNDEFORMED, labelType=TRUE_DISTANCE_X)
pth = session.paths['HD5']
session.XYDataFromPath(name='AxiHD5S11', path=pth, includeIntersections=True,
    projectOntoMesh=False, pathStyle=UNIFORM_SPACING, numIntervals=10,
    projectionTolerance=0, shape=UNDEFORMED, labelType=TRUE_DISTANCE_X)
pth = session.paths['HD6']
session.XYDataFromPath(name='AxiHD6S11', path=pth, includeIntersections=True,
    projectOntoMesh=False, pathStyle=UNIFORM_SPACING, numIntervals=10,
    projectionTolerance=0, shape=UNDEFORMED, labelType=TRUE_DISTANCE_X)
pth = session.paths['HD7']
session.XYDataFromPath(name='AxiHD7S11', path=pth, includeIntersections=True,
    projectOntoMesh=False, pathStyle=UNIFORM_SPACING, numIntervals=10,
    projectionTolerance=0, shape=UNDEFORMED, labelType=TRUE_DISTANCE_X)
pth = session.paths['HD8']
session.XYDataFromPath(name='AxiHD8S11', path=pth, includeIntersections=True,
    projectOntoMesh=False, pathStyle=UNIFORM_SPACING, numIntervals=10,
    projectionTolerance=0, shape=UNDEFORMED, labelType=TRUE_DISTANCE_X)
pth = session.paths['HD9']
session.XYDataFromPath(name='AxiHD9S11', path=pth, includeIntersections=True,
    projectOntoMesh=False, pathStyle=UNIFORM_SPACING, numIntervals=10,
    projectionTolerance=0, shape=UNDEFORMED, labelType=TRUE_DISTANCE_X)
pth = session.paths['HD10']
session.XYDataFromPath(name='AxiHD10S11', path=pth, includeIntersections=True,
```

```
    projectOntoMesh=False, pathStyle=UNIFORM_SPACING, numIntervals=10,
    projectionTolerance=0, shape=UNDEFORMED, labelType=TRUE_DISTANCE_X)
x0 = session.xyDataObjects['AxiHD1S11']
x1 = session.xyDataObjects['AxiHD2S11']
x2 = session.xyDataObjects['AxiHD3S11']
x3 = session.xyDataObjects['AxiHD4S11']
x4 = session.xyDataObjects['AxiHD5S11']
x5 = session.xyDataObjects['AxiHD6S11']
x6 = session.xyDataObjects['AxiHD7S11']
x7 = session.xyDataObjects['AxiHD8S11']
x8 = session.xyDataObjects['AxiHD9S11']
x9 = session.xyDataObjects['AxiHD10S11']
x10 = session.xyDataObjects['AxiU2-1']
session.writeXYReport(fileName='AxiHDData.csv', appendMode=OFF, xyData=(x0, x1, x2, x3, x4, x
    5,
    x6, x7, x8, x9))
session.writeXYReport(fileName='AxiU2Data.csv', appendMode=OFF, xyData=(x10))
```

Appendix G. Hill Engineering Residual Stress Report [105]

HILL ENGINEERING
Predict. Test. Perform.

Background

Hill Engineering was contracted by Peerless Technologies Corporation to perform residual stress measurements on four plate specimens. Residual stress was measured using the incremental hole drilling method. This report summarizes these measurements with results displayed in the form of line plots residual stress versus depth.

Specimen geometry

Residual stress measurements were performed on four plate specimens. The test specimens were labeled with serial numbers: 82495, 82496, S/N 1, and S/N 2. Figure 1 shows the four plate specimens as received.

Specimens 82495 and 82496 were made from 2024-T351 aluminum, which was assumed to have the following elastic material properties: E = 10,600 ksi GPa, $\nu = 0.33$.

Specimens S/N 1 and S/N 2 were made from Ti-6Al-4V, which was assumed to have the following elastic material properties: E = 16,500 ksi, $\nu = 0.342$.

These elastic material properties were used for residual stress calculations.

Experimental details

The incremental hole drilling method was used to measure residual stress at selected locations on each plate. Figure 2 and Figure 3 show the measurement location layout for each specimen geometry. Measurements HD4 though HD11 and HD15 through HD18 are located on single spot laser shock peening (LSP) sites on the plate specimens. Measurements HD1, HD2, HD3, HD12, HD13 and HD14 are located away from the LSP sites.

All measurements were drilled in 0.001 inch increments to a final depth of 0.02 inches for a total of 20 increments. HD7 for specimen 82495 was drilled in 0.002 inch increments to a final depth of 0.04 inches. The following is a summary of the hole drilling method measurements as they were applied here. For additional background information please consult reference [1].

1. Install strain gage rosette on hole drilling site.
2. Incrementally drill hole through center of strain gage and record strain release for each incremental depth.
3. Compute residual stress from measured strain data.

Results

Line plots of the hole drilling method measured residual stress vs. depth for each measurement are shown in Figure 4 through Figure 18.

Hill Engineering is available to provide additional analysis or interpretation of the results as needed.

Page 2 of 13

HILL ENGINEERING
Predict. Test. Perform.

Figures

Figure 1: Photograph of the test specimens as received.

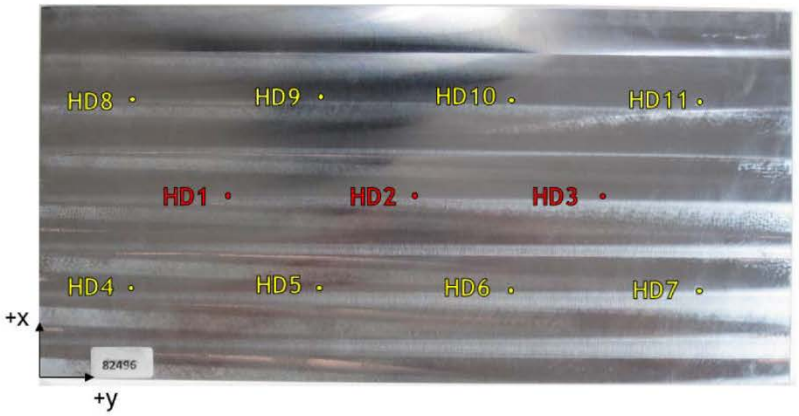

Figure 2: Representative diagram of hole drilling measurement locations for specimens: 82495 and 82496.

Figure 3: Representative diagram of hole drilling measurement locations for specimens: SN 1 and SN 2.

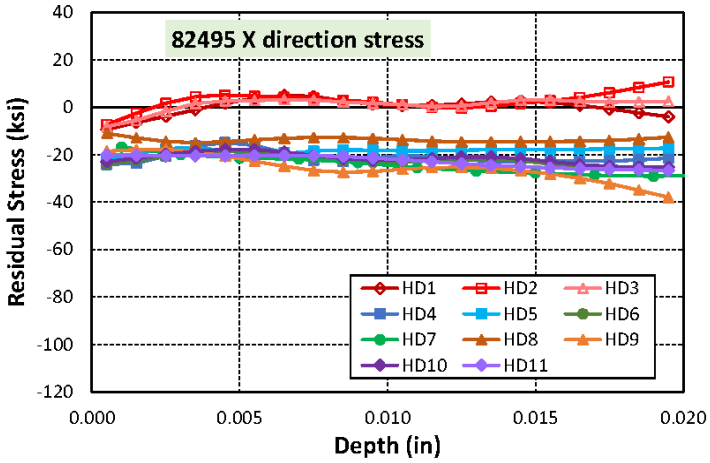

Figure 4: Line plots of the residual stresses measured in x-direction for specimen 82495.

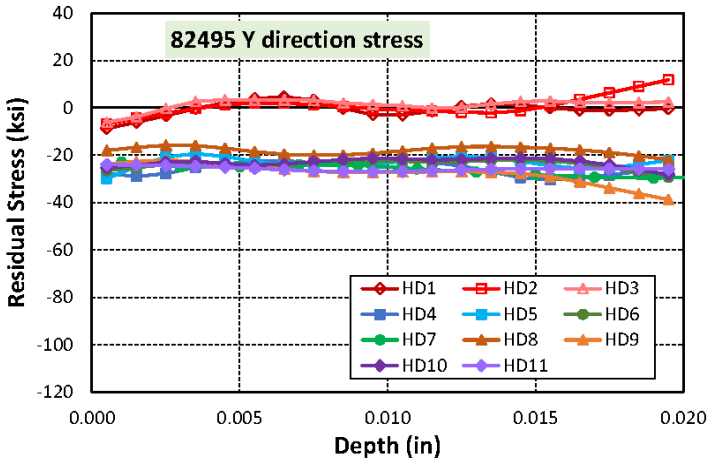

Figure 5: Line plots of the residual stresses measured in y-direction for 82495.

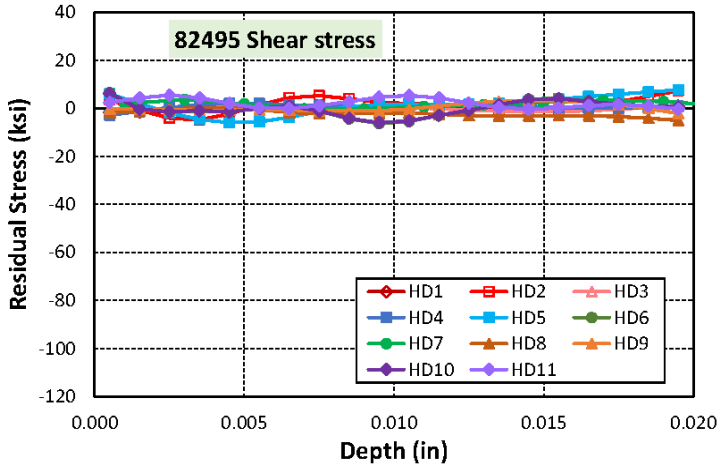

Figure 6: Line plots of the measured shear stresses for specimen 82495.

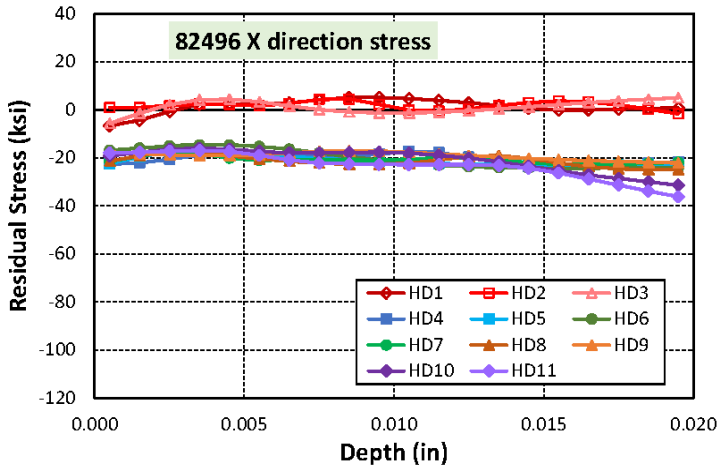

Figure 7: Line plots of the residual stresses measured in x-direction for 82496.

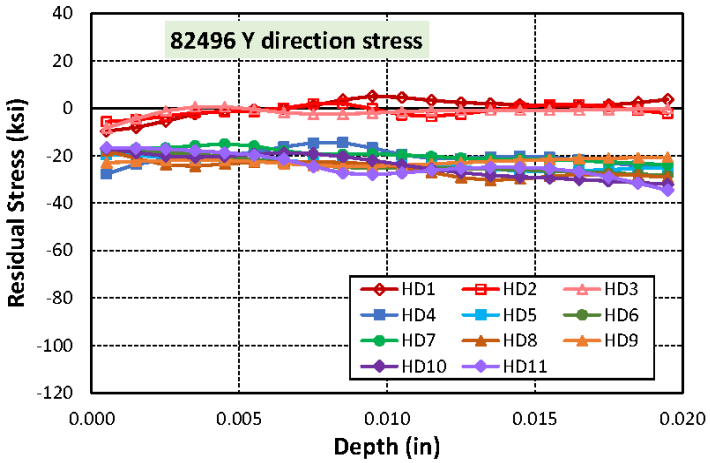

Figure 8: Line plots of the residual stresses measured in y-direction for 82496.

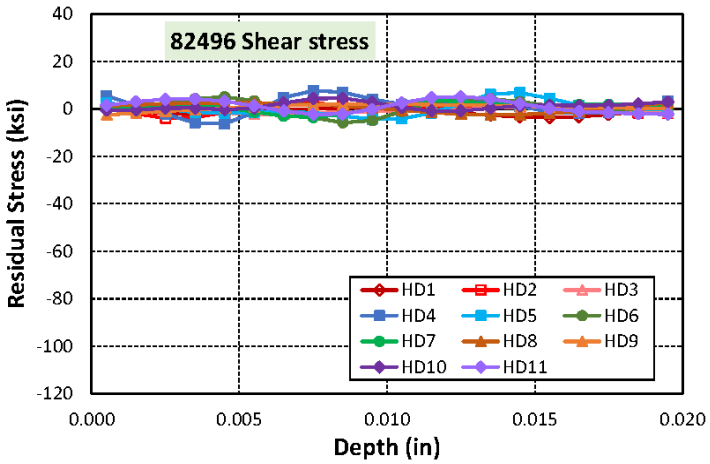

Figure 9: Line plots of the measured shear stresses for specimen 82496.

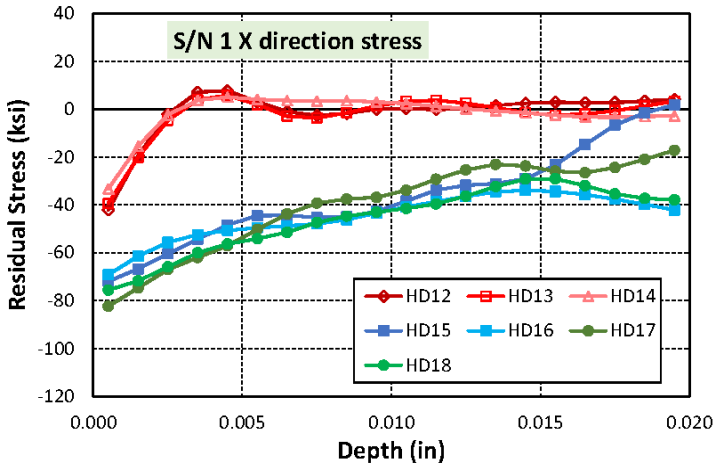

Figure 10: Line plots of the residual stresses measured in x-direction for SN 1.

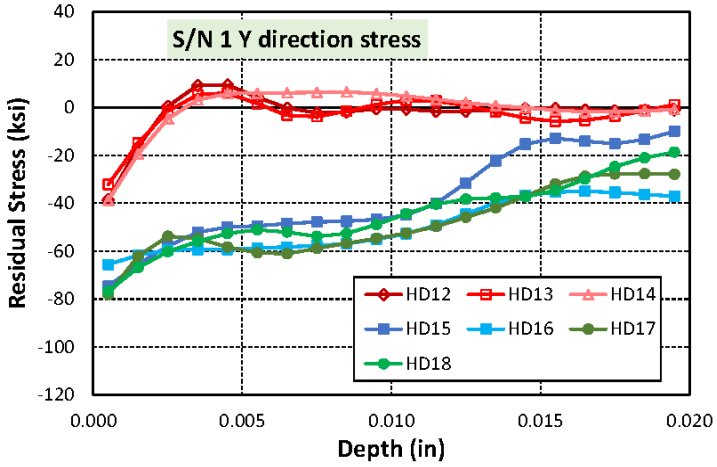

Figure 11: Line plots of the residual stresses measured in y-direction for SN 1.

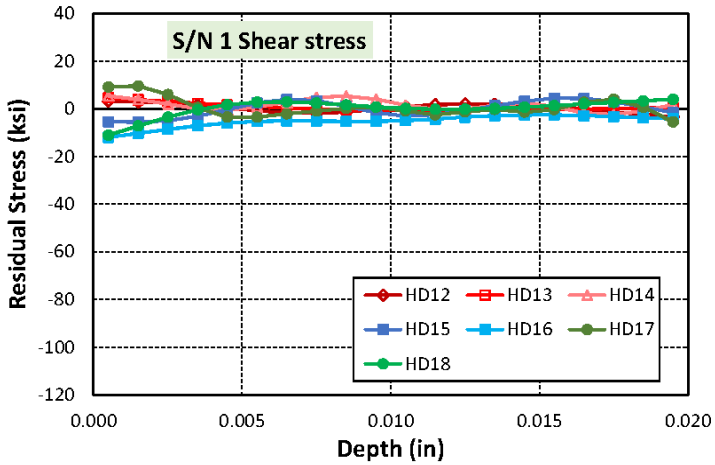

Figure 12: Line plots of the measured shear stresses for specimen SN 1.

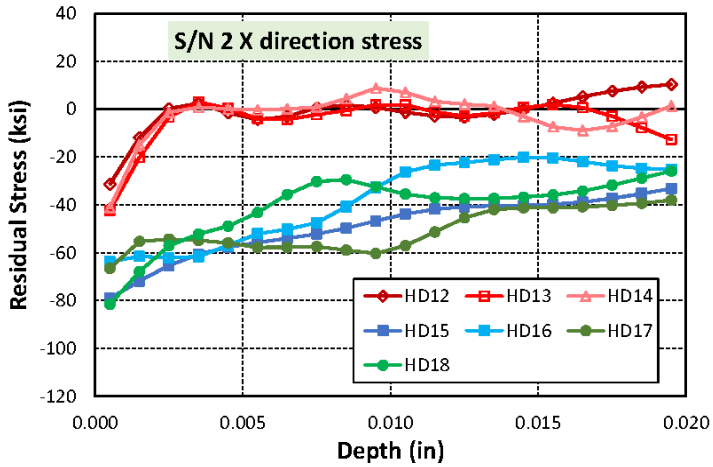

Figure 13: Line plots of the residual stresses measured in x-direction for SN 2.

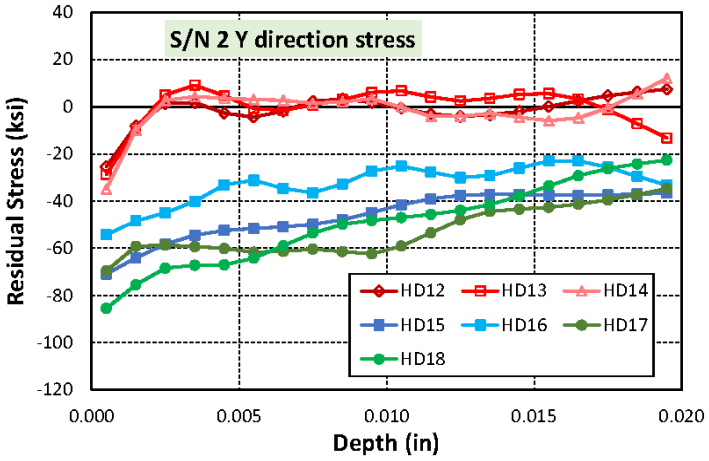

Figure 14: Line plots of the residual stresses measured in y-direction for SN 2.

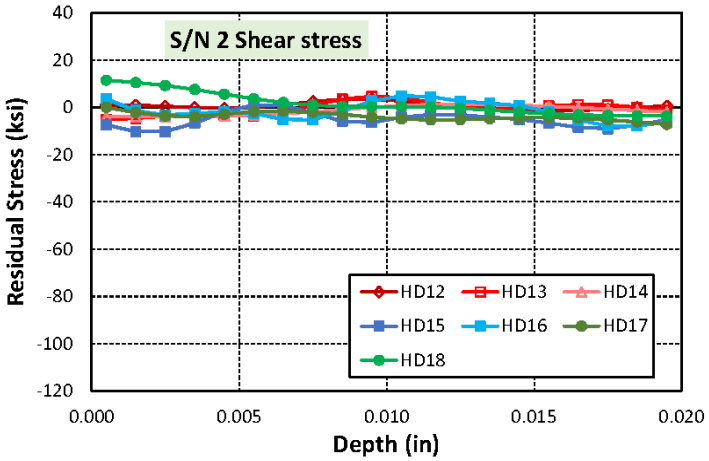

Figure 15: Line plots of the measured shear stresses for specimen SN 2.

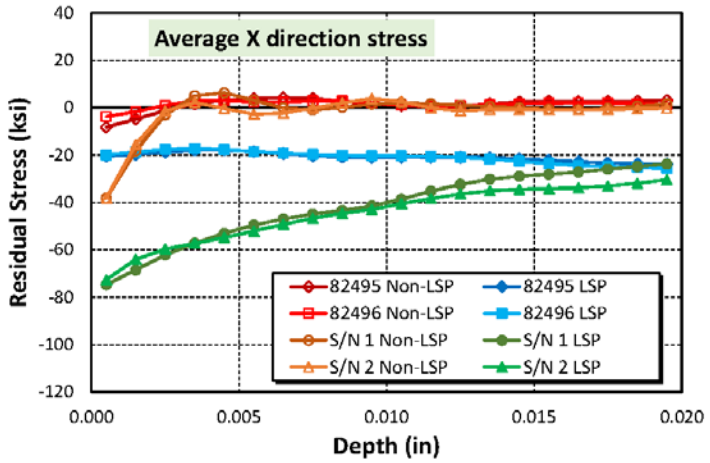

Figure 16: Line plots of the average residual stresses measured in x-direction for each plate specimen.

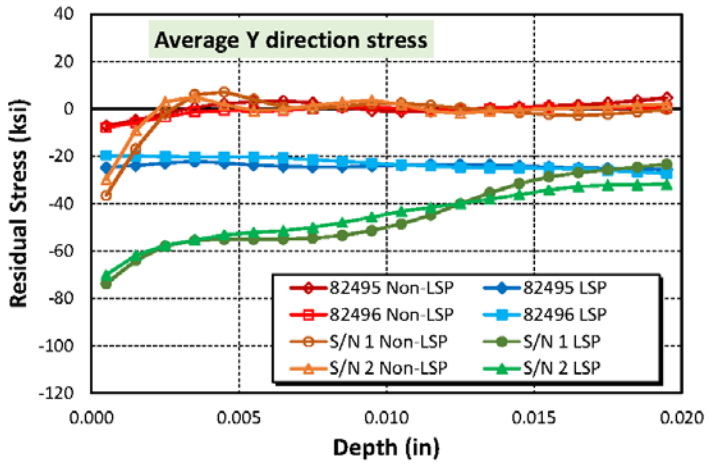

Figure 17: Line plots of the average residual stresses measured in y-direction for each plate specimen.

HILL ENGINEERING
Predict. Test. Perform.

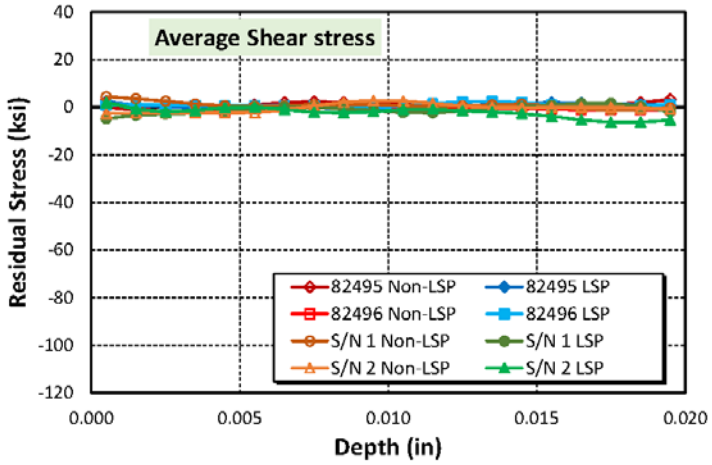

Figure 18: Line plots of the average measured shear stresses for each plate specimen.

Appendix H. Optical Profilometer Calibration Documentation

NANOVEA®

Ref: 400um
Date: 11/12/10
Page: 2/3

METROLOGICAL CHARACTERISTICS OF THE CHR CONTACTLESS SENSOR
Delivered to: SelectTech Services Co.

Introduction

The metrological characteristics have been measured in Nanovea Metrology laboratory.
The measurementswere carried out on a calibration bench by comparison with a Heindenhain LIP 372 ZERODUR encoder.

Sensor identification

Controller type: CHR 150
Controller serial number: 10.30.1581
Controller channel: 1
Calibration table location: 0

Chromatic lens type: CL2
Chromatic lens serial number: 10.29.6215
Magnifier type: MG140
Magnifier serial number:
Fiber type: Standard

Nominal sensor characteristics

Nominal measuring range: 400.0 micrometers
Numerical aperture: 0.47
Max measuring angle for specular samples: 28.0 deg.
Working distance: 11.0 millimeters
Quantization step: 0.013 micrometers
Lateral resolution: 1.5 micrometers
Max accepted linearity error: 0.06 micrometers

Measured metrological characteristics

Measuring range: 400.0 micrometers
Max linearity error: 0.04 micrometers
Static noise at the center of measuring range: 12 nanometers

Nanovea Inc. - 6 Morgan, Suite 156 - Irvine, CA 92618
Tel. 866 333 4674 - Fax 949 461 9232 - Email info@nanovea.com - www.nanovea.com

NANOVEA®

Ref: 400um
Date: 11/12/10
Page: 1/3

METROLOGICAL CHARACTERISTICS of the CHR CONTACTLESS OPTICAL SENSOR

MEASUREMENT REPORT

Delivered to: SelectTech Services Co.

Sensor serial number: 10.30.1581

Chromatic lens serial number: 10.29.6215

Magnifier serial number:

	Experimenter	Metrology Manager
Name	Frank Martinez	Craig Leising
Date	11/12/10	11/12/10
Visa		

Nanovea Inc. - 6 Morgan, Suite 156 - Irvine, CA 92618
Tel. 866 333 4674 - Fax 949 461 9232 - Email info@nanovea.com - www.nanovea.com

VLSI Standards, Inc.

Certification Program: SHSThick7.1

Certificate of Calibration - Annex 1 of 1

Step Height Standard

Model Number : SHS - 50.0 Q
Serial Number : 10763-25-13
Calibration Date : 02/28/2011

Summary of (step height) input and output quantities:

Input quantity:

		Mean value
NISTc	NIST reference (NIST report of calibration)	50.0464 µm
NISTm	NIST reference (VLSI observations)	49.8133 µm
Ym	SHS (VLSI uncorrected observations)	49.2417 µm

Output quantity:

		Mean value
Yc	SHS (VLSI corrected value)	49.4721 µm
	*Yc = NISTc / NISTm * Ym*	

Summary of (step height) standard uncertainty components, combined standard uncertainty, degrees of freedom and expanded uncertainty coverage factor :

	Source of uncertainty	Value (µm)	Partial derivative	Combined component (µm)	Degrees of freedom	"Uncertainty of an uncertainty"
u(NISTc) Combined	NIST reference traceability (NIST report of calibration)	0.11574	0.98853	0.11441	8	25%
u(NISTm) Type A	NIST reference reproducibility (VLSI observations)	0.00048	1	0.00048	8	25%
u(resol) Type B	VLSI instrument vertical resolution	3.4E-06	1	3.4E-06	5000	1%
u(NISTmr) Combined	NIST reference reproducibility (VLSI corrected)	0.00054	0.99315	0.00054	13	
	u(NISTmr) = sqrt{[u(NISTm)]^2 + [u(prec)]^2 + [u(resol)]^2}					
u(Ym) Type A	SHS step height uniformity (VLSI observations)	0.00835	1	0.00835	8	25%
u(resol') Type B	VLSI instrument precision	2.6E-04	1	2.6E-04	8	
u(Ymr) Combined	SHS step height measurement (VLSI corrected)	0.00835	1.00468	0.00839	8	
	u(Ymr) = sqrt{[u(Ym)]^2 + [u(prec)]^2 + [u(resol)]^2}					

u(Yc) **SHS combined standard uncertainty**

*u(Yc) = sqrt {[Ym / NISTm * u(NISTc)]^2 + [Ym * NISTc / NISTm^2 * u(NISTmr)]^2 + + [NISTc / NISTm * u(Ymr)]^2}*

u(Yc)		degrees of freedom *ν* (eff)	coverage t - factor
0.11472	µm	**8**	**2.31**

VLSI Standards Incorporated

NVLAP
Lab Code 200302-0

CERTIFICATE OF CALIBRATION

STEP HEIGHT STANDARD

Model Number : SHS - 50.0 Q

Serial Number : 10763-25-13

Step Material: Step etched in quartz

CALIBRATED STEP HEIGHT : Certification Program: SHSThick7.1

Mean Value		Expanded Uncertainty[1]
(49.472	±	0.265) µm

The certified step height value and uncertainty of measurement is traceable to VLSI Standards' master step height standard 4343-23-21 which is certified by the National Institute of Standards and Technology as described in the NIST Test Number 821/261555-99A.[2]

Environmental conditions at the time of measurement:

Temperature:	(21	±	1	) °C
Humidity:	(42	±	2	) %

VLSI Standards is fully accredited by NVLAP to perform this calibration under Lab Code 200302-0.
This standard is calibrated in compliance with ISO 10012:2003(E) and ANSI/NCSL Z540-1-1994.

Dimitar Ovtcharov
Calibration Engineer

Terry Trinh
Quality Assurance

Shipment Date: MAR 07 2011

[1] *At the 95% confidence level, as defined by the ISO Guide to the Expression of Uncertainty in Measurement. The expanded uncertainty is obtained by multiplying the combined standard uncertainty by a coverage factor. Please see the Certificate of Calibration, Annex section.*

[2] *This certificate does not constitute product endorsement by NVLAP or by any U.S. Government agency.*

5 Technology Drive, Milpitas, CA 95035-7916 • (408) 428-1800 • Fax (408) 428-9555 • www.vlsistandards.com

NANOVEA®

Ref: 400um
Date: 11/12/10
Page: 3/3

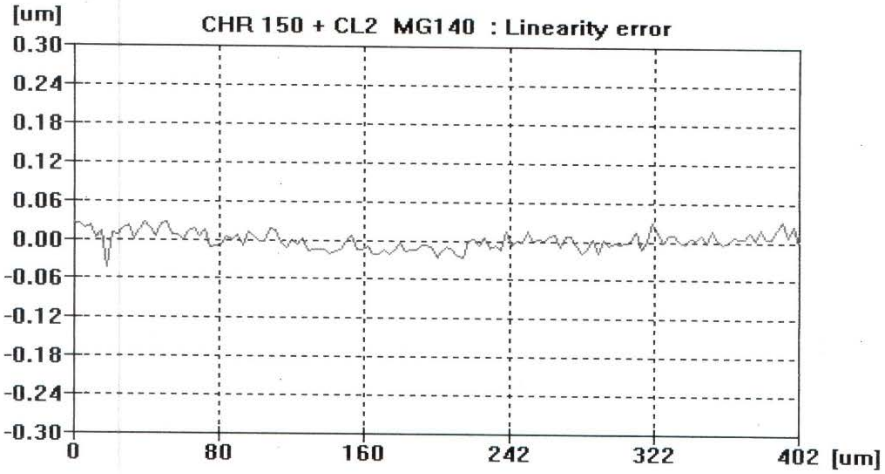

Delivered to: SelectTech Services Co.
Sensor serial number: 10.30.1581
Chromatic lens serial number: 10.29.6215
Magnifier serial number:

Nanovea Inc. - 6 Morgan, Suite 156 - Irvine, CA 92618
Tel. 866 333 4674 - Fax 949 461 9232 - Email info@nanovea.com - www.nanovea.com

Bibliography

[1] Ding, K. and Ye, L., *Laser Shock Peening Performance And Process Simulation*. Cambridge: Woodhead Publishing Limited, 2006.

[2] Veitch, L. and Laprade, E., "Recent Developments In The Joint Strike Fighter Durability Testing," *Institute For Defense Analyses Research Notes*, pp. 47–52, 2016.

[3] Gonzalez-Romero, J., *et al.*, "Piezoresistive Method For A Laser Induced Shock Wave Detection On Solids," *Proceedings Of SPIE - The International Society For Optical Engineering*, vol. 10403, no. August, 2017.

[4] SAE Aerospace, "Aerospace Material Specification 2546, Laser Peening." SAE International, Warrendale, PA, 2010.

[5] Neuman, F., "Momentum Transfer And Cratering Effects Produced By Giant Laser Pulses," *Applied Physics Letters*, vol. 4, no. 9, pp. 167–169, 1964.

[6] Gregg, D. and Thomas, S., "Momentum Transfer Produced By Focused Laser Giant Pulses," *Journal Of Applied Physics*, vol. 37, no. 7, pp. 2787–2789, 1966.

[7] Anderholm, N., "Laser-Generated Stress Waves," *Applied Physics Letters*, vol. 16, no. 3, pp. 113–115, 1970.

[8] O'Keefe, J. and Skeen, C., "Laser-Induced Stress-Wave And Impulse Augmentation," *Applied Physics Letters*, vol. 21, no. 10, pp. 464–466, 1972.

[9] Fox, J., "Effect Of Water And Paint Coatings On Laser-Irradiated Targets," *Applied Physics Letters*, vol. 24, no. 10, pp. 461–464, 1974.

[10] Yang, L., "Stress Waves Generated In Thin Metallic Films By A Q -Switched Ruby Laser," *Journal Of Applied Physics*, vol. 45, no. 6, pp. 2601–2608, 1974.

[11] Fairand, B., *et al.*, "Quantitative Assessment Of Laser-Induced Stress Waves Generated At Confined Surfaces," *Applied Physics Letters*, vol. 25, no. 8, pp. 431–433, 1974.

[12] Clauer, A., *et al.*, "Effects Of Laser Induced Shock Waves On Metals," *Shock Waves And High-Strain-Rate Phenomena In Metals*, pp. 675–703, 1981.

[13] Fairand, B. and Clauer, A., "Laser Generation Of High-Amplitude Stress Waves In Materials," *Journal Of Applied Physics*, vol. 50, no. 3, pp. 1497–1502, 1979.

[14] Clauer, A., *et al.*, "Laser Shock Hardening Ot Weld Zones In Aluminum Alloys," *Metallurgical Transactions A*, vol. 8, no. December, pp. 1871–1876, 1977.

[15] "LSP Technologies Brochure," *Laser Peen Process*, 2017. [Online]. Available: http://www.lsptechnologies.com/brochures/LaserPeen2016.pdf.

[16] Chu, J., *et al.*, "Effects Of Laser-Shock Processing On The Microstructure And Surface Mechanical Properties Of Hadfield Manganese Steel," *Metallurgical And Materials Transactions A*, vol. 26, no. 6, pp. 1507–1517, 1995.

[17] Clauer, A., *et al.*, "The Effects Of Laser Shock Processing On The Fatigue Properties Of 2024-T3 Aluminum," *Lasers In Materials Processing*, no. January, pp. 7–22, 1983.

[18] Peyre, P., *et al.*, "Laser Shock Processing Of Aluminium Alloys. Application To High Cycle Fatigue Behaviour," *Materials Science And Engineering: A*, vol. 210, pp. 102–113, 1996.

[19] Clauer, A., "Laser Shock Peening For Fatigue Resistance," *Surface Performance Of Titanium*, pp. 217–230, 1996.

[20] Yang, J., *et al.*, "Laser Shock Peening On Fatigue Behavior Of 2024-T3 Al Alloy With Fastener Holes And Stopholes," *Materials Science And Engineering A*, vol. 298, no. 1–2, pp. 296–299, 2001.

[21] Mannava, S., *et al.*, "Laser Shock Peened Gas Turbine Engine Fan Blade Edges," US Patent No. 5591009, 1997.

[22] Somers, R., *et al.*, "Laser Shock Peening Quality Assurance By Volumetric Analysis Of Laser Shock Peened Dimple," US Patent No. 5948293, 1999.

[23] Ruschau, J., *et al.*, "Fatigue Crack Nucleation And Growth Rate Behavior Of Laser Shock Peened Titanium," *International Journal Of Fatigue*, vol. 21, pp. 199–209, 1999.

[24] Nikitin, I. and Altenberger, I., "Comparison Of The Fatigue Behavior And Residual Stress Stability Of Laser-Shock Peened And Deep Rolled Austenitic Stainless Steel AISI 304 In The Temperature Range 25-600 C," *Materials Science And Engineering A*, vol. 465, no. 1–2, pp. 176–182, 2007.

[25] Lavender, C., *et al.*, "The Effect Of Laser Shock Peening On The Life And Failure Mode Of A Cold Pilger Die," *Journal Of Materials Processing Technology*, vol. 204, no. 1–3, pp. 486–491, 2008.

[26] Zhang, L., *et al.*, "Effects Of Different Shocked Paths On Fatigue Property Of 7050-T7451 Aluminum Alloy During Two-Sided Laser Shock Processing," *Materials And Design*, vol. 32, no. 2, pp. 480–486, 2011.

[27] Achintha, M., *et al.*, "Fatigue Behaviour Of Geometric Features Subjected To Laser Shock Peening: Experiments And Modelling," *International Journal Of Fatigue*, vol. 62, pp. 171–179, 2014.

[28] Ganesh, P., *et al.*, "Studies On Fatigue Life Enhancement Of Pre-Fatigued Spring Steel Specimens Using Laser Shock Peening," *Materials And Design*, vol. 54, pp. 734–741, 2014.

[29] Wang, J., *et al.*, "Effects Of Laser Shock Peening On Stress Corrosion Behavior Of 7075 Aluminum Alloy Laser Welded Joints," *Materials Science And Engineering A*, vol. 647, pp. 7–14, 2015.

[30] Wang, F., *et al.*, "Laser Shock Processing Of Polycrystalline Alumina Ceramics," *Journal Of The American Ceramic Society*, vol. 100, no. September 2016, pp. 911–919, 2016.

[31] Petronic, S., *et al.*, "Picosecond Laser Shock Peening Of Nimonic 263 At 1064 Nm And 532 Nm Wavelength," *Metals*, vol. 6, no. 3, p. 41, 2016.

[32] Salimianrizi, A., *et al.*, "Effect Of Laser Shock Peening On Surface Properties And Residual Stress Of Al6061-T6," *Optics And Lasers In Engineering*, vol. 77, pp. 112–117, 2016.

[33] Granados-Alejo, V., *et al.*, "Influence Of Specimen Thickness On The Fatigue Behavior Of Notched Steel Plates Subjected To Laser Shock Peening," *Optics And Laser Technology*, vol. 101, pp. 531–544, 2017.

[34] Eisensmith, D., "Fatigue Effects Of Laser Shock Peening Minimally Detectable Partial Through Thickness Surface Cracks," MS Thesis, AFIT-GA-ENY-MS-17M, School of Engineering and Management, Air Force Institute of Technology (AU), Wright-Patterson AFB, OH, March, 2017.

[35] Eisensmith, D., *et al.*, "Re[1] Eisensmith, Et Al., 'Residual Stress Evaluation Of Laser Shock

Peening Over A Partial Through The Thickness Crack,' Vol. 5, No. 11, P. 2016, 2016.Sidual Stress Evaluation Of Laser Shock Peening Over A Partial Through The Thickness Crack," vol. 5, no. 11, p. 2016, 2016.

[36] Lainé, S., *et al.*, "Microstructural Characterisation Of Metallic Shot Peened And Laser Shock Peened Ti–6Al–4V," *Acta Materialia*, vol. 123, pp. 350–361, 2017.

[37] Sun, R., *et al.*, "Microstructure, Residual Stress And Tensile Properties Control Of Wire-Arc Additive Manufactured 2319 Aluminum Alloy With Laser Shock Peening," *Journal Of Alloys And Compounds*, vol. 747, pp. 255–265, 2018.

[38] Berthe, L., *et al.*, "Shock Waves From A Water-Confined Laser-Generated Plasma," *Journal Of Applied Physics*, vol. 82, no. 1997, pp. 2826–2832, 1997.

[39] Braisted, W. and Brockman, R., "Finite Element Simulation Of Laser Shock Peening," *International Journal Of Fatigue*, vol. 21, no. 7, pp. 719–724, 1999.

[40] Meyers, M., *Dynamic Behavior Of Materials*. New York City: Wiley, 1994.

[41] Ding, K. and Ye, L., "Three-Dimensional Dynamic Finite Element Analysis Of Multiple Laser Shock Peening Processes," *Surface Engineering*, vol. 19, no. 5, pp. 351–358, 2003.

[42] Warren, A., *et al.*, "Massive Parallel Laser Shock Peening: Simulation, Analysis, And Validation," *International Journal Of Fatigue*, vol. 30, no. 1, pp. 188–197, 2008.

[43] Engebretsen, C., *et al.*, "Integrated Finite Element & Optimization Model For Laser Shock Pressure Impulse Shape Determination," *Engineering Research Express*, vol. 1, no. 1, 2019.

[44] Dewald, A. and Hill, M., "Eigenstrain-Based Model For Prediction Of Laser Peening Residual Stresses In Arbitrary Three-Dimensional Bodies. Part 1: Model Description," *Journal Of Strain Analysis For Engineering Design*, vol. 44, no. 1, pp. 1–11, 2009.

[45] Dewald, A. and Hill, M., "Eigenstrain-Based Model For Prediction Of Laser Peening Residual Stresses In Arbitrary Three-Dimensional Bodies. Part 2: Model Verification," *Journal Of Strain Analysis For Engineering Design*, vol. 44, no. 1, pp. 13–27, 2009.

[46] Singh, G. and Grandhi, R., "Fatigue Life Optimization Using A Laser Peening Process," *50th AIAA/ASME/ASCE/AHS/ASC Structures, Structural Dynamics, And Materials Conference*, no.

May, 2009.

[47] Singh, G., “Effective Simulation And Optimization Of A Laser Peening Process,” PhD Dissertation, Wright State University, Fairborn, OH, 2009.

[48] Nam, T., “Finite Element Analysis Of Residueal Stress Field Induced By Laser Shock Peening,” PhD Dissertation, The Ohio State University, Columbus, OH, 2002.

[49] Ivetic, G., “Three-Dimensional FEM Analysis Of Laser Shock Peening Of Aluminium Alloy 2024-T351 Thin Sheets,” *Surface Engineering*, vol. 27, no. 6, pp. 445–453, 2011.

[50] Brockman, R., *et al.*, “Prediction And Characterization Of Residual Stresses From Laser Shock Peening,” *International Journal Of Fatigue*, vol. 36, no. 1, pp. 96–108, 2012.

[51] Hfaiedh, N., *et al.*, “Finite Element Analysis Of Laser Shock Peening Of 2050-T8 Aluminum Alloy,” *International Journal Of Fatigue*, vol. 70, pp. 480–489, 2015.

[52] Li, P., *et al.*, “Numerical Simulation And Experiments Of Titanium Alloy Engine Blades Based On Laser Shock Processing,” *Aerospace Science And Technology*, vol. 40, pp. 164–170, 2015.

[53] Langer, K., *et al.*, “High Strain-Rate Material Model Validation For Laser Peening Simulation,” *The Journal Of Engineering*, no. September, 2015.

[54] Halilovič, M., *et al.*, “Prediction Of The Residual State In 304 Austenitic Steel After Laser Shock Peening - Effects Of Plastic Deformation And Martensitic Phase Transformation,” *International Journal Of Mechanical Sciences*, vol. 111–112, pp. 24–34, 2016.

[55] Sealy, M., *et al.*, “Finite Element Modeling Of Hybrid Additive Manufacturing By Laser Shock Peening,” in *Proceedings of the 27th Annual International Solid Freeform Fabrication Symposium*, 2016, no. September, pp. 306–316.

[56] Kamkarrad, H. and Narayanswamy, S., “FEM Of Residual Stress And Surface Displacement Of A Single Shot In High Repetition Laser Shock Peening On Biodegradable Magnesium Implant,” *Journal Of Mechanical Science And Technology*, vol. 30, no. 7, pp. 3265–3273, 2016.

[57] Hasser, P., *et al.*, “An Efficient Reliability-Based Simulation Method For Optimum Laser Peening Treatment,” *Journal Of Manufacturing Science And Engineering*, vol. 138, no. 11, p. 111001, 2016.

[58] Cao, Y., *et al.*, "Parametric Study On Single Shot And Overlapping Laser Shock Peening On Various Metals Via Modeling And Experiments," *Journal Of Manufacturing Science And Engineering*, vol. 132, no. 6, p. 061010, 2010.

[59] Wang, C., *et al.*, "Numerical Modeling Of The Confined Laser Shock Peening Of The OFHC Copper," *International Journal Of Mechanical Sciences*, vol. 108–109, pp. 104–114, 2016.

[60] Je, G., *et al.*, "A Study On Micro Hydroforming Using Shock Wave Of 355 Nm UV-Pulsed Laser," *Applied Surface Science*, vol. 417, pp. 244–249, 2017.

[61] Luo, K., *et al.*, "Massive Laser Shock Peening Of An Aluminium Alloy And The Effects Of Overlapping Rate On Residual Stress Relaxation When Under Cyclic Loading," *Lasers In Engineering*, vol. 38, no. 3–6, pp. 353–368, 2017.

[62] Frija, M., *et al.*, "Optimization Of Peened-Surface Laser Shock Conditions By Method Of Finite Element And Technique Of Design Of Experiments," *International Journal Of Advanced Manufacturing Technology*, 2018.

[63] Banas, G., "An Application Of PVDF Gauges For Pressure Measurements During Laser Shock Processing," *Transactions On Engineering Sciences*, vol. 8, pp. 239–346, 1995.

[64] Nguyen, T., *et al.*, "Effects Of An Absorptive Coating On The Dynamics Of Underwater Laser-Induced Shock Process," *Applied Physics A: Materials Science And Processing*, vol. 116, no. 3, pp. 1109–1117, 2014.

[65] Glaser, D. and Polese, C., "Cavitation Bubble Oscillation Period As A Process Diagnostic During The Laser Shock Peening Process," *Applied Physics A: Materials Science And Processing*, vol. 123, no. 9, pp. 1–10, 2017.

[66] Guo, Y. and Caslaru, R., "Fabrication And Characterization Of Micro Dent Arrays Produced By Laser Shock Peening On Titanium Ti-6Al-4V Surfaces," *Journal Of Materials Processing Technology*, vol. 211, no. 4, pp. 729–736, 2011.

[67] Montross, C., *et al.*, "Laser Shock Processing And Its Effects On Microstructure And Properties Of Metal Alloys: A Review," *International Journal Of Fatigue*, vol. 24, no. 10, pp. 1021–1036, 2002.

[68] Li, K., *et al.*, "Experimental Study Of Micro Dimple Fabrication Based On Laser Shock

Processing," *Optics And Laser Technology*, vol. 48, pp. 216–225, 2013.

[69] Karthik, D. and Swaroop, S., "Laser Peening Without Coating Induced Phase Transformation And Thermal Relaxation Of Residual Stresses In AISI 321 Steel," *Surface And Coatings Technology*, vol. 291, pp. 161–171, 2016.

[70] Gujba, A. and Medraj, M., *Laser Peening Process And Its Impact On Materials Properties In Comparison With Shot Peening And Ultrasonic Impact Peening*, vol. 7, no. 12. 2014.

[71] Nalla, R., *et al.*, "On The Influence Of Mechanical Surface Treatments-Deep Rolling And Laser Shock Peening-On The Fatigue Behavior Of Ti-6Al-4V At Ambient And Elevated Temperatures," *Materials Science And Engineering A*, vol. 355, no. 1–2, pp. 216–230, 2003.

[72] Kalainathan, S. and Prabhakaran, S., "Recent Development And Future Perspectives Of Low Energy Laser Shock Peening," *Optics And Laser Technology*, vol. 81, pp. 137–144, 2016.

[73] Caslaru, R., *et al.*, "Fabrication And Characterization Of Micro Dent Array Produced By Laser Shock Peening On Aluminum Surfaces," *Transactions Of NAMRI/SME*, vol. 37, pp. 159–166, 2009.

[74] Mordyuk, B., *et al.*, "Characterization Of Ultrasonically Peened And Laser-Shock Peened Surface Layers Of AISI 321 Stainless Steel," *Surface And Coatings Technology*, vol. 202, no. 19, pp. 4875–4883, 2008.

[75] George, T., *et al.*, "Goodman Diagram Via Vibration-Based Fatigue Testing," *Journal Of Engineering Materials And Technology, Transactions Of The ASME*, vol. 127, no. 1, pp. 58–64, 2005.

[76] Li, J. and Wang, S., "Distortion Caused By Residual Stresses In Machining Aeronautical Aluminum Alloy Parts: Recent Advances," *International Journal Of Advanced Manufacturing Technology*, vol. 89, no. 1–4, pp. 997–1012, 2017.

[77] Litteken, C., *et al.*, "Residual Stress Effects On Plastic Deformation And Interfacial Fracture In Thin-Film Structures," *Acta Materialia*, vol. 53, no. 7, pp. 1955–1961, 2005.

[78] Ballard, P., *et al.*, "Residual Stresses Induced By Laser-Shocks," *Journal De Physique IV Colloque*, vol. 01, no. C3, pp. 487–494, 1991.

[79] Schajer, G., *Stress Measurement Methods Practical Residual Stress Measurement*. West Sussex: John Wiley & Sons, 2013.

[80] Ramadhan, R., *et al.*, "Mapping Residual Strain Induced By Cold Working And By Laser Shock Peening Using Neutron Transmission Spectroscopy," *Materials And Design*, vol. 143, pp. 56–64, 2018.

[81] Chen, H., *et al.*, "Fourier Analysis Of X-Ray Micro-Diffraction Profiles To Characterize Laser Shock Peened Metals," *International Journal Of Solids And Structures*, vol. 42, no. 11–12, pp. 3471–3485, 2005.

[82] Chen, H., *et al.*, "Characterization Of Plastic Deformation Induced By Microscale Laser Shock Peening," *Journal Of Applied Mechanics*, vol. 71, no. 5, p. 713, 2004.

[83] Benedetti, M., *et al.*, "Residual Stresses Reconstruction In Shot Peened Specimens Containing Sharp And Blunt Notches By Experimental Measurements And Finite Element Analysis," *International Journal Of Fatigue*, vol. 87, pp. 102–111, 2016.

[84] Pei, Y. and Duan, C., "Study On Stress-Wave Propagation And Residual Stress Distribution Of Ti-17 Titanium Alloy By Laser Shock Peening," *Journal Of Applied Physics*, vol. 122, no. 19, 2017.

[85] King, A., *et al.*, "Effects Of Fatigue And Fretting On Residual Stresses Introduced By Laser Shock Peening," *Materials Science And Engineering A*, vol. 435–436, pp. 12–18, 2006.

[86] Pagliaro, P., *et al.*, "Measuring Inaccessible Residual Stresses Using Multiple Methods And Superposition," *Experimental Mechanics*, vol. 51, no. 7, pp. 1123–1134, 2011.

[87] Winiarski, B., *et al.*, "High Spatial Resolution Evaluation Of Residual Stresses In Shot Peened Specimens Containing Sharp And Blunt Notches By Micro-Hole Drilling, Micro-Slot Cutting And Micro-X-Ray Diffraction Methods," *Experimental Mechanics*, vol. 56, no. 8, pp. 1449–1463, 2016.

[88] Dassault-Systemes, *Abaqus 6.14 Documentation*. Providence, Rhode Island: Dassault Systemes, 2014.

[89] Buentello Hernandez, R., "3D Finite Element Modeling Of Sliding Wear," PhD Dissertation, AFIT-ENY-DS-13S, School of Engineering and Management, Air Force Institute of Technology (AU), Wright-Patterson AFB, OH, March, 2013.

[90] Dunne, F. and Petrinic, N., *Introduction To Computational Plasticity*. Oxford University, UK: Oxford University Press, 2006.

[91] Grązka, M. and Janiszewski, J., "Identification Of Johnson-Cook Equation Constants Using Finite Element Method," *Engineering Transactions*, vol. 60, no. 3, pp. 215–223, 2012.

[92] Fabbro, R., *et al.*, "Physical Study Of Laser-produced Plasma In Confined Geometry," *Journal Of Applied Physics*, vol. 68, no. 40, pp. 775–808, 1990.

[93] Hooke, R. and Jeeves, T., "'Direct Search''' Solution Of Numerical And Statistical Problems,'" *Journal Of The ACM*, vol. 8, no. 2, pp. 212–229, 1961.

[94] Dassault-Systemes, *Isight Documentation & User's Manual*. Providence, Rhode Island: Dassault Systemes, 2010.

[95] Prime, M. and Hill, M., "Uncertainty , Model Error , And Order Selection For Series-," vol. 128, no. April, 2006.

[96] Nanovea, "Profilometer Brochure," 2016. [Online]. Available: https://nanovea.com/brochure/.

[97] Lesuer, D., "Experimental Investigations Of Material Models For Ti-6Al-4V Titanium And 2024-T4 Aluminum," Washington DC, 2000.

[98] Engebretsen, C., *et al.*, "Finite Element Model Correlation Of Laser Shock Peening," in *2018 AIAA/ASCE/AHS/ASC Structures, Structural Dynamics, and Materials Conference*, 2018.

[99] Engebretsen, C., *et al.*, "Strain Rate Dependent FEM Of Laser Shock Induced Residual Stress," *Challenges In Mechanics Of Time-Dependent Materials*, vol. 2, pp. 109–114, 2019.

[100] Kanel, G., "Unusual Behaviour Of Usual Materials In Shock Waves," *Journal Of Physics: Conference Series*, vol. 500, no. PART 1, 2014.

[101] Sun, R., *et al.*, "Dynamic Response And Residual Stress Fields Of Ti6Al4V Alloy Under Shock Wave Induced By Laser Shock Peening," *Modelling And Simulation In Materials Science And Engineering*, vol. 25, no. 6, 2017.

[102] Engebretsen, C., *et al.*, "Laser Shock Impulse Modelling Via Data Matching," in *2019 AIAA/ASCE/AHS/ASC Structures, Structural Dynamics, and Materials Conference*, 2019.

[103] Devore, J. and Peck, R., *Statistics, The Exploration And Analysis Of Data*, 4th ed. Duxbury,

Thomson Learning, 2001.

[104] Turnbull, A. and De Los Rios, E., "The Effect Of Grain Size On Fatigue Crack Growth In An Aluminium Magnesium Alloy," *Fatigue & Fracture Of Engineering Materials And Structures*, vol. 18, no. 11, pp. 1355–1366, 1995.

[105] Hill-Engineering, "Hole-Drilling Measurement Report," Rancho Cordova, CA, 2019.